ABSTRACT

Title of dissertation: EXPLOITING COLLECTIVE EFFECTS TO DIRECT LIGHT ABSORPTION IN NATURAL AND ARTIFICIAL LIGHT-HARVESTERS

Chris Schroeder,
Doctor of Philosophy, 2016

Dissertation directed by: Professor Luis A. Orozco
Joint Quantum Institute,
University of Maryland Department of Physics
and
National Institute of Standards and Technology

Photosynthesis – the conversion of sunlight to chemical energy – is fundamental for supporting life on our planet. Despite its importance, the physical principles that underpin the primary steps of photosynthesis, from photon absorption to electronic charge separation, remain to be understood in full. Electronic coherence within tightly-packed light-harvesting (LH) units or within individual reaction centers (RCs) has been recognized as an important ingredient for a complete understanding of the excitation energy transfer (EET) dynamics. However, the electronic coherence across units – RC *and* LH or LH *and* LH – has been consistently neglected as it does not play a significant role during these relatively slow transfer processes. Here, we turn our attention to the absorption process, which, as we will show, has a much shorter built-in timescale. We demonstrate that the – often overlooked – spatially extended but short-lived excitonic delocalization plays a relevant role in

general photosynthetic systems. Most strikingly, we find that absorption intensity is, quite generally, redistributed from LH units to the RC, increasing the number of excitations which can effect charge separation without further transfer steps. A biomemetic nano-system is proposed which is predicted to funnel excitation to the RC-analogue, and hence is the first step towards exploiting these new design principles for efficient artificial light-harvesting.

Exploiting Collective Effects to Direct Light Absorption in Natural and Artificial Light-Harvesters

by

Christopher Schroeder

Dissertation submitted to the Faculty of the Graduate School of the
University of Maryland, College Park in partial fulfillment
of the requirements for the degree of
Doctor of Philosophy
2016

Advisory Committee:
Professor Luis A. Orozco, Chair/Advisor
Professor Martin B. Plenio
Professor Arpita Upadhyaya
Professor Christpher Jarzynski
Professor Peter S. Shawhan

Acknowledgments

Professor Luis Orozco has been an outstanding advisor. I am deeply grateful for his cheerful and unflagging support, without which this research would have never been possible.

Professor Martin Plenio, through his open curiosity and remarkable insight, has been a model physicist. I am deeply grateful for the opportunity to study at his stimulating and egalitarian Institute of Theoretical Physics.

Dr. Felipe Caycedo sat across from me for the duration of our research, and it is only through his optimistic and humble example that I leave better than I arrived.

I also thank the National Science Foundation for support through a Graduate Research Fellowship and the PFC@JQI.

Table of Contents

Chapter 1: Introduction

1.1 Absorption in Light-Harvesting Complexes

The main task of this thesis will be to describe changes in absorption, and the subsequent transfer events, upon coupling between light-harvesting units, as summarized in Figure 1.1. The natural and artificial light-harvesting complexes we will consider are composed of light-absorbing pigments which interact to collectively facilitate absorption and transfer of excitation. Light-harvesting (LH) complexes are most often organized hierarchically into (1) a large antenna structure, the main purpose of which is to harvest light, and (2) a smaller reaction center (RC), where chemical reactions take place that turn excitation energy into usable chemical energy. The combined system funnels excitation into the RC, either through transfer events or through direct absorption of the RC pigments. We will show that collective effects in the combined system are constructed in such a way that the direct absorption of the RC pigments in the combined system is greater than in the isolated RC. The coherent effects arising from the weak coupling between light-harvesting units at short times are destroyed by interactions with their warm, wet environment, leading to incoherent (classical) transfer at later times. However, these short-lived coherent signatures are witnessed by the absorption spectrum, which has a faster

built-in timescale than both decoherence and transfer.

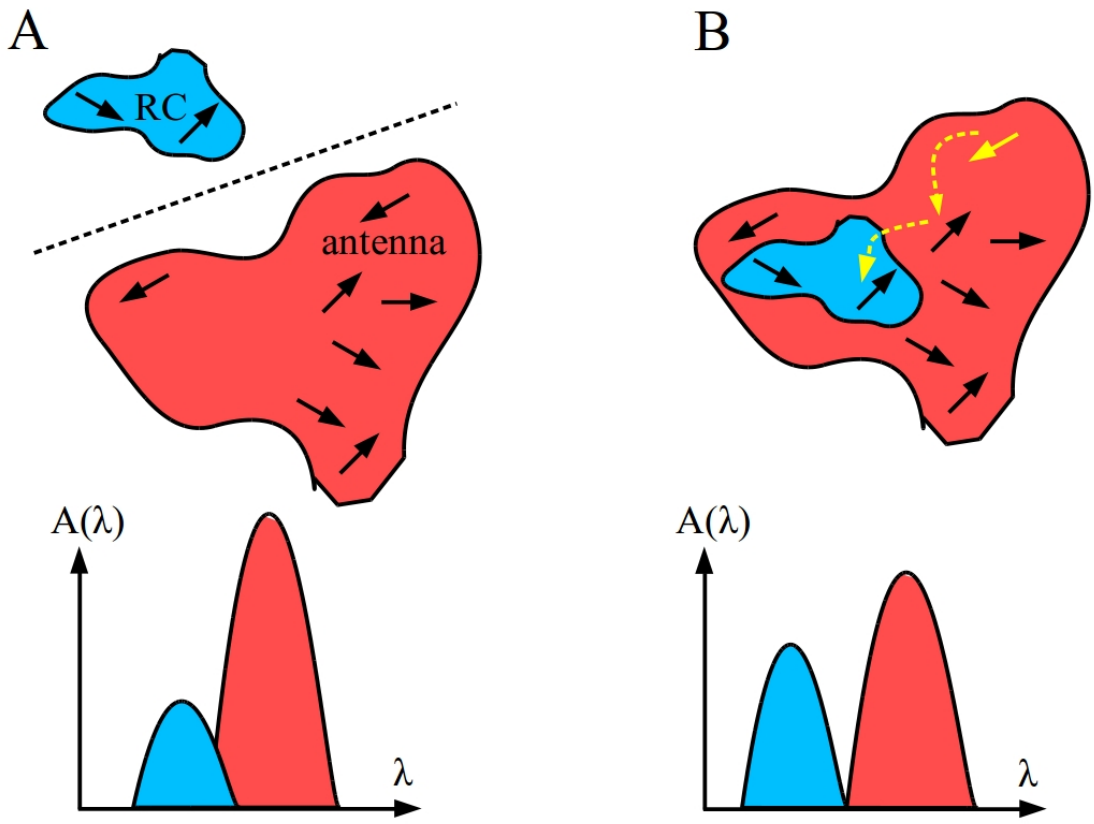

Figure 1.1: (A) Light-harvesting pigments are organized in a large antenna structure, the main purpose of which is to harvest light, and a smaller reaction center (RC), where chemical reactions take place that turn excitation energy into usable chemical energy. The function of the combined system (B) is to funnel excitation into the RC, either through transfer events or through direct absorption of the RC pigments. We will show that collective effects in the combined system are constructed in such a way that the direct absorption of the RC pigments in the combined system (B) is greater.

Our work occurs within the context of a wide-spread re-consideration of biological processes within the formalism of quantum mechanics, so-called quantum biology [1, 2]. In the next section we argue why such a consideration is useful, or perhaps even necessary, and illustrate some biological phenomena which are thought to exhibit quantum signatures. Within quantum biology, quantum mechanics has

found its best application in a description of the primary processes of photosynthesis, the biochemistry of which is summarized in Chapter 2. The requisite quantum mechanical formalism is introduced in Chapter 3. In Chapter 4 we demonstrate theoretically that the excitonic delocalization across several LH units leads to unambiguous signatures in the optical response, specifically, linear absorption spectra. We demonstrate that this optical response could be used as a diagnostic tool to determine the coherent coupling between iso-energetic light-harvesting structures. The knowledge of these couplings would then provide further insight into the dynamical properties of transfer, such as facilitating the accurate determination of Förster rates. We also demonstrate, in Chapter 5, that delocalization across the RC and its LH complex redistributes direct absorption towards the charge separation unit, thereby increasing the photosynthetic efficiency. Using the complete core complex of *Rhodospirillum rubrum*, we verify experimentally a 90 % increase in the direct optical absorption of the RC *in situ* as compared to isolated RCs. Calculations reveal that similar enhancements can be expected for a wide variety of photosynthetic units in both plant and bacterial systems, suggesting that this mechanism is conserved across species. Our studies illuminate clear new design principles for light-harvesting nanostructures, which we explore theoretically in Chapter 6 through a proposed biomemetic light-harvester– specifically, a 2-dimensional array of metal nanoparticles anchored to a DNA-origami scaffold– which is predicted to exhibit a 60 % enhancement of the direct absorption of the spectrally-distinct resonance of the RC-analogue.

1.2 Quantum Biology

The current interest in quantum effects in biology was precipitated by recent experiments which observed long-lasting oscillations in time-resolved spectroscopy of photosynthetic light-harvesting complexes [3–8]. These experiments have driven a wave of theoretical work which explains experiments [9–12] and broadens our understanding of the effects of the vibrational environment [2, 13–20]. These long-lasting oscillations have been attributed to quantum coherences, although their nature– electronic, vibrational or vibronic (a mixture of electronic and vibrational)– is still disputed. Such wave-like behavior is often attributed to, and is here well-described by, quantum theory, and the interest of the community has been piqued by the possibility that nature exploits quantum mechanics to effect efficient exciton transport. In general, two questions motivate research in this field: are biological processes sensitive to quantum effects? If so, when does nature exploit quantum effects, and when does nature suppress them?

Two perhaps better-posed, if less consequential, questions that will motivate this thesis are: when must a biological phenomenon be described by a quantum theory? If it must be described by a quantum theory, does that mean that the phenomenology is strictly quantum? Although many– indeed, in principle, all– phenomena can be described by quantum theory, very often a classical theory is sufficient, and such a theory is often simpler, as well. The conclusion of this thesis will be that, just because a phenomenon requires a quantum theory does not mean that there is no classical analogue, or a classical system which exhibits the same

principles. Explicitly, we will find that a good description of absorption in the RC-LH1 core complex of purple bacteria– which must be described by a quantum theory because its fundamental unit, the bacteriochlorophyll, is "small enough" to exhibit quantum properties– requires (extended) excitonic delocalization, or quantum superposition states. However, we will also find that the phenomenology– and the design principle for efficient light-harvesting– has a direct classical analogue in the collective resonances of metal-nanoparticle arrays. Metal nanoparticles can be described by a simple classical theory because they are mesoscopic objects containing many particles, and, although *quantum* coherence between electrons is extremely short-lived, their collective properties rely on *classically* coherent electron oscillations. Hence, it is perhaps more accurate to say that this thesis is concerned with exploiting collective and coherent effects, regardless of their description, for efficient light-harvesting.

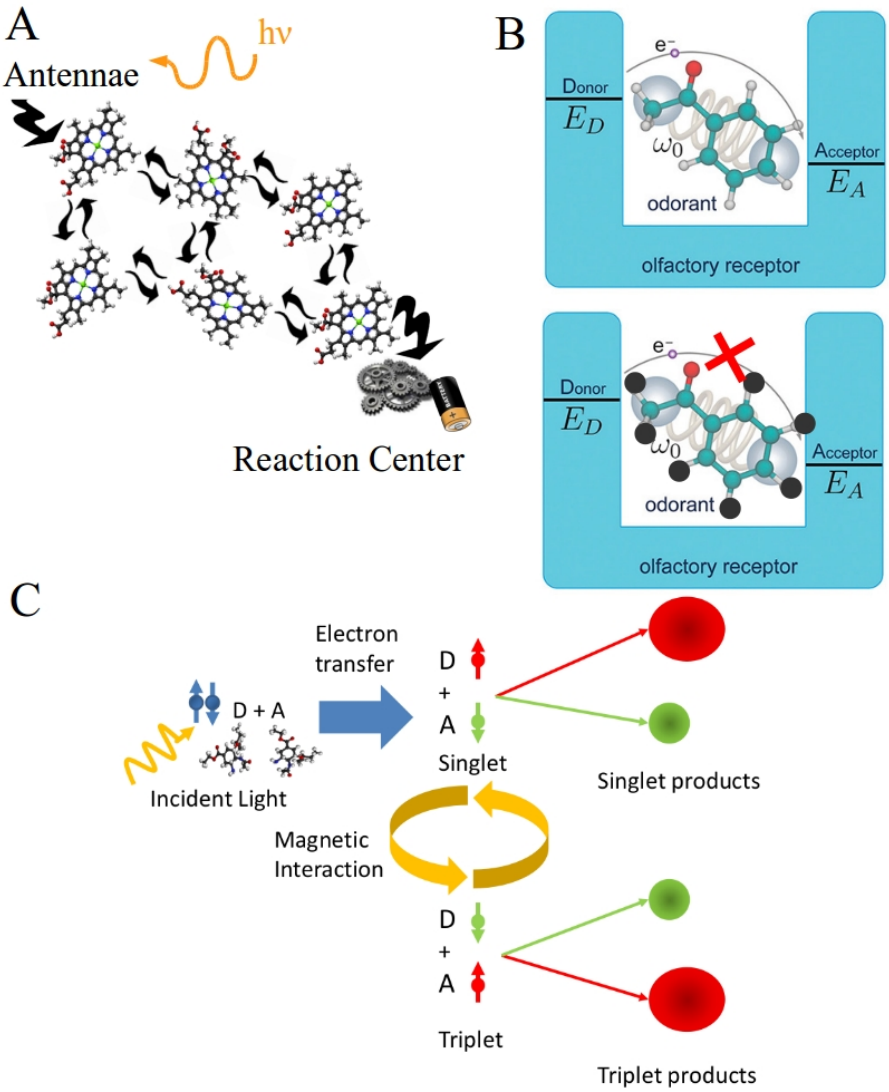

Figure 1.2: (A) *[reproduced and adapted from Ref. [2]]* Light-harvesting antennae capture light and transfer excitation to a reaction center, where charge separation takes place. Long-lasting oscillations in time-resolved spectroscopy of LH complexes have been explained by quantum theories which attribute these oscillations to quantum coherences. (B) *[reproduced and adapted from Ref. [21]]* A quantum theory of olfaction posits that olfactory receptors exploit incoherent electron tunnelling to sense the vibrational modes of odorants, and thereby discriminate between them. (C) *[reproduced from Ref. [2]]* Avian magnetoreception has been proposed to operate by a chemical compass that exploits spin chemistry. A radical pair in the singlet state is photoexcited, and magnetic interactions mix singlet and triplet states, which lead to differentiable products.

Excitonic effects in photosynthetic light-harvesting complexes comprise one

facet of quantum biology. The distinctly quantum feature of that theory is the wave-like nature of transport, which is described classically by incoherent (thermal) hopping. Other applications of quantum theory to biological phenomena are illustrated in Fig. 1.2. A quantum theory of olfaction postulates that the well-accepted "shape theory" of olfaction, in which odorants are recognized strictly by their structure, is insufficient [21]. Inelastic electron tunnelling could allow an olfactory receptor to discriminate odorants by their vibrational structure. As pictured schematically in Fig. 1.2 (A), inelastic electron tunnelling across a gapped receptor is enhanced if the gap matches that between discrete vibrational energy levels of the odorant. The most straightforward test of this theory measures if an organism can discriminate between an odorant and its deuterated form, as illustrated schematically in Fig. 1.2 (B). Deuteration changes the mode energy structure with respect to the receptor gap, and thereby changes electron transport properties. In this way, an organism could discriminate between an odorant and its deuterated form, a prediction which has been verified experimentally [22]. The distinctly quantum feature of this theory is the discretization of energy levels. It has also been proposed that birds orient in the earth's magnetic field by exploiting spin chemistry [23–25]. Photoexcitation of and electron transfer within a particular molecule– cytochrome has been proposed– in the bird's eye creates a radical pair– two molecules with non-zero spin– in the singlet state. Interaction with the earth's magnetic field and, crucially, nuclear spins mixes singlet and triplet states, which each lead to chemically-differentiable products, as depicted schematically in Fig. 1.2 (C). The relative singlet-to-triplet product after photoexcitation depends on the strength of the field, and is therefore

a sensing mechanism. The distinctly quantum feature of this theory is spin.

1.3 Publications and Authorship

This thesis is partly based on, or reproduced from, material that has been published elsewhere. This relates, in particular, to Chapters 4 and 5, which are largely identical to Ref. [26] and Ref. [27]. However, 5 contains new, more rigorous calculations which will be included in the new version of Ref. [27] that is in preparation. Results which are discussed but not obtained by the author will be made clear in the text. In particular, full numerical simulations of *R. sphaeroides* and *Rsp. palustris* were performed by Dr. Felipe Caycedo-Soler (University of Ulm), and the experiments on *R. rubrum* were performed by Dr. Carline Autenrieth and Prof. Dr. Robin Ghosh (University of Stuttgart), and are discussed in detail in Appendix 8.

Chapter 2: Biochemistry of Purple Bacteria

This chapter reviews the biochemistry of photosynthesis and the structural details of photosynthetic complexes with a focus on the purple bacteria species *Rhodospirillum rubrum*, which will be our model organism in later chapters for probing quantum effects in absorption, theoretically and experimentally.

2.1 Photosynthesis in Purple Bacteria

Although the chemical and structural details of photosynthesis exhibit great diversity, the basic mechanism, pictured in Fig. 2.1 (A), is conserved. The primary processes of photosynthesis use light energy to power charge separation in the photosynthetic complex to create an electron gradient across a membrane. Photosynthetic complexes consist of strongly coupled light-harvesting (LH) units where the coupling between LH units is relatively weak. An electrochemical gradient is used to create ATP, the biological currency of energy. Figure 2.1 (B) details the photosynthetic cycle in many purple bacteria. Light is captured by light-harvesting complexes 1 and 2 (LH1 and LH2), and shuttled to the reaction center (RC), where charge separation takes place. Cytochrome shuttles electrons back from the bc_1 com-

plex, where the electron gradient is used to create a proton gradient. The ATPase synthesizes ATP from ADP using this proton gradient. We will use the anoxygenic photosynthetic purple bacteria *R. rubrum* to exhibit and explore quantum effects in the primary processes of photosynthesis – from photon absorption to charge separation [28]. *R. rubrum* is a highly-adaptable organism, allowing it to thrive in many different aquatic environments, including lakes, ponds, streams and standing water. It contains only LH1 complexes and RCs, while many purple bacteria additionally contain LH2.

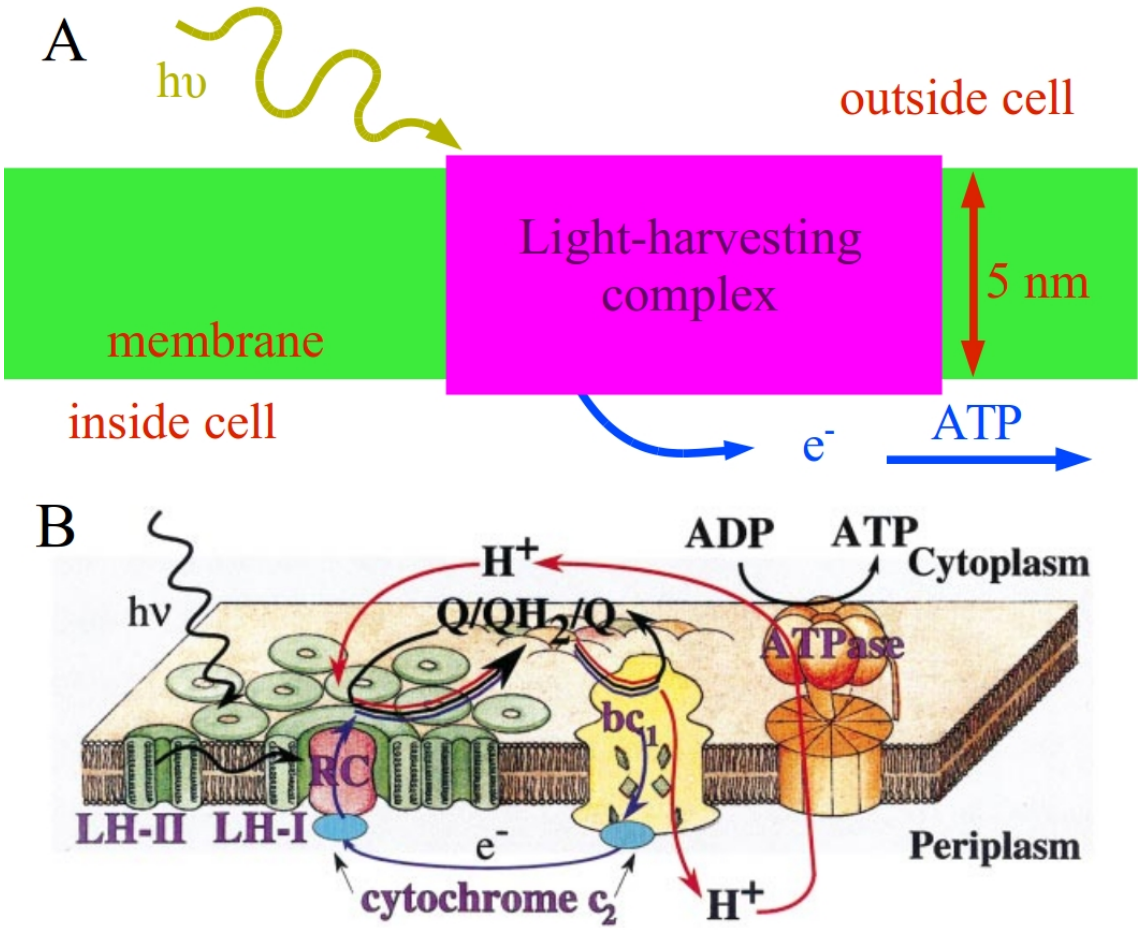

Figure 2.1: (A) The primary processes of photosynthesis convert light energy into an electron gradient across a membrane by a light-harvesting complex. An electrochemical gradient is used to create ATP, the biological currency of energy. (B) *[reproduced from Ref. [28]]* The photosynthetic apparatus in purple bacteria. Light is captured by light-harvesting complexes 1 and 2 (LH1 and LH2), and shuttled to the reaction center (RC), where charge separation takes place. Cytochrome shuttles electrons back from the bc_1 complex, where the electron gradient is used to create a proton gradient. The ATPase synthesizes ATP from ADP using this proton gradient.

2.2 Bacteriochlorophyll

The fundamental unit in purple bacteria which facilitates both light absorption and charge separation is bacteriochlorophyll (BChl). The species and geometry

of BChls determine an LH unit, such as LH1, LH2 or RC in purple bacteria. For example, an LH1 complex contains 32 BChl a molecules arranged in a ring-like geometry. The absorption properties of BChl can be understood by first examining its simplest constituent structure, porphyrin [29]. As pictured in Fig. 2.2 (A), porphyrin is composed of four pyrrole rings which form a conjugated electron system due to the overlap of parallel π orbitals. The absorption spectrum of porphrin, see Fig. 2.2 (C), shows a single strong band in the near-ultraviolet and four weak bands in the visible and near-infrared, and can be understood by a simple free electron model which considers the 18 electrons of the completely conjugated path (see Fig. 2.2 (A)) to be confined to a ring [29–31]. The energies and wavefunctions of this simple model are denoted by an angular quantum number l; explicitly

$$E_l \propto l^2 \tag{2.1}$$

$$|e_l\rangle = \frac{1}{\sqrt{2\pi}} e^{il\phi} \tag{2.2}$$

$$|\Phi_0\rangle = \Pi_{l=-4}^{4} |e_l\rangle \tag{2.3}$$

where the ground state $|\Phi_0\rangle$ is a product of single-electron wavefunctions corresponding to the filling of the energy levels up to $l = \pm 4$, according to Pauli's exclusion principle (see Fig. 2.2 (B)). The transition then occurs from $l = \pm 4$ to $l = \pm 5$ and is

four-fold degenerate, corresponding to changes in angular momentum $\Delta l = \pm 1, \pm 9$.

$$|\Phi_1\rangle = \ldots e^{+4i\phi} e^{+5i\phi} e^{-4i\phi} e^{-4i\phi} \tag{2.4}$$

$$|\Phi_{-1}\rangle = \ldots e^{+4i\phi} e^{+4i\phi} e^{-4i\phi} e^{-5i\phi} \tag{2.5}$$

$$|\Phi_9\rangle = \ldots e^{+4i\phi} e^{+4i\phi} e^{-4i\phi} e^{+5i\phi} \tag{2.6}$$

$$|\Phi_{-9}\rangle = \ldots e^{+4i\phi} e^{-5i\phi} e^{-4i\phi} e^{-4i\phi} \tag{2.7}$$

Only $\Delta l = \pm 1$ transitions are dipole-allowed, and these correspond to the doubly-degenerate, bright Soret band, labelled B in Fig. 2.2 (C). By Hund's rule– which says that for a given multiplicity (degeneracy), the transition with the largest angular momentum has the lowest energy– the $\Delta l = \pm 9$ transitions, corresponding to the Q band, have the lowest energy, consistent with observations. The degeneracy of the bands is broken because the H-H axis, the x-axis in Fig. 2.2 (A), breaks the 90° rotational symmetry. However, only the Q band splits due to the relationship of the wavefunctions to the reduction of the symmetry group from D_{4h} to D_{2h} [32]. The additional peaks in the Q bands correspond to vibrational sidebands. Even from this extremely simplified model, we can see that low-energy spectral features can be characterized by the Q_y optically-induced transition dipole moments.

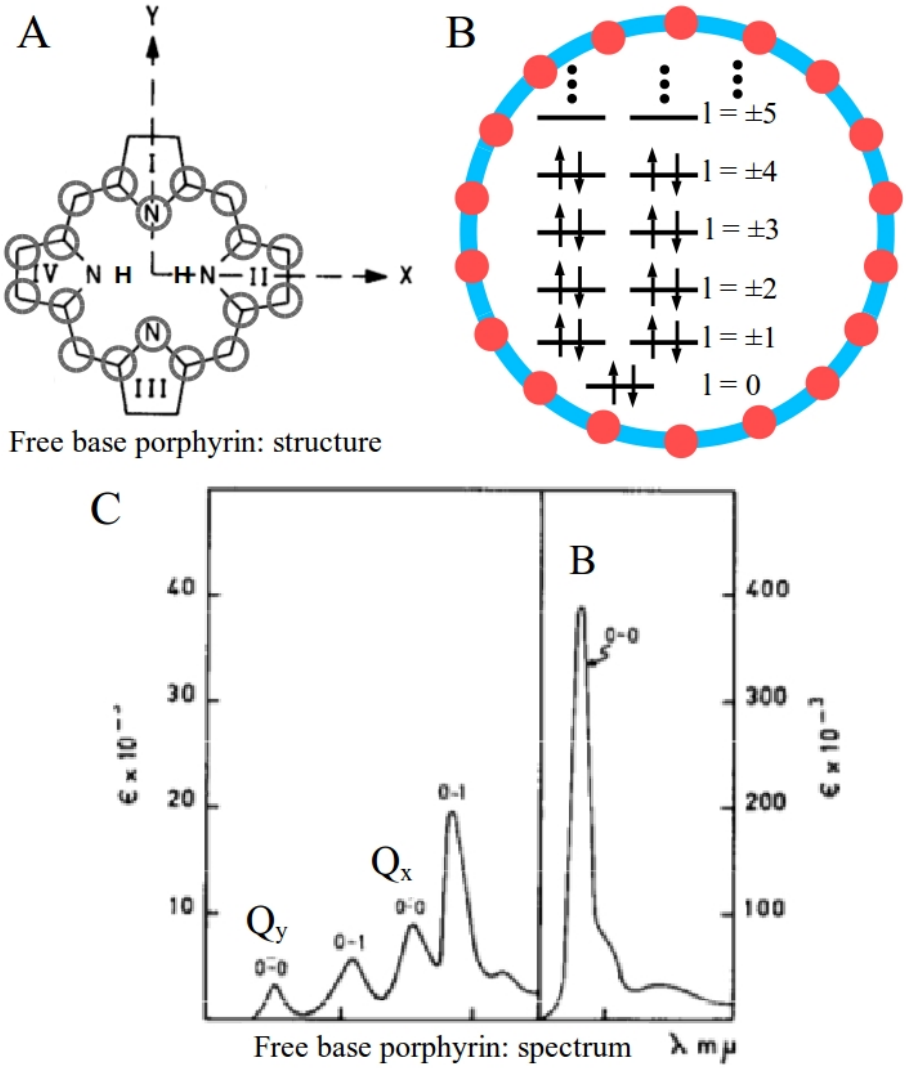

Figure 2.2: (A) *[adapted from Ref. [31]]* Chemical structure of free base porphyrin, the basic chemical unit of bacteriochlorophyll. The labelled x- and y-axes denote the direction of the induced transition dipole moment. The eighteen atoms that form an unbroken conjugated path are circled in grey. (B) A simple model for porphyrin considers 18 free electrons confined to a ring. (C) *[adapted from Ref. [31]]* The absorption spectrum of free-base porphyrin.

In BChl, the porphyrin ring is highly functionalized, as can be seen in Fig. 2.3. These additional functional groups change the conjugation properties, and hence the symmetry of the delocalized electron states, leading to changes in the absorption properties. The biggest change is that the quasi-forbidden Q_y transitions

become highly allowed– that is, pick up considerable dipole strength– due to the extended delocalization along the y-axis. Hence, in what follows, we will describe near-infrared spectral features by considering only the Q_y transitions in BChl, which have an associated induced transition dipole moment along the line joining the nitrogens of unreduced pyrrole rings I and III [33, 34].

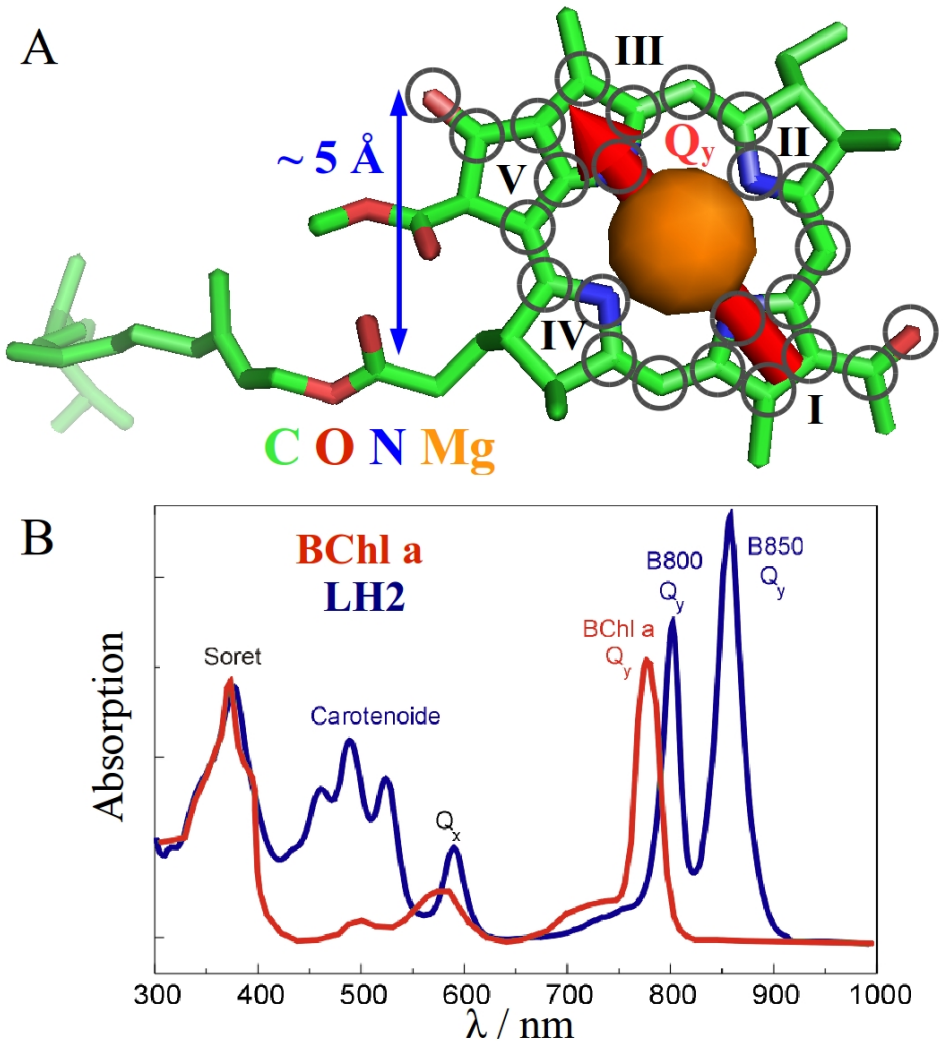

Figure 2.3: (A) Chemical structure of bacteriochlorophyll. The Q_y induced transition-dipole moment, which lies along a line connecting the nitrogen atoms of pyrol rings I and III (atoms NB and ND), is represented by the red arrow. The atoms involved in the π-conjugated electron system are circled in gray. The additional functional groups change the conjugated path from that of the free base porphyrin, leading to greater delocalization along the y-axis and greater dipole strength of the Q_y transition, as can be seen in (B) *[reproduced from Ref. [35]]*, which is quasi-forbidden in the free base porphyrin of Fig. 2.2.

2.3 Structural Model of LH1 and RC

Light-harvesting complexes are a collection of BChl which are held in place by a protein scaffold. In this study we have employed a model of the *R. rubrum* LH1 where 32 BChl molecules, bound to 16 α and β polypeptides as $\alpha\beta(\text{BChl})_2$ subunits, are arranged in a ring-like geometry with C_{16} symmetry, see Fig. 2.4. The Q_y transition dipole moments are tangent to the ring and in the plane. The model was constructed in the group of R. Ghosh [36] in a collaboration with the group of Klaus Schulten (Beckmann Institute, University of Illinois, Urbana-Champaign) in 2002, and was based upon both extensive biochemical and biophysical data, low-resolution projection structures obtained using cryoelectron microscopy (cryoEM) of 2D crystals [37, 38], and homology modelling to the known X-ray structures of the LH2 complexes from *Rhodospirillum molischianum* [39] and *Rhodopseudomomas acidophila* [40] as well as a further homology model of the LH1 structure from *Rhodobacter sphaeroides* [41]. The data from this model, as well as that for the complete *R. rubrum* photosynthetic unit (PSU) (containing the RC) has been used subsequently for biophysical studies of this complex [42–44].

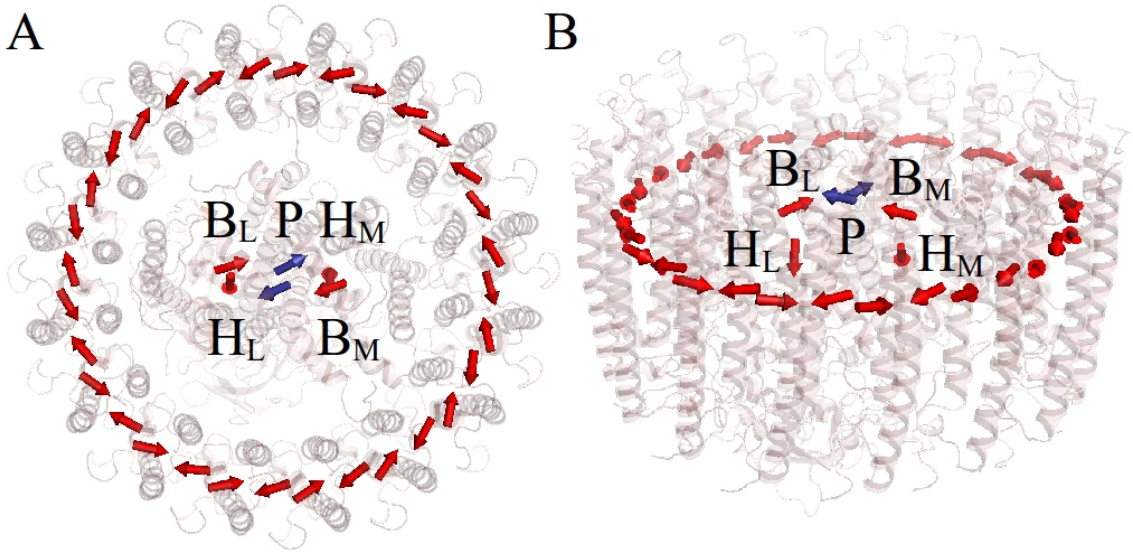

Figure 2.4: (A), (B) The position of the BChl and bacteriopheophytin pigments in the atomic model of the *R. rubrum* LH1-RC complex. The orientations of the Q_y transition moments of the pigments are shown with arrows. The special pair (P), accessory BChls (B_L and B_M) and bacteriopheophytins (H_L and H_M) of the RC are also indicated. The α and β protein subunits are rendered translucent.

The C_{16} symmetry naturally arises from the energy minimization procedure needed to construct the model, and is one of the controversial aspects since it contradicts AFM and cryoEM data obtained for LH1 complexes of other organisms [38,45]. However, fluorescence polarization data obtained from both purified *R. rubrum* LH1 and LH1-RC complexes, respectively, reconstituted and diluted into bilayer membranes [42,43], have yielded results consistent with C_{16} symmetry, so we feel justifed to employ this assumption for the calculations made here. Very recently, the X-ray structure of a thermostable LH1-RC complex from *Thermochromatium tepidum* at near-atomic resolution of 3.0 Å has been published [46]. This LH1-RC complex is also comprised of 16 $\alpha\beta(\text{BChl})_2$ units which form a closed ring, und thus strongly resembles the *R. rubrum* PSU model employed here. However, the *T. tepidum* com-

plex also shows observable ellipticity. Nevertheless, the distances and geometries of the BChl pigments do not differ strongly from our *R. rubrum* model. Furthermore, the crystals were grown in detergent, which may have a destabilizing effect upon the geometry of the LH1-RC complex.

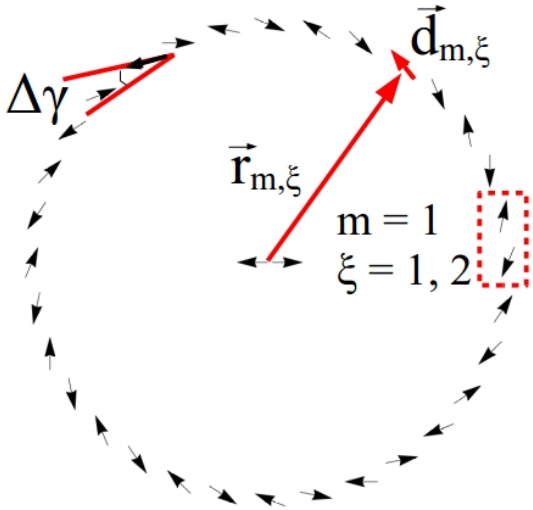

Figure 2.5: Parameterization of RC-LH1 structure according to Eqs. 2.8–2.11.

The LH1 operates as an antenna and probably evolved to increase the absorption cross-section. Charge separation is accomplished by the reaction center (RC), which sits inside the LH1 ring, see Fig. 2.4. A pair of tightly-coupled pigments, called the special pair (P), absorb energy– either by direct absorption or electronic energy transfer from the LH1– and a series of cascading redox reactions transfers electrons to the accessory bacteriochlorophyll (B_M, B_L), then to the bacteriopheophytin (H_M, H_L), and then out of the complex. Note that the Q_y induced transition dipole moments of the P-pigments are nearly anti-parallel and in the plane of the ring.

In this study we have employed a model of the *R. rubrum* LH1 where $M =$

32 BChl molecules, bound to 16 α and β polypeptides as $\alpha\beta(\mathrm{BChl})_2$ subunits, are equidistantly arranged along a ring of radius R = 47 Å. Low energy spectral features can be characterized using the Q_y optically-induced transition dipole moments of the BChl, which lie along a line joining the nitrogens of unreduced pyrrole rings I and III [33]. For simplicity, these dipole moments are taken to be tangential to, and in the plane of, the ring. The LH1 dipoles are taken to be of magnitude $d^{LH1} = \sqrt{2.4}$ $\times$ 6.3 D = 9.8 D to take into account the observed hyperchromism [47]. Explicitly, the positions and dipole moments of the BChl on the LH1 ring are parameterized according to

$$\vec{d}^{LH1}_{m,\zeta} = d^{LH1}(-1)^{\zeta} \begin{pmatrix} \sin(\psi_{m,\zeta}) \\ -\cos(\psi_{m,\zeta}) \end{pmatrix} \tag{2.8}$$

$$\vec{r}^{LH1}_{m,\zeta} = R \begin{pmatrix} \cos(\psi_{m,\zeta}) \\ \sin(\psi_{m,\zeta}) \end{pmatrix} \tag{2.9}$$

$$\psi_{m,\zeta} = \frac{2\pi}{M}\left(\lfloor m/2 \rfloor + \zeta - 1\right) + \Delta\gamma, \tag{2.10}$$

where $\lfloor m/2 \rfloor$ is the largest integer less than or equal to $m/2$. The P-pigments are modelled as two anti-parallel dipoles, of magnitude $d^P = 6.3$ D, at the center of the LH1 ring according to

$$\vec{d}^{P}_{i} = d^{P}(-1)^{i} \begin{pmatrix} 1 \\ 0 \end{pmatrix}, \ \vec{r}^{P}_{i} = \begin{pmatrix} 0 \\ 0 \end{pmatrix} \tag{2.11}$$

This structural parameterization is pictured in Fig. 2.5.

2.4 Absorption Spectra of LH1 and RC

The close proximity of BChl and the geometric and electric fluctuations of the protein change the absorption properties, as can be seen in the LH2 absorption spectrum of Fig. 2.3 and the LH1 absorption spectrum of Fig. 2.6 (A). The description of such changes in the absorption spectrum will be the main task of this thesis. In Chapter 5 we will be concerned with the quantum mechanical coherent coupling between the LH1 and the RC. Figure 2.6 (B) shows the RC spectrum which is composed of three bands: the H band at 760 nm corresponding to the bacteriopheophytin, the B band at 800 nm corresponding to the accessory bacteriochlorophyll and the P band at 870 nm corresponding to the special pair bacteriochlorophyll. In particular, we will be interested in changes to the LH1 880 nm band (B880) and the RC 870 nm band (P870) when the RC is physically inside the LH1, as in the natural configuration, Fig. 2.4. However, the P870 band is buried underneath the much stronger B880 band of the LH1. The experiment will make use of the charge-transfer nature of the P-pigments to isolate the 870 nm peak. After a charge separation event, which removes an electron, the optical properties of the P-pigments change. In particular, they no longer absorb at 870 nm. Cytochrome returns the electron to the special pair after approximately 1 ms, and the P870 peak reappears.

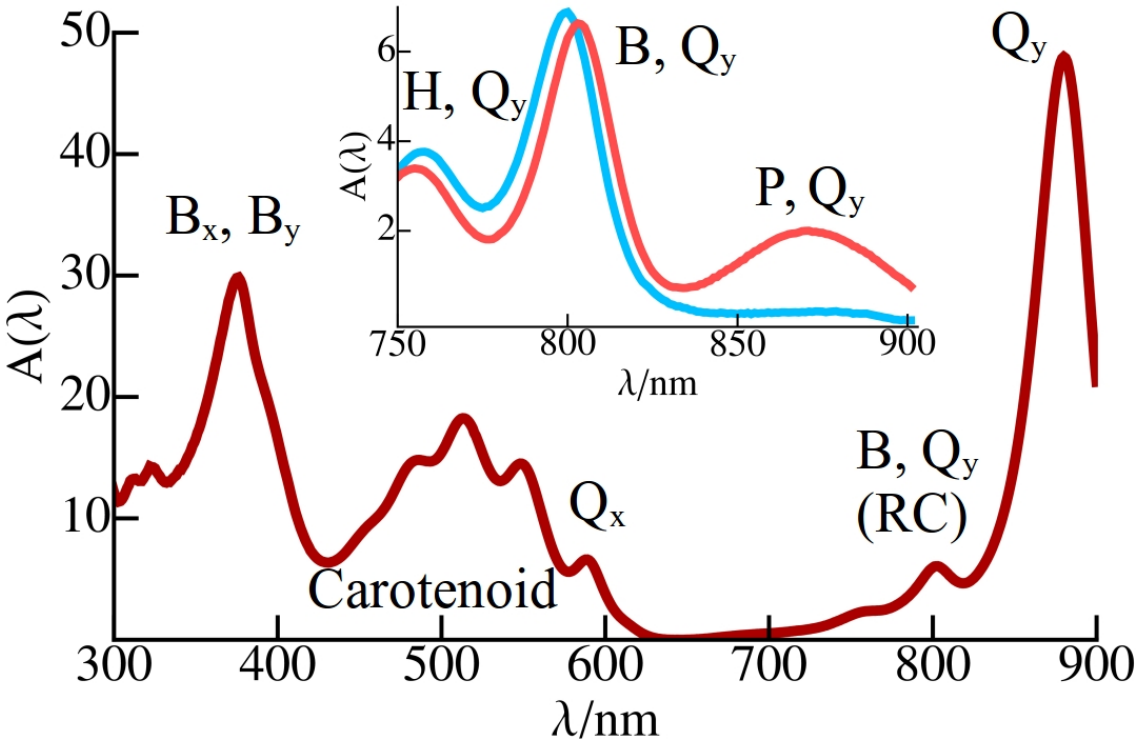

Figure 2.6: Experimentally-measured absorption spectrum of the LH1 core-complex of *R. rubrum*. *(inset)* Measured absorption spectrum of the purified RC of *R. rubrum*. The "dark" and "light" RC spectra, discussed in the main text, are pictured in light-red and light-blue, respectively. Experimental spectra were measured in the group of R. Ghosh (University of Stuttgart).

Hence, if we apply light of sufficiently strong intensity, resulting in the "light" spectrum, photons will excite the RC many times before the cytochrome returns with an electron. Consequently, the 870 nm peak can be completely suppressed, as in Figure 2.6 (B). Conversely, if light of sufficiently low intensity, resulting in the "dark" spectrum, is applied, the P870 band will be visible. A subtraction of "dark" from "light" spectra, as we will do in Ch. 5, leaves only those spectral features which depend on interactions with the P-pigments. In this way, we will be able to isolate changes to the P870 band in the presence of the overwhelming B880 band.

Chapter 3: Theoretical Description of Absorption

As discussed in the last chapter, light-harvesting complexes are composed of bacteriochlorophyll (BChls) which are held in place by a protein scaffold. The proximity of BChl to each other and the fluctuations of the protein– including geometric fluctuations which change the relative orientation of BChl as well as energy level fluctuations due to electric field of the protein– affect the absorption properties of the light-harvesting complex, the main task of this thesis. The close distances ($\sim$ 10 Å), and consequently the strong couplings ($\sim$ 600 cm^{-1}), between bacteriochlorophyll in LH1 means that the states which describe absorption and transfer processes are delocalized. That is, the electronic excitation is shared between multiple pigments. This chapter presents the theoretical framework which describes these delocalized excitations, called excitons, and how they determine properties of the absorption spectrum. The C_{16} symmetry of the complex allows an analytical solution to the eigenvalue problem, and consequently an analytical form for the unbroadened spectral lines, the so-called stick-spectrum. Spectral lines are broadened due to interactions with the protein environment, and we show that a simple dressing of the excitonic stick spectra reproduces exactly the results of a more rigorous calculation using the dipole-dipole correlation function (DDCF). Chapters 4 and 5

use this theory to quantify the small changes in absorption upon (weak) coupling between LH1 complexes and between LH1 and RC.

3.1 The Absorption Spectrum

The main task of this thesis will be to track signatures of weak resonance coupling between light-harvesting units in the absorption spectrum. Biological complexes absorb light due to the interaction of the incident electric field and the induced dipole moment of the BChl. Thinking classically, the field drives oscillations of the classical dipole, and hence the Fourier transform of the two-point correlation function should give the absorption of the field according to the Wiener-Khinchin theorem

$$A(\omega) \propto \int_0^\infty e^{i\omega t} \langle (\vec{E} \cdot \vec{\mu}(t))(\vec{E} \cdot \vec{\mu}(0)) \rangle \, dt \tag{3.1}$$

where $\vec{E}$ is the exciting field and the expectation value of the correlation function is taken in the steady-state of the system. A rigorous derivation of this expression begins with a semi-classical Hamiltonian description of the interaction between light and the electronic degrees of freedom

$$\hat{\mathscr{H}}_{sys-field} = \vec{E}(t) \cdot \hat{\vec{\mu}}, \tag{3.2}$$

where $\hat{\vec{\mu}} = \vec{\mu}|e\rangle\langle g| + H.c.$ is the quantum-mechanical dipole-operator connecting the ground and excited state of the BChl. For a system containing many BChl, the total dipole moment operator is $\hat{\vec{\mu}} = \sum_i \vec{\mu}_i|e_i\rangle\langle g| + H.c.$, where $|e_i\rangle$ corresponds to a single excitation on BChl i. Considering for the moment only electronic degrees of freedom, the full Hamiltonian reads

$$\hat{\mathscr{H}} = \hat{\mathscr{H}}_e + \hat{\mathscr{H}}_{sys-field}. \tag{3.3}$$

Since the incident field is weak, as discussed above, a perturbative expansion in the field is accurate as well as useful. Transforming to the interaction picture with the unitary operator $U_e(t) = e^{i\hat{\mathscr{H}}_e t}$, the dynamics of the density matrix, ρ, of the system obeys the von Neumann equation

$$\dot{\rho}^I(t) = -i\left[\hat{\mathscr{H}}^I_{sys-field}, \rho^I(t)\right], \tag{3.4}$$

which can be solved iteratively. Plugging in the explicit form for the interaction Hamiltonian, the density matrix in the Schrödinger picture is then

$$\rho(t) = \rho^{(0)} + \sum_{n=1}^{\infty} \rho^{(n)}(t) \tag{3.5}$$

$$\begin{aligned}\rho^{(n)}(t) = (-i)^n \int_{t_0}^{t} d\tau_n \int_{t_0}^{\tau_n} d\tau_{n-1} \ldots \int_{t_0}^{\tau_2} d\tau_1 \; \vec{E}(\tau_n)\vec{E}(\tau_{n-1})\ldots\vec{E}(\tau_1)\cdot \\ U_e(t)\left[\hat{\vec{\mu}}(\tau_n), \left[\hat{\vec{\mu}}(\tau_{n-1}), \ldots \left[\hat{\vec{\mu}}(\tau_1), \rho^{(0)}\right]\ldots\right]\right] U_e^{\dagger}(t),\end{aligned} \tag{3.6}$$

where $\rho^{(0)} = \rho(t_0)$ is the density matrix of the system at the initial time t_0 and

$$\hat{\vec{\mu}}(\tau) = U_e^{\dagger}(\tau - t_0)\, \hat{\vec{\mu}}\, U_e(\tau - t_0) \tag{3.7}$$

is the (time-dependent) dipole operator in the interaction picture. The connection between macroscopic observables and the microscopic model is through the expectation value (in the interaction picture) of the macroscopic polarization, given by

$$\vec{P}(t) = Tr\left\{\hat{\vec{\mu}}\rho(t)\right\}, \tag{3.8}$$

which, using Eq. 3.6, Eq. 3.7 and the cyclical property of the trace, is

$$\vec{P}(t) = \vec{P}^{(0)}(t) + \sum_n \vec{P}^{(n)}(t) \tag{3.9}$$

$$\vec{P}^{(n)}(t) = (-i)^n \int_{t_0}^{t} d\tau_n \int_{t_0}^{\tau_n} d\tau_{n-1} \ldots \int_{t_0}^{\tau_2} d\tau_1 \vec{E}(\tau_n)\vec{E}(\tau_{n-1}) \ldots \vec{E}(\tau_1) \cdot \left\langle \hat{\vec{\mu}}(t) \left[\hat{\vec{\mu}}(\tau_n), \left[\hat{\vec{\mu}}(\tau_{n-1}), \ldots \left[\hat{\vec{\mu}}(\tau_1), \rho^{(0)}\right] \ldots\right]\right]\right\rangle. \tag{3.10}$$

The time evolution of the system is here unitary, and, in what follows, will be generated by a Markovian master equation; hence, the time-correlation functions are stationary, meaning their expectation values depends only on the time interval, not the absolute time [48]. Therefore, we set $\hat{\vec{\mu}}(\tau_1) = \hat{\vec{\mu}}(0)$. For the weak illuminating fields used in experiment and experienced by the bacterium under physiological conditions (Rabi frequency/ decay frequency $\sim 10^{-6}$), the steady-state matrix can be safely approximated as the ground state, $\rho^{(0)} \approx |g\rangle\langle g|$. Furthermore, since this

state does not evolve until an interaction with the light field, we can send $t_0 \to -\infty$. Finally, we express Eq. 6.5 in terms of relative time intervals according to $t_k := \tau_{k+1} - \tau_k$ with $t_n = t - \tau_n$ and $\tau_1 = 0$. Using the identities $\tau_k = \sum_i^{k-1} t_i = t - \sum_{i=k}^{n} t_i$, we can rewrite the expectation value of the macroscopic polarization as

$$\begin{aligned}\vec{P}^{(n)}(t) = (-i)^n \int_0^\infty dt_n \int_0^\infty dt_{n-1} ... \int_0^\infty dt_1 \\ \vec{E}(t-t_n)\vec{E}(t-t_n-t_{n-1})...\vec{E}(t-t_n-t_{n-1}...t_1) \\ \cdot \left\langle \hat{\vec{\mu}}(t_n+...+t_1) \left[\hat{\vec{\mu}}(t_{n-1}+...+t_1), \left[\hat{\vec{\mu}}(t_{n-2}+...+t_1), ... \left[\hat{\vec{\mu}}(0), \rho^{(0)}\right] ...\right]\right]\right\rangle .\end{aligned} \tag{3.11}$$

The terms in the time-correlation function of Eq. 3.11 can be understood, ordered and kept track of using two-sided Feynman diagrams. As an example of this formalism, we focus on the first-order polarization $P^{(1)}(t)$ because it leads to the linear absorption spectrum, the central concern of this thesis.

$$\vec{P}^{(1)}(t) = (-i) \int_0^\infty dt_1 \vec{E}(t-t_1) \cdot \left\langle \hat{\vec{\mu}}(t_1) \left[\hat{\vec{\mu}}(0), \rho^{(0)}\right]\right\rangle \tag{3.12}$$

$$= (-i) \int_0^\infty dt_1 \vec{E}(t-t_1) \cdot \left(\left\langle \hat{\vec{\mu}}(t_1)\hat{\vec{\mu}}(0)\right\rangle - \left\langle \hat{\vec{\mu}}(t_1)\hat{\vec{\mu}}(0)\right\rangle^*\right) \tag{3.13}$$

where the last line follows from

$$Tr\{\hat{\vec{\mu}}(t_1)\rho^{(0)}\hat{\vec{\mu}}(0)\} = Tr\{\rho^{(0)}\hat{\vec{\mu}}(0)\hat{\vec{\mu}}(t_1)\} = Tr\{\rho^{(0)\dagger}\hat{\vec{\mu}}^\dagger(0)\hat{\vec{\mu}}^\dagger(t_1)\} \tag{3.14}$$

$$= Tr\{(\hat{\vec{\mu}}(t_1)\hat{\vec{\mu}}(0)\rho^{(0)})^\dagger\} = \left\langle \hat{\vec{\mu}}(t_1)\hat{\vec{\mu}}(0)\right\rangle^* \tag{3.15}$$

Fig. 3.1 shows the Feynman diagram corresponding to absorption, in which the ground state of the system interacts with light at time $\tau_1 := 0$, corresponding to application of the dipole operator on the right or on the left of the system density matrix, depending on the time-ordering of the term in the nested commutator of Eq. 6.5. The interaction creates a ground-excited state coherence, which oscillates at the frequency corresponding to the energy gap. Hence, Fourier transforming the correlation function of the first interaction with the emitted field gives a peak at that frequency– the absorption spectrum. The final interaction with the dipole operator corresponds to the free-induction decay of the excited system, which is the field that is heterodyne detected. That is, the induced polarization emits an electric field which is 90° out of phase

$$\vec{E}^{(1)}(t) \propto -i\vec{P}^{(1)}(t) \tag{3.16}$$

which is heterodyne detected by beating the emitted field with the applied field after spectral separation with a prism or grating, which Fourier transforms the fields

$$A(\omega) \propto log\left(\frac{\left|\vec{E}(\omega)+\vec{E}^{(1)}(\omega)\right|^2}{\left|\vec{E}(\omega)\right|^2}\right) \approx \frac{2Re\left\{\vec{E}(\omega)\cdot\vec{E}^{(1)}(\omega)\right\}}{\left|\vec{E}(\omega)\right|^2}. \tag{3.17}$$

The semi-impulsive limit, in which $\vec{E}(t) \approx \vec{E}\delta(t)$ and therefore $\vec{E}(\omega) = \vec{E}$, allows a simplification of this expression. The absorption spectrum corresponding to ab-

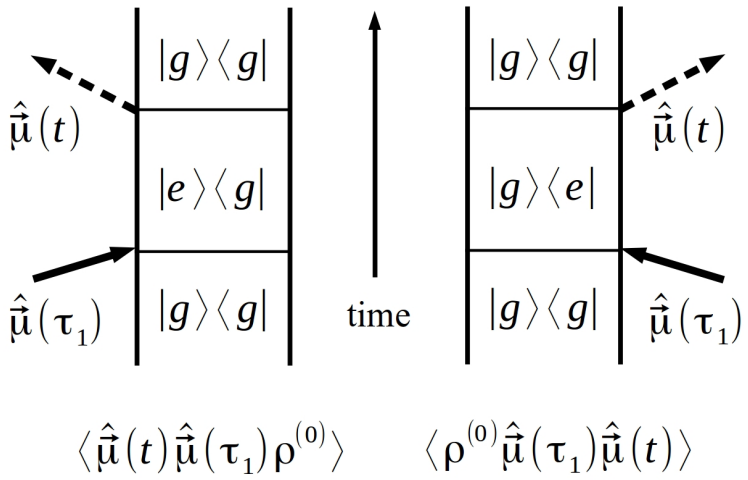

Figure 3.1: Two-sided Feynman diagrams corresponding to absorption.

sorption of light polarized along $\hat{E}$ is then

$$A(\omega) \propto 2Re\{\hat{E}\cdot\hat{E}^{(1)}(\omega)\} = 2Re\left\{\int_0^\infty e^{i\omega t}\left\langle\left(\hat{E}\cdot\hat{\vec{\mu}}(t)\right)\left(\hat{E}\cdot\hat{\vec{\mu}}(0)\right)\right\rangle dt\right\} \quad (3.18)$$

We will also find useful the linear dichroism (LD), which is the difference between the absorption of orthogonally polarized light

$$LD(\phi,\omega) = \frac{A(\phi,\omega) - A(\phi+\pi/2,\omega)}{max\{\langle A(\phi,\omega)\rangle_\phi\}}. \quad (3.19)$$

Where $A(\phi,\omega)$ corresponds to the absorption of light polarized along ϕ. Note that the LD is normalized by the maximum of the unpolarized absorption spectrum, $\langle A(\phi,\lambda)\rangle_\phi$, where the brackets $\langle\rangle_\phi$ correspond to an average over incident polarizations.

3.2 Environmental Effects

The BChl are assembled in a protein scaffold which induces fluctuations in the local electric field and hence the excitation energies. These fluctuations occur on many different time scales, and we divide them, and their effects, into two categories based on their timescale relative to the excitation lifetime. The electronic-vibrational interaction leads to fluctuations of the excitation energy level, which lead to dephasing noise, which destroys electronic coherence, on a sub-picosecond timescale. Dephasing noise does not destroy electronic populations, whose lifetime is of the order or nanoseconds. Pure dephasing process is modelled using a Markovian master equation

$$\dot{\rho} = -i\left[\rho, \hat{H}\right] + \frac{\gamma}{2}\sum_n \sigma_z^n \rho \sigma_z^n - \rho, \tag{3.20}$$

where $\sigma_z^n = |e_n\rangle\langle e_n| - |g_n\rangle\langle g_n|$ and $|g_n\rangle$ ($|e_n\rangle$) is the ground (excited) state of BChl n. Such a Markovian process leads to a decay of the DDCF according to

$$\langle \mu(t)\mu(0)\rangle \sim e^{-t/\tau}. \tag{3.21}$$

where the coherence lifetime is related to the dephasing rate according to

$$\tau = \frac{1}{2\pi\gamma}. \tag{3.22}$$

We will most often take a coherence time of $\tau = 50$ fs which corresponds to a dephasing of $\gamma = 106\ \mathrm{cm}^{-1}$, as this corresponds to measured homogeneous linewidths [49]. The homogeneous absorption spectrum can now be calculated according to Eq. 3.18, where now $\hat{\tilde{\mu}}(t) = e^{\mathcal{L}t}\hat{\tilde{\mu}}(0)$ and the superoperator $\mathcal{L}$ contains all excitonic couplings and the dephasing process. The fast fluctuations lead to a homogeneously-broadened spectral line which, as we will show, is a Lorentzian

$$L(\epsilon) = \frac{1}{\pi}\frac{(1/2\Gamma)^2}{\epsilon^2 + (1/2\Gamma)^2}. \tag{3.23}$$

with full-width at half-maximum (FWHM) $\Gamma = 2 \times 106\ \mathrm{cm}^{-1}$. If the DDCF exhibits Gaussian decay

$$\langle \mu(t)\mu(0)\rangle \sim e^{-(t/\tau)^2}, \tag{3.24}$$

which could be a signature of non-Markovian effects, then the homogeneous lineshape is Gaussian in energy space according to

$$G(\epsilon) = \frac{1}{\sqrt{2\pi\sigma^2}} e^{-\epsilon^2/(2\sigma^2)} \tag{3.25}$$

where the standard deviation is $\sigma = \sqrt{2} \times \gamma$. Slow fluctuations can Stark-shift the excitation energies for the lifetime of the excitation, leading to inhomogeneous broadening of the spectal line. These effects are modeled by performing stochastic averages of the homogeneous absorption spectrum, where the excitation energy of

BChl n is modified to be

$$\epsilon_n \rightarrow \epsilon_n + \xi_n, \tag{3.26}$$

and ξ_n is drawn from a Gaussian distribution of width σ_{inhom}, which is a fit parameter used to reproduce measured spectral widths.

As will be shown in later chapters, calculation of the homogeneous absorption spectrum with the DDCF and a pure dephasing master equation agrees exactly with a simpler, commonly-used protocol according to a Fermi's Golden Rule-type expression

$$A(\omega) \propto \sum_{\alpha} |\vec{D}_{\alpha} \cdot \vec{E}|^2 f(\omega - \omega_{\alpha}) \tag{3.27}$$

which dresses the excitonic stick-spectra with lineshapes f, which are often taken to be Lorentzian. In this formulation, calculation of the spectrum requires only finding a unitary matrix U which diagonalizes the electronic Hamiltonian, $\hat{\mathscr{H}_e}$, and calculation of the excitonic dipole moments $\vec{D}_{\alpha} = \sum_m U_{m,n}\vec{d}_n$, where $\vec{d}_n$ is the dipole-moment of BChl n. Hence, properties of the absorption spectrum are determined by the wave-functions, or shared excitations, called excitons. The next section derives an analytical form for these wavefunctions, and hence the spectrum directly, according to Eq. 3.27.

3.3 Exciton Formalism

Delocalized excitations are characterized using the Frenkel exciton Hamiltonian in the single excitation subspace, which is valid under weak illumination. A correspondence between microscopic structure and optical properties is possible by a theoretical analysis using a Hamiltonian coupling Q_y transition dipoles. Pigments are identified in the site basis with $|m,\zeta\rangle$, where $m \in \{-M/4+1,\ldots,M/4\}$ labels the (dimerized) unit cell ($M = 32$), and $\zeta \in \{1,2\}$ labels the chromophore within the $\alpha\beta$ dimer. For the electronic degrees of freedom, we consider the Hamiltonian

$$\hat{\mathscr{H}_e} = \sum_{m,\zeta} \epsilon_{m,\zeta} |m,\zeta\rangle \langle m,\zeta| + \sum_{(m,\zeta)\neq(m',\zeta')} J_{m,\zeta}^{m',\zeta'} |m,\zeta\rangle \langle m',\zeta'| + H.c. \tag{3.28}$$

where $\epsilon_{m,\zeta}$ is the site energy of BChl (m,ζ) and $J_{m,\zeta}^{m',\zeta'}$ is the interaction energy between pigments (m,ζ) and (m',ζ'). When the details of the charge distribution of excited states are of no importance (center-to-center distances greater than 10 Å), $J_{m,\zeta}^{m',\zeta'}$ can be calculated (in units of cm^{-1}) using the point-dipole approximation:

$$J_{m,\zeta}^{m',\zeta'} = \frac{5042}{\kappa}\left(\frac{\vec{d}_{m,\zeta}\cdot\vec{d}_{m',\zeta'}}{(r_{m,\zeta}^{m',\zeta'})^3} - \frac{3\left(\vec{d}_{m,\zeta}\cdot\vec{r}_{m,\zeta}^{m',\zeta'}\right)\left(\vec{d}_{m',\zeta'}\cdot\vec{r}_{m,\zeta}^{m',\zeta'}\right)}{(r_{m,\zeta}^{m',\zeta'})^5}\right), \tag{3.29}$$

where $\vec{r}_{m,\zeta}^{m',\zeta'} = \vec{r}_{m,\zeta} - \vec{r}_{m',\zeta'}$ (in units of Å), $\vec{d}_{m,\zeta}$ is the Q_y transition dipole moment of BChl (m,ζ) (in units of Debye), and κ is the relative permittivity. The sub-nanometer distance between neighbouring chromophores implies that the nearest-neighbour couplings depend on the geometry of the electronic wave-function of each

chromophore. These couplings can be fitted using fluorescence anisotropy measurements, resulting in $Q_1 = 600\ \text{cm}^{-1}$ and $Q_2 = 377\ \text{cm}^{-1}$ for the intra- and inter-dimer couplings, respectively [50].

The Davydov theory of molecular excitons develops analytic expressions for the exciton states of circularly-symmetric complexes [51]. These states are useful as a basis for deriving exact results and developing a perturbation theory. Modelling the LH1 complex with a C_{16} symmetry suggests expressing the Hamiltonian in the Fourier basis

$$|k,\zeta\rangle = \frac{1}{\sqrt{M/2}} \sum_m e^{i\frac{4\pi}{M}km} |m,\zeta\rangle \tag{3.30}$$

where $k \in \{-M/4+1, ..., M/4\}$. The Hamiltonian coupling elements, when expressed in this basis, decouple for different values of k:

$$\langle k,\zeta| \hat{\mathscr{H}}_e |k',\zeta'\rangle = \frac{1}{M/2} \sum_{m,n} e^{-i\frac{4\pi}{M}(km-k'n+(k'm-k'm))} \langle m,\zeta| \hat{\mathscr{H}}_e |n,\zeta'\rangle \tag{3.31}$$

$$= \frac{1}{M/2} \sum_m e^{i\frac{4\pi}{M}(k-k')m} \sum_n e^{i\frac{4\pi}{M}k'(m-n)} \langle m,\zeta| \hat{\mathscr{H}}_e |n,\zeta'\rangle \tag{3.32}$$

$$= \frac{1}{M/2} \sum_m e^{i\frac{4\pi}{M}(k-k')m} \sum_n e^{i\frac{4\pi}{M}k'(m-n)} \hat{\mathscr{H}}_e^{\zeta,\zeta'}(m-n) \tag{3.33}$$

$$= \frac{1}{M/2} \sum_m e^{i\frac{4\pi}{M}(k-k')m} L_{\zeta,\zeta'}(k') \tag{3.34}$$

$$= L_{\zeta,\zeta'}(k)\delta_{k,k'} \tag{3.35}$$

where

$$L_{\zeta,\zeta'}(k) = \sum_n e^{i\frac{4\pi}{M}kn} \langle 0,\zeta| \hat{\mathscr{H}_e} |n,\zeta'\rangle \,. \tag{3.36}$$

The diagonalisation of the 2×2 Hamiltonians restricted to each k-subspace, $L(k)$, is accomplished with the unitary

$$U(k) = \begin{pmatrix} e^{i\Phi(k)/2}\cos\Theta(k) & e^{i\Phi(k)/2}\sin\Theta(k) \\ -e^{-i\Phi(k)/2}\sin\Theta(k) & e^{-i\Phi(k)/2}\cos\Theta(k) \end{pmatrix}, \tag{3.37}$$

where $\Phi(k) = \arg(L_{01}(k))$ and $\Theta(k) = \frac{1}{2}\arctan\frac{2|L_{01}(k)|}{L_{00}(k)-L_{11}(k)}$ reflect the "amount of dimerization": $\Phi(k)$ captures the difference between intra- and inter-dimer coupling, and $\Theta(k)$ captures the site energy differences. The angle $\Phi(k)$ is plotted in Fig. 3.2(A) for the parameters of the LH1, discussed in the next section. Hence, the Hamiltonian is diagonalized by the exciton wavefunctions

$$|k,\nu\rangle = \sum_{m,\zeta} c^{k,\nu}_{m,\zeta} |m,\zeta\rangle = \frac{1}{\sqrt{M/2}} \sum_{m,\zeta} e^{i\frac{4\pi}{M}km} U(k)_{\alpha,\nu} |m,\zeta\rangle \tag{3.38}$$

and the corresponding dipole moments of the exciton states are

$$\vec{D}_{k,\nu} = \sum_{m,\zeta} c^{k,\nu}_{m,\zeta} \vec{d}_{m,\zeta} \tag{3.39}$$

where $\vec{d}_{m,\zeta}$ is the Q_y transition dipole moment of chromophore m,ζ, Eq. 2.8. Im-

portantly, the dipole moments of the excitons obey a sum rule

$$\sum_{k,\nu} |\vec{D}_{k,\nu}|^2 = \sum_{m,\zeta} |\vec{D}_{m,\zeta}|^2. \tag{3.40}$$

Let U be a unitary matrix which diagonalizes the Hamiltonian, then:

$$\begin{aligned}
\vec{D}_k &\equiv \sum_n U_{n,k} \vec{D}_n \\
\sum_k |D_k|^2 &= \sum_k \sum_{m,n} \vec{d}^*_m \cdot \vec{d}_n \, U_{n,k} U^*_{m,k} = \sum_{m,n} \vec{\mu}^*_m \cdot \vec{d}_n \sum_k U_{n,k} U^\dagger_{k,m} \\
&= \sum_{m,n} \vec{d}^*_m \cdot \vec{d}_n \delta_{m,n} = \sum_m |\vec{d}_m|^2.
\end{aligned}$$

Intuitively, this means that the total absorption of the complex remains constant, it can be only redistributed among different states due to coherent coupling.

3.3.1 LH1 Excitons

We consider a simplified model for the LH1 geometry, parameterized by Eq. 2.8 and 2.9, and the energy landscape, which yields analytical expressions with quantitative insight. Considering degenerate dimers ($\epsilon_2 - \epsilon_1 \approx 10$ cm$^{-1} \ll Q_1 \approx 600$ cm^{-1}) and taking into account only nearest-neighbour coupling, the matrix L takes

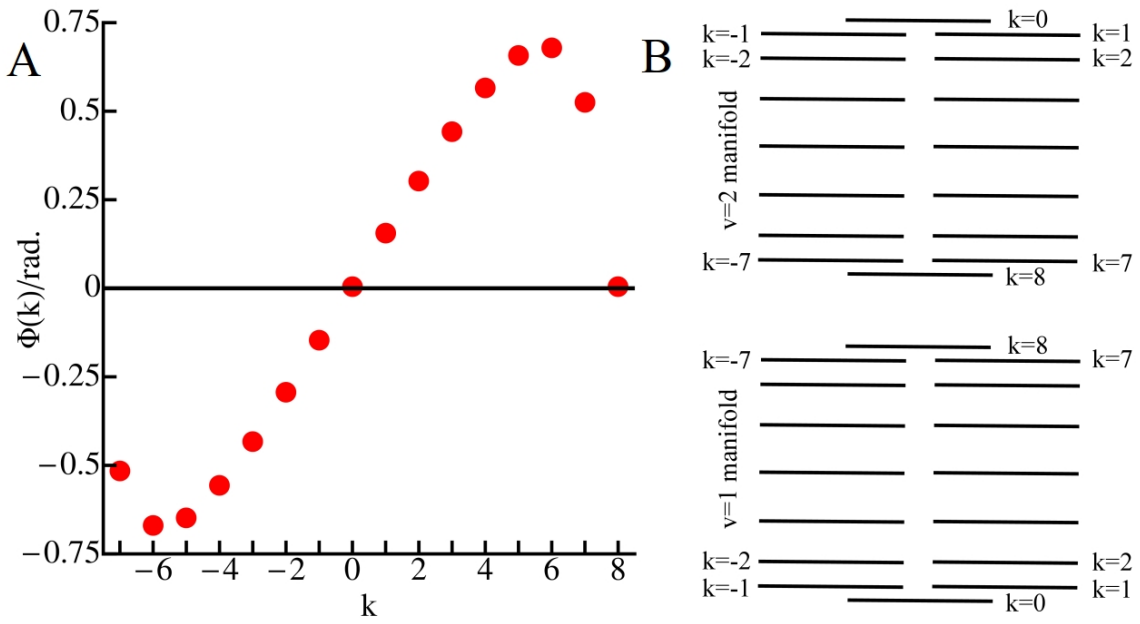

Figure 3.2: (A) The Davydov angle $\Phi(k)$ for the simple example of Eq. 3.42. This angle captures effects of dimerization on the exciton states. It is small for the bright states $k = \pm 1$. (B) LH1 energy level structure of Eq. 5.8. The two-fold degeneracy and manifold splitting of $2(Q_1 - Q_2)$ are signatures of the circular symmetry and dimerization, respectively.

on a particularly simple form

$$L(k) = \begin{pmatrix} \epsilon & Q_1 + Q_2 e^{i\frac{4\pi}{M}k} \\ Q_1 + Q_2 e^{-i\frac{4\pi}{M}k} & \epsilon \end{pmatrix} \tag{3.41}$$

where ϵ, Q_1, Q_2 are site energies, and intra-dimer and inter-dimer couplings, respectively. Accordingly,

$$\begin{aligned} \Theta(k) &= \frac{\pi}{4} \\ \Phi(k) &= \arctan \frac{Q_2 \sin \frac{4\pi}{M}k}{Q_1 + Q_2 \cos \frac{4\pi}{M}k}. \end{aligned} \tag{3.42}$$

The Hamiltonian is diagonalized by the exciton wavefunctions $|k,\nu\rangle$, leading to dipole moments $\vec{D}_{k,\nu}$ and energies $E_{k,\nu}$

$$\vec{D}_{k,1} = \delta_{k,\pm1} d^{LH1} \sqrt{M/2} \cos\left(\frac{\Phi(1)-\gamma}{2}\right) \frac{e^{\pm i\Delta\gamma}}{\sqrt{2}} \begin{pmatrix} \mp\frac{i}{\sqrt{2}} \\ \frac{1}{\sqrt{2}} \end{pmatrix} \tag{3.43}$$

$$\vec{D}_{k,2} = \delta_{k,\pm1} d^{LH1} \sqrt{M/2} \sin\left(\frac{\Phi(1)-\gamma}{2}\right) \frac{e^{\pm i\Delta\gamma}}{\sqrt{2}} \begin{pmatrix} \frac{1}{\sqrt{2}} \\ \mp\frac{i}{\sqrt{2}} \end{pmatrix} \tag{3.44}$$

$$E_{k,\nu} = \epsilon + (-1)^{\nu} \left(Q_1 + Q_2 \cos\left(\frac{4\pi}{M}k\right)\right), \tag{3.45}$$

The circular symmetry is manifest in the two-fold degeneracy $E_{k,\nu} = E_{-k,\nu}$ and the dipole selection rule $\vec{D}_{k,\nu} \propto \delta_{k,\pm1}$, and the dimerization in the splitting by $2(Q_1 - Q_2)$ of the energies into two bands, denoted by ν, see Fig. 3.2 (B).

The concentration of dipole strength in the upper and lower bands is a function of $\Phi(1) - {}^{2\pi}/_{32} \approx 0$, which reflects the amount of dimerization. As $Q_1 \to Q_2$, $\Phi(1) \to {}^{2\pi}/_{32}$ and, consequently, more dipole strength is distributed in the lower band. For the LH1, more than 99% of the total absorbing strength is in the low-lying $|k = \pm1, 1\rangle$, since $(\Phi(1) - 2\pi/32)/2 \approx$ -0.02 according to Fig. 3.2 (A). The dipole selection rule, which concentrates dipole strength in the $k = \pm1$, $\nu = 1$ manifold, means that the absorption properties of the single LH1 rings, as well as aggregates of LH1s and LH1-RC complexes, are determined by these states. We will show that effects of coupling outside this manifold can be neglected because of either (1) selection rules or (2) the states outside of this manifold will be off-resonance with the states of interest. Hence, in what follows we will drop the subscript ν and con-

sider only the $k = \pm 1$ states. Full numerical simulations will consider a microscopic structural model and all states.

3.3.2 Special Pair Excitons

The $P870$ band corresponds to absorption by the anti-symmetric superpostion of special pair states since the dipole moments of the P-pigments are nearly anti-parallel according to Eq. 2.11. This bright special pair state is modeled by

$$\vec{r}_{P870} = \begin{pmatrix} 0 \\ \\ 0 \end{pmatrix} \qquad \vec{D}_{P870} = \sqrt{N} d^P \begin{pmatrix} 1 \\ \\ 0 \end{pmatrix} \tag{3.46}$$

where $N = 2$.

Chapter 4: Optical Signatures of Quantum Delocalization over Extended Domains in Photosynthetic Membranes

This chapter applies the exciton formalism of Ch. 3 to characterize absorption in arrays of circular LH complexes. Figure 4.1 shows that LH1 and LH2 complexes exhibit diverse assemblies and structures across species and growth conditions. In particular, the relative proportion of LH2 to LH1 in *Rsp. photometricum* and *R. blasticus*, closely related to the well-studied *R. sphaeroides*, depends on the light conditions during growth, an adaptation that balances excitation trapping and dissipation [52]. As the distance between LH complexes is much greater than the distance between BChl within single complexes, the effects of the weak excitonic coupling *between* LH complexes during absorption have been unexplored. This weak coupling breaks the circular symmetry of excitons confined to a single ring, and therefore leads to an optical response that is sensitive to polarization. In particular, the linear dichroism (LD), the difference in absorption of orthogonally polarized light, witnesses this small coupling. The details are given in the following published paper [26] after a few summary remarks.

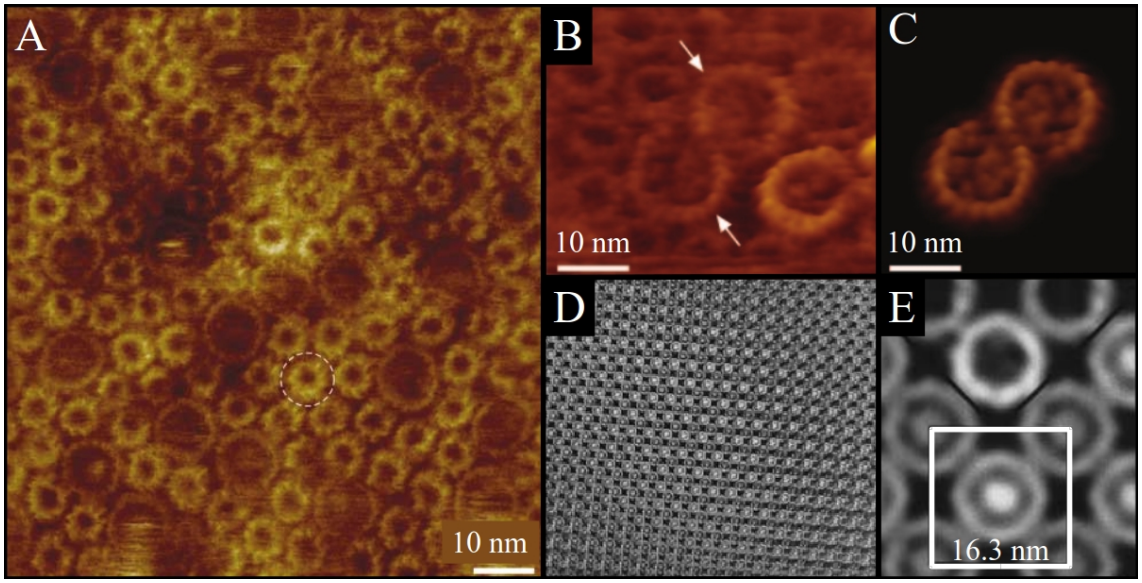

Figure 4.1: (A) *[reproduced from Ref. [53]]* AFM topograph of a native high-light-adapted photosynthetic membrane in *Rsp. photometricum*. The large LH1 rings are randomly interspersed between LH2 rings. (B-C) *[reproduced from Ref. [54]]* AFM topograph of periplasmic surface of *R. blasticus*. The LH1s are open rings and dimerize due to the presence of the PufX protein. (D-E) *[reproduced from Ref. [55]]* Electron micrograph of reconstituted, crystallized LH1s (in detergent) of *R. rubrum*. This purple bacterial species contains only LH1 complexes. In all species, the RC sits inside the LH1 ring. However, the LH1 of *R. rubrum* can be crystallized (E) without the RC.

According to the analysis of circular complexes in Ch. 3, the absorption spectrum is determined by two states, labelled $k = \pm 1$. Hence, the polarized absorption and LD is, according to Eq. 3.27 and Eq. 3.19 is

$$A(\omega, \phi) \propto |\vec{D}_{k=1} \cdot \hat{E}|^2 f(\omega - \omega_{k=+1}) + |\vec{D}_{k=-1} \cdot \hat{E}|^2 f(\omega - \omega_{k=-1}) \tag{4.1}$$

$$LD(\omega, \phi) \propto A(\omega, \phi) - A(\omega, \phi + \pi/2) \tag{4.2}$$

where $\hat{E} = \cos\phi\,\hat{x} + \sin\phi\,\hat{y}$ is the polarization unit-vector of the incident light, assumed to be travelling along the z-axis perpendicular to the plane of the ring, and

f is a homogeneous lineshape function. For a single, circular complex the $|k = \pm 1\rangle$ states are degenerate in energy ($\omega_{k=+1} = \omega_{k=-1} \equiv \omega_1$), carry equal dipole strength and are orthogonally polarized according to Eq. 5.6

$$\vec{D}_{k=\pm 1} \propto \begin{pmatrix} \pm i \\ \\ 1 \end{pmatrix}. \tag{4.3}$$

Hence, $\vec{D}_{k=\pm 1} \cdot \hat{E}$ is a pure phase and the polarized absorption and LD of a single, circular LH complex are

$$A(\omega, \phi) \propto f(\omega - \omega_1) \tag{4.4}$$

$$LD(\omega, \phi) \propto 0. \tag{4.5}$$

That is, the circular symmetry, or more specifically the 90° rotational symmetry, of the complex is reflected in the vanishing LD. The following paper shows that upon coupling between two LH complexes, the new eigen-wavefunctions, now delocalized over two rings, concentrate dipole moment again in two states

$$|\pm\rangle = \frac{1}{2}\big(|k = 1\rangle_1 \pm |k = -1\rangle_1 \big) + \frac{1}{2}\big(|k = 1\rangle_2 \pm |k = -1\rangle_2 \big) \tag{4.6}$$

$$\vec{D}_+ \propto \begin{pmatrix} 0 \\ \\ 1 \end{pmatrix} \qquad \vec{D}_- \propto \begin{pmatrix} 1 \\ \\ 0 \end{pmatrix} \tag{4.7}$$

where $|k = \pm 1\rangle_i$ is a single ring exciton on ring i. The other two eigenstates formed

from the $k = \pm 1$ manifolds

$$|\pm\rangle_{\emptyset} = \frac{1}{2}\big(\,|k=1\rangle_1 \pm |k=-1\rangle_1\,\big) - \frac{1}{2}\big(\,|k=1\rangle_2 \pm |k=-1\rangle_2\,\big) \tag{4.8}$$

carry no dipole strength. The bright $|\pm\rangle$ states are shifted with respect to each other in energy, leading to a splitting of peaks in the absorption spectrum

$$A(\omega,\phi) \propto \cos^2\phi\, f(\omega - \omega_1 - \frac{\delta\omega}{2}) + \sin^2\phi\, f(\omega - \omega_1 + \frac{\delta\omega}{2}) \tag{4.9}$$

and a non-zero LD along the line connecting the two complexes

$$LD(\omega,0) \propto f\left(\omega - \omega_1 - \frac{\delta\omega}{2}\right) - f\left(\omega - \omega_1 + \frac{\delta\omega}{2}\right). \tag{4.10}$$

In general, an assembly which does not exhibit 90° rotational symmetry will lead to a non-zero LD. As the splitting $\delta\omega$ is proportional to the resonance coupling between rings, a measurement of the LD is a direct measurement of this coupling. The following paper contains details regarding the effects of homogeneous and inhomogeneous broadening, which affect the absorption lineshape and the LD contrast.

A complete understanding of the primary processes of photosynthesis, from light absorption to charge separation, requires insight into the incoherent transfer rates in and between all constituents– LH1, LH2 and RC– in the complete core complex. Generalized Förster theory is often used to calculate the incoherent rate

$\gamma_{k\to k'}$ from a donor exciton k to acceptor exciton k'

$$\gamma_{k\to k'} = \frac{2\pi}{\hbar}|V_{k,k'}|^2\, Z_k\, I_{k,k'}, \tag{4.11}$$

where $V_{k,k'}$ is the resonance coupling between excitons, Z_k is the thermal population (Boltzmann factor) and $I_{k,k'} = \int_0^\infty F_k(\epsilon)A_{k'}(\epsilon)d\epsilon$ denotes the spectral overlap integral of the donor fluorescence from exciton k and acceptor absorption of exciton k', F and A, respectively [56, 57]. Under some assumptions regarding the homogeneity of absorption and emission, discussed in the following paper, transfer occurs predominantly between $|k = \pm 1\rangle$ states, and hence the transfer rate between iso-energetic circular complexes is determined by exactly that coupling which can be read off from the LD spectrum. The most exciting finding of the following paper is that the LD can therefore provide a novel, straightforward if indirect method to estimate the incoherent transfer rate between iso-energetic LH complexes.

THE JOURNAL OF PHYSICAL CHEMISTRY A

Article

pubs.acs.org/JPCA

Optical Signatures of Quantum Delocalization over Extended Domains in Photosynthetic Membranes

Christopher A. Schroeder,[†,‡,¶] Felipe Caycedo-Soler,[†,¶] Susana F. Huelga,[†] and Martin B. Plenio*[,†]

[†]Institute of Theoretical Physics, University of Ulm, Albert-Einstein-Allee 11, D-89069 Ulm, Germany

[‡]Joint Quantum Institute, Department of Physics, University of Maryland and National Institute of Standards and Technology, College Park, Maryland 20742, United States

Supporting Information

ABSTRACT: The prospect of coherent dynamics and excitonic delocalization across several light-harvesting structures in photosynthetic membranes is of considerable interest, but challenging to explore experimentally. Here we demonstrate theoretically that the excitonic delocalization across extended domains involving several light-harvesting complexes can lead to unambiguous signatures in the optical response, specifically, linear absorption spectra. We characterize, under experimentally established conditions of molecular assembly and protein-induced inhomogeneities, the optical absorption in these arrays from polarized and unpolarized excitation, and demonstrate that it can be used as a diagnostic tool to determine the resonance coupling between iso-energetic light-harvesting structures. The knowledge of these couplings would then provide further insight into the dynamical properties of transfer, such as facilitating the accurate determination of Förster rates.

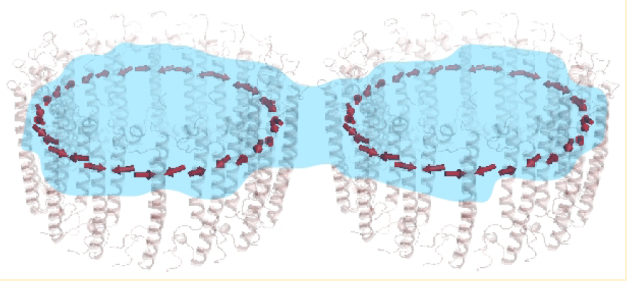

INTRODUCTION

Nature has evolved a variety of photosynthetic architectures. A detailed, quantitative understanding of the principles that underly their function could assist the design of future energy conversion devices. A wealth of careful structural and spectral studies[1−6] complemented by first principle calculations[7−10] have contributed to our current understanding of exciton transfer dynamics in light-harvesting (LH) antenna and reaction center (RC) pigment−protein complexes. Recently, interest in this topic has intensified due to observations of persistent oscillatory features in nonlinear optical experiments,[11−17] which have been reproduced in various LH structures. This has motivated work that reevaluates the nature of the interaction between excitonic dynamics and vibrational motion.[18−20]

Recent work has examined excitonic delocalization restricted to closely packed pigments in single LH units.[8,22,23] This approximation is valid for studies of intercomplex energy transfer and fluorescence, which take place on time scales (approximately picosecond to nanosecond) much longer than the dephasing (∼100 fs), which reduces the excitons to localized (single-unit) domains.[10,24,25] However, as we will show, for processes that are characterized through observables with a faster built-in time scale, such as absorption, which depends on the dipole−dipole correlation function (DDCF) oscillating at optical frequencies, extended delocalization across LH complexes must be taken into account in an accurate description.[26] Here, we propose and characterize theoretically an experimental scheme, based on simple linear absorption measurements, which quantifies the resonance coupling among LH complexes in purple bacteria. On the basis of firm theoretical analysis, we show how this information facilitates the determination of incoherent excitonic transfer rates in systems where the donor's fluorescence and acceptor's absorption overlap.

MATERIALS AND METHODS

Purple Bacteria. Photosynthetic membranes of purple bacteria are composed, in general, of two-dimensional arrays of LH1 and LH2 complexes, which are responsible for the absorption of light and the subsequent transport of excitation energy to RC pigments, where charge separation drives metabolism under photosynthetic growth conditions.[2−4,6,7,27−30] In such membranes, excitonic energy transfer among LH1 and LH2 units has been characterized in terms of incoherent (thermal) hopping.[31] However, for a description of absorption, which has a much faster built-in time scale than intercomplex energy transfer and dephasing, excitonic delocalization across several harvesting complexes may become relevant. In this work, we analyze excitonic delocalization across many LH complexes. We will show that this delocalization leads to a redistribution of absorption intensity that is experimentally accessible by exploiting the symmetry of LH1 and LH2 complexes.

Received: May 20, 2015
Revised: August 7, 2015

DOI: 10.1021/acs.jpca.5b04804
J. Phys. Chem. A XXXX, XXX, XXX−XXX

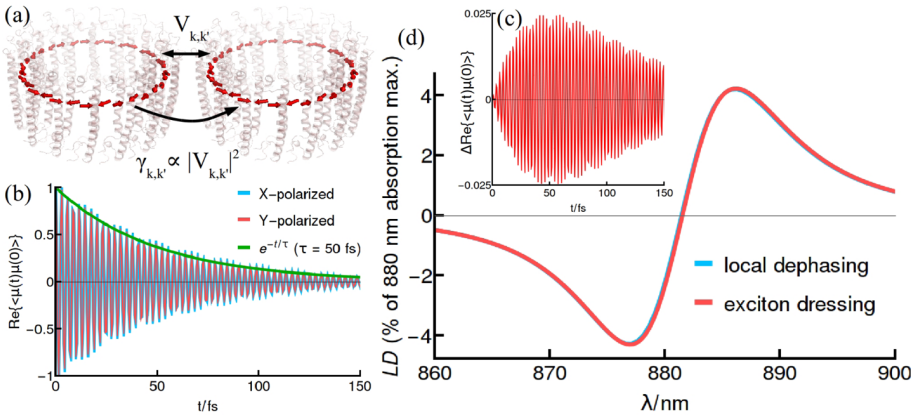

Figure 1. (a) Q_y transition dipole moments (red arrows) of the BChl pigments and the protein scaffold (light red) of the LH1 complex in *R. rubrum*, are pictured schematically.[21] The rate of incoherent energy transfer between excitons k and k' on different LH complexes, $\gamma_{k,k'}$, is determined by the resonance coupling $V_{k,k'}$, as explained in the main text. (b) Oscillating dipole−dipole correlation function (DDCF) contains all signatures of the resonance coupling and decays due to decoherence, which leads to homogeneous spectral broadening. The difference between the $\hat{x}$- and $\hat{y}$-polarized correlation functions (c) contains the signatures of coupling between rings, $V_{k,k'}$, and can be obtained experimentally by measuring (d) the linear dichroism (LD), which is the difference between polarized absorption along these orthogonal axes. Importantly, the effects of local dephasing on the LD can be reproduced by both the DDCF, eq 2, or a simple dressing of excitonic states according to eq 3.

For concreteness, we develop our analysis using the LH1 of *Rhodospirillum rubrum*, whose assumed homology of LH1 to LH2 harvesting units permits a straightforward generalization to membranes composed of either complex. The available X-ray structure of the LH1 complex from *Thermochromatium tepidum*[32] and vanishing fluorescence anisotropy of LH 1s in *R. rubrum*[33] provide support for a closed ring structure with dimeric repeating units of $2N = 32$ bacteriochlorophyll (BChl) pigments in a C_{16}-fold symmetry, as depicted schematically in Figure 1a, although not all LH1 complexes are closed or circular.[34] LH1 complexes from *R. rubrum* naturally aggregate via protein domain-mediated interactions into arrays with a tetragonal packing and can be grown without the constituent RCs.[2] Due to symmetry, the complex develops a single bright band at 880 nm, which, in the case of *R. rubrum*, has 2.4 times the dipole strength from what is expected from the addition of 32 dipoles $\vec{d}$.[35,36] Such hyperchromism is accounted for by increasing the magnitude of the induced dipoles $|\vec{d}_i| \rightarrow |\sqrt{2.4} \times \vec{d}| = \sqrt{2.4} \times 6.3$ Debye = 9.8 D. In *Rhodobacter sphaeroides*, LH1 complexes tend to dimerize.[2−4]

Exciton Formalism. Excitonic properties of membranes subject to low-intensity illumination can be obtained from the electronic Hamiltonian in the single excitation subspace:

$$\mathcal{H} = \sum_m \epsilon_m |m\rangle\langle m| + \sum_{m \neq n} J_{mn} |n\rangle\langle m| \tag{1}$$

where ϵ_m is the excitation energy of pigment m and J_{nm} is the coupling, through the Coulomb exchange mechanism, between the Q_y induced transition dipoles, $\vec{d}_m$, of the electronic excited states $|n\rangle$ and $|m\rangle$ on pigments n and m.[37] Details of the coherent interaction lead to specific eigen-frequencies ω_α from eigenstates $|\alpha\rangle = \sum_n c_n^\alpha |n\rangle$, in general, delocalized over the complete set of pigments accounted for (see Supporting Information for Hamiltonian parameters). In general, the resonance coupling between different rings, labeled $V_{k,k'}$ in Figure 1a, is the origin of electronic energy transfer (EET), which is well-described as an incoherent process between *different* rings (occurring at a rate $\gamma_{k,k'} \propto |V_{k,k'}|^2$).[38] The key prediction of this article, illustrated in Figure 1, is that this resonance coupling introduces experimentally accessible signatures in the linear absorption, which evidence excitonic delocalization across different rings and can be used to obtain estimates of the EET rates $\gamma_{k,k'}$.

The absorption spectrum $A_{\hat{E}}(\omega)$ along an excitation polarization direction $\hat{E}$ is obtained from the Laplace−Fourier transform of the DDCF, $\langle(\vec{D}(t)\cdot\hat{E})(\vec{D}(0)\cdot\hat{E})\rangle$,[39]

$$A_{\hat{E}}(\omega) = \int_0^\infty \langle(\vec{D}(t)\cdot\hat{E})(\vec{D}(0)\cdot\hat{E})\rangle e^{i\omega t}\, dt$$

$$\approx \int_0^\infty \mathrm{Tr}\{(e^{\mathcal{L}t}\vec{D}(0)\cdot\hat{E})\vec{D}(0)\cdot\hat{E}\}e^{i\omega t}\, dt \tag{2}$$

$$\approx \sum_\alpha |\vec{D}_\alpha\cdot\hat{E}|^2 f(\omega - \omega_\alpha) \tag{3}$$

The propagator $e^{\mathcal{L}t}$ contains all excitonic couplings and dispersive processes of relevance for excitonic dynamics. Within the DDCF description, the evolution of the dipole moment operator $\vec{D}(t) = e^{\mathcal{L}t}\vec{D}(0) = e^{\mathcal{L}t}\sum_i \vec{d}_m |m\rangle\langle 0|$ leads to oscillations at optical frequencies $\propto e^{i\omega_\alpha t}$ with a period of about ≈2−3 fs, due to the Hamiltonian part of the propagator. These coherent signatures are degraded by environmental decoherence, which in the worst-case scenario (in terms of processes that degrade the excitonic delocalization), may lead to independent fluctuations of pigment energies ω_i within the excitation's lifetime, local pure dephasing, occurring on a time scale of γ_d^{-1} ≈ 50−100 fs.[40,41]

The DDCF evolves for many tens of optical cycles, as seen in Figure 1b, before dephasing sets in, which can be sufficient to imprint in the absorption spectra features of excitonic coupling, i.e., excitonic delocalization among several LH units. Such features are difficult or impossible to observe in processes with a longer built-in time scale, such as EET. Our interest is to connect the optical signatures from this DDCF with excitonic delocalization across *multiple* rings. To be conservative, we initially consider the worst-case scenario for degradation of such extended excitonic delocalization, introduced by a local dephasing superoperator of the form $\mathcal{L}_d\rho = \sum_m \frac{\gamma_d}{2}(\sigma_z^m\rho\sigma_z^m - \rho)$, with $\sigma_z^m = |m\rangle\langle m| - |0\rangle\langle 0|$ and the density operator ρ, consistent with random temporal fluctuations of the energy gap

DOI: 10.1021/acs.jpca.5b04804
J. Phys. Chem. A XXXX, XXX, XXX−XXX

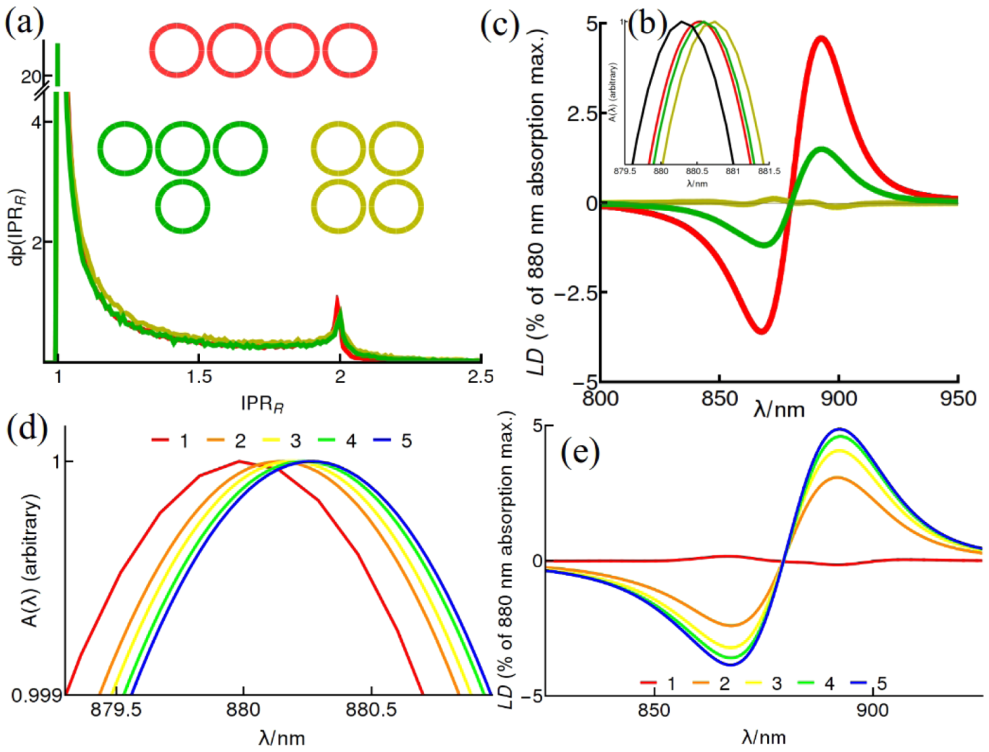

Figure 2. Extended delocalization across multiring arrays in different multiple-ring configurations. Each four-ring configuration considered in (a) exhibits a similar, although not identical, extent of delocalization, measured by the ring inverse participation ratio IPR_R. Plotted is the probability distribution, $dp(IPR_R)$, of the IPR_R of the exciton state with greatest dipole strength, averaged over realizations of static disorder. The average delocalization length, $\langle IPR_R \rangle$, increases slightly with the number of neighbors, i.e., $\langle IPR_R \rangle = \{1.24, 1.27, 1.33\}$ for the line, T, and square configurations, respectively. However, the delocalization is witnessed by linear dichroism (LD) only when the assembly exhibits an asymmetry, like in the T and line assemblies, as shown in (c). (d) Red-shifted absorption and (e) nonzero linear-dichroism (LD) for linear arrays ($Q = 1$, calculated for different values of $R = 1, ..., 5$) witness extended delocalization over multiple LH1 complexes. Results from 5×10^4 realizations of site-energy variations with standard deviation 325 cm^{-1} and $\gamma_d = 1/50$ fs^{-1}.

between levels $|m\rangle$ and the electronic ground state $|0\rangle$. When derived from a microscopic approach, the considered dephasing model describes the action of a fully Markovian environment in the infinite temperature limit. The vectorial nature of the dipole moment $\vec{D}$ permits discrimination of absorption along the axis that joins two coherently coupled rings and perpendicular to it, based upon the calculation of the respective DDCF of Figure 1b. The subtraction of these two signals, presented in Figure 1c, shows that their DDCF differ, a fact made even more conspicuous by the subtraction of absorption spectra (through the Laplace–Fourier transform from eq 2) corresponding to these orthogonal directions, namely, the linear dichroism (LD). This result should be contrasted with the vanishing LD of single circular rings, or equivalently, assemblies of rings where the resonance coupling between rings plays no role, as discussed below. As these calcuations show, strong local dephasing with a rate of $\gamma_d = 1/50$ fs is not enough to smear out the finite LD for the coupled rings, and displays the robustness of optical measures for understanding the extent of excitonic delocalization in photosynthetic membranes. Reassuringly, the result obtained from the local dephasing model is virtually indistinguishable from the usual procedure illustrated by eq 3, in which excitonic energies ω_α are used as the center of a dressing function $f(\omega - \omega_\alpha)$, whose weight in the complete absorption spectrum is determined by the exciton dipole strength $|\vec{D}_\alpha \cdot \hat{E}|^2$. This agreement justifies the reduction of the complexity of the DDCF calculation to a simple diagonalization of the full Hamiltonian and the use of Lorentzian line-shape functions $f(\omega) = \gamma_d^2/(\omega^2 + \gamma_d^2)$, to establish the influence of the electronic coherent coupling in polarized absorption spectra. Moreover, it emphasizes the necessity of the excitonic dipole strength $|\vec{D}_\alpha|^2$, and therefore the relevance/necessity of excitonic states $|\alpha\rangle$, for the description/understanding of the absorption process in ring assemblies.

RESULTS AND DISCUSSION

Excitons $|\alpha\rangle$ are affected by their interactions with the protein environment, which dynamically degrade the electronic coherence within the excitation lifetime (homogeneous broadening) captured by either $\mathcal{L}_d$ or the dressing procedure, and quasi-static fluctuations (inhomogeneous broadening) of the excitation energy and the Coulomb coupling. An interplay between both types of broadening leads to the observed width of the absorption spectrum, which in the case of LH1 is approximately $\Gamma \approx 465$ cm^{-1}. If the homogeneous line shape function is consistent with a dephasing lifetime of $\gamma_d = 1/50$ fs, a standard deviation of a Gaussian pigment site-energy variation of 325 cm^{-1} is required to recover the full width of the LH1 absorption (further details in the Supporting Information). This latter value is in agreement with previous estimations.[24,42−46]

Extended Delocalization: Absorption and LD as a Witness of Delocalization in Ring Assemblies. The relevance of the excitonic dipole strength $|\vec{D}_\alpha|^2$ for the description of the optical response of ring assemblies motivates our study of the excitons $|\alpha\rangle$ in multiple ring arrays.

DOI: 10.1021/acs.jpca.5b04804
J. Phys. Chem. A XXXX, XXX, XXX−XXX

To estimate the influence of inhomogeneities on the extent of excitons, the usual inverse participation ratio[9,47,48] is generalized to quantify delocalization *across* rings R of a given exciton α, namely, the ring participation ratio $\mathrm{IPR}_R^\alpha = 1/\sum_{M=1}^{R}(\sum_{n\in M}^{2N}|c_n^\alpha|^2)^2$. The IPR_R ranges from 1 to R, and $\mathrm{IPR}_R > 1$ unequivocally represents excitonic delocalization over more than a single ring. An estimation of the size of excitons in each of the three configurations presented in Figure 2a shows that absorption in these arrays generates excitons that in general extend over domains larger than a single ring. This figure also shows that excitons have similar sizes for a fixed set of coherently coupled rings. In more detail, small differences emerge from the specific connectivity of each configuration, setting the square, T-like and linear configurations with exciton sizes in descending order. Importantly, the histogram of IPR_R of Figure 2 is made upon the two most optically active states from every noise realization and therefore represents the accessible states through optical excitation.

For uncoupled LH1 complexes, the circular symmetry leads to an optical response predominantly determined by two orthogonally polarized degenerate exciton states and vanishing LD.[26,33,49,50] However, the coherent excitonic interaction between rings may lift such a symmetry and result in shifts in the unpolarised absoprtion spectrum and/or to a finite LD. The key theoretical predictions of this article are summarized in Figure 2b–e. Namely, a shift in the unpolarised absorption spectra will generally be observed in assemblies of many rings, whereas a nonzero LD will be measured in arrays with a large aspect ratio and small width, i.e., linear-like arrays.

A close inspection of the absorption spectrum (Figure 2b) of the configurations from the inset of Figure 2a, shows very similar spectra for the T-like and linear configurations, whereas the square assembly does present a larger shift to the red than the former geometries, in comparison to the spectrum from a single ring. In practice, shifts that account for fractions of nanometers can be difficult to discriminate and a complementary measure, namely, the LD, can be of help to understand whether the shifts observed are compatible with excitons formed across several rings. Even though all these structures present a finite shift with respect to the single ring spectrum, notice, however, that not all multiple-ring arrangements present a finite LD. For instance, the symmetric square assembly, which presents the greatest IPR_R, has vanishing LD, whereas the linear array shows a LD with a contrast of ≃4−5% of the absorption maximum. From these results it is apparent that, although each assembly presents similar delocalization and shifts in the unpolarised absorption, asymmetric assemblies provide a suitable scenario for the experimental observation of excitonic delocalization using polarized spectroscopy. When the focus is placed in the linear-like arrays, it is observed that unpolarized absorption spectra show greater shifts in Figure 2d with an increase of the number of rings in the linear array. Interestingly, the amplitude of the LD also increases with the linear array size, from ≈2.5% for two rings, rising up until it seems to saturate to ≈5% for five rings.

It must be highlighted that just due to homogeneous broadening, the LD amplitude for two rings is about 5% whereas if the inhomogeneities are included, it reduces to about 2.5% of the total spectra. We have tested that this latter value is robust to different compositions of homogeneous and inhomogeneous broadening restricted to the same full broadening of the optical transition. The inhomogeneities in a sample may not be restricted to environmentally induced inhomogeneities in the pigment energies and can indeed be caused by structural perturbations, such as variations in the intercomplex distance or geometrical perturbations that produce ellipticity. A thorough study of both effects is presented in the Supporting Information, from where it can be concluded that the specific details of the broadening mechanisms do not play an important role for the determination of the LD amplitude.

These full numerical simulations of the polarized and unpolarized absorption spectrum highlight (1) in general, (small) shifts in the absorption spectra are expected in arrays of rings; (2) a finite LD, in particular for linear-like assemblies, will be observed due to the coherent coupling of the rings, and (3) the contrast of the LD depends inversely on the total broadening of the optical transition and not on the specific details of the broadening mechanism.

Analytical Expressions. To understand which quantities determine both the shifts in the unpolarized spectrum and the LD, an analytical model is desirable. In the absence of inhomogeneities, the optical response of circular aggregates, resembling LH1 or LH2 rings, is determined by the $|k = \pm 1\rangle = \frac{1}{\sqrt{2N}}\sum_n (-1)^n \exp(2\pi i k \lfloor n/2 \rfloor / N)|n\rangle$ states, where $\lfloor n/2 \rfloor$ is the largest integer smaller than $n/2$. These states carry all the transition dipole moment, namely, $\vec{D}_{k=\pm 1} \approx |\vec{d}|\sqrt{\frac{N}{2}}(\hat{x} \pm \hat{y})$, where $\hat{x}$ and $\hat{y}$ denote orthonormal axes to be identified with those shown in Figure 3a. The inter-ring resonance coupling $V_{k,k'} = \langle k, \vec{e}|\mathcal{H}|k', \vec{e}'\rangle$ between excitons k and k' on rings

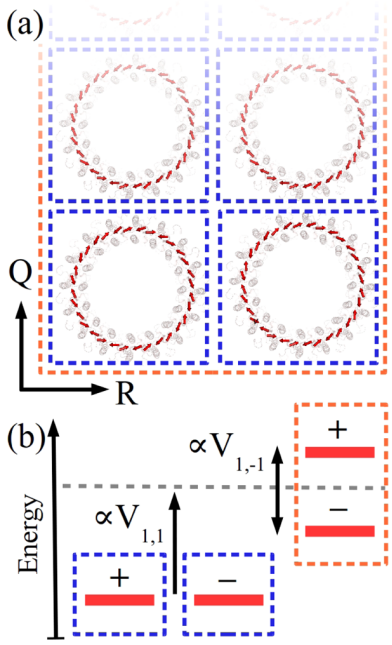

Figure 3. (a) LH complexes in purple bacteria naturally arrange themselves in well-ordered 2D arrays. The spectral consequences of extended delocalization in such an arrangement can be understood by examining a rectangular $Q \times R$ array. The absorption anisotropy is strongest for linear-like arrays ($Q/R \gg 1$), represented schematically by the color gradient. (b) Circular symmetry of single LH complexes concentrates the optical absorption strength in degenerate states with orthogonal polarization (blue bounding boxes). The circular symmetry of the combined system is broken upon interaction (orange bounding boxes), leading to a measurable splitting of polarized states.

DOI: 10.1021/acs.jpca.5b04804
J. Phys. Chem. A XXXX, XXX, XXX−XXX

centered at lattice sites $\vec{e}$ and $\vec{e}'$, calculated by coupling all pigments on both rings according to eq 1, is much smaller than the energy difference between single-ring excitons, namely, $|\langle k, \vec{e}|\mathcal{H}|k, \vec{e}\rangle - \langle k', \vec{e}'|\mathcal{H}|k', \vec{e}'\rangle|$. Such a condition results in a minor mixing between states $|k| \neq |k'|$, and leads to an optical response of assemblies mainly determined by the coupling between the bright $|k = \pm 1, \vec{e}\rangle$ and $|k' = \pm 1, \vec{e}'\rangle$ states from neighboring rings. In particular for this manifold, it can be shown that $V_{1,1} = V_{-1,-1} < 0$, $V_{1,-1} = V^*_{-1,1}$ and the argument $\arg(V_{1,-1}) = \xi$ for $\vec{e} - \vec{e}' = \pm a\hat{x}$ becomes $\arg(V_{1,-1}) = \xi + \pi$ for $\vec{e} - \vec{e}' = \pm a\hat{y}$, where a is the lattice spacing.

In what follows, we consider nearest-neighbor couplings on the rectangular lattice of Figure 3a, as in Figure 2 regarding square and linear configurations, as it exhibits the optical signatures of extended delocalization while allowing simple analytical expressions. In particular, for the LH1 complex of *R. rubrum*, we find $V_{1,1} = -1.8$ cm^{-1} and $|V_{1,-1}| = 4.4$ cm^{-1}. Qualitatively similar results are obtained for couplings beyond nearest-neighbors and triangular lattices, which we consider explicitly in the Supporting Information. Rings are centered at lattice sites $\vec{e} = a(q\hat{x} + r\hat{y})$, where $q = 1, ..., Q \in \mathbb{Z}$, $r = 1, ..., R \in \mathbb{Z}$, and $a = 120$ Å;[3] single-ring excitons are labeled $|\pm 1, q, r\rangle = |\pm 1, \vec{e}\rangle$. Accordingly, the extended excitonic wave functions over the rectangular array read as

$$|\pm, k_q, k_r\rangle = \sqrt{\frac{2 \times 2}{(Q+1)(R+1)}} \times \sum_{q,r} \sin\left(\frac{\pi k_q q}{Q+1}\right) \sin\left(\frac{\pi k_r r}{R+1}\right) |\pm, q, r\rangle \tag{4}$$

where $|\pm\rangle = \frac{1}{\sqrt{2}}(|1\rangle \pm |-1\rangle)$ and $k_q = 1, ..., Q$ and $k_r = 1, ..., R$ are Fourier quantum numbers corresponding to the $\hat{x}$ and $\hat{y}$ directions, respectively. The optical response can be approximated according to eq 3,

$$\begin{pmatrix} |\vec{D}_{+,k_q,k_r}\cdot\hat{E}|^2 \\ |\vec{D}_{-,k_q,k_r}\cdot\hat{E}|^2 \end{pmatrix} \propto \frac{S^2(k_q,Q)}{Q+1}\frac{S^2(k_r,R)}{R+1}\begin{pmatrix} \cos^2\phi \\ \sin^2\phi \end{pmatrix} \tag{5}$$

where ϕ is the angle between the polarization of the field $\hat{E}$ and the axis $\hat{x}$. The absorption strength is determined by

$$S(k,W) = \sin\left(\frac{\pi k}{2}\right)\sin\left(\frac{\pi k W}{2(W+1)}\right)\csc\left(\frac{\pi k}{2(W+1)}\right)$$

distributed over states $|\pm\rangle$ along orthogonal polarizations. Given that $S(k,W) \sim \frac{W}{k}\sin^2\left(\frac{\pi k}{2}\right)$ already for $W \gtrsim 3$–4 rings, the dipole strength becomes small for higher $k > 1$ states, concentrating dipole moment in the k_q, $k_r = 1$ states in the rectangular configuration. The energies of these states are shifted by

$$\begin{aligned} E_\pm &= 2V_{1,1}\left(\cos\left(\frac{\pi}{Q+1}\right) + \cos\left(\frac{\pi}{R+1}\right)\right) \\ &\quad \pm 2|V_{1,-1}|\left(\cos\left(\frac{\pi}{Q+1}\right) - \cos\left(\frac{\pi}{R+1}\right)\right) \\ &= \delta E \pm \Delta E \end{aligned} \tag{6}$$

Given that the absorption is composed of these two shifted optical transitions, a general shift $\delta E = (E_+ + E_-)/2 \propto V_{1,1}$ of the (unpolarized) absorption maximum, with respect to the single-ring case, is expected for the coherently coupled array of rings. Such a shift from the assemblies studied in Figure 2a,b, accounts for $\delta E = 2V_{1,1}$ in the square ($Q = 2$, $R = 2$) and $\delta E = 2V_{1,1}\cos(\pi/5)$ in the linear ($Q = 4$, $R = 1$) assemblies. Hence, the above expression explains why the square geometry shows a greater shift than the linear assembly, with respect to the single-ring case, in the unpolarized absorption spectrum. Last, but not least, note that the magnitude of $V_{1,1}$ depends also on the specific details of the structure (further details in the Supporting Information). Hence, spectral shifts can be used as a tool to understand specific geometrical details that have been not possible to resolve by other means.

The states $|+\rangle$ and $|-\rangle$ are orthogonally polarized; polarization along the $\hat{x}$-axis results in absorption spectra peaking at energy E_+ corresponding to $\vec{D}_+ \propto \hat{x}$, whereas polarization along the $\hat{y}$-axis results in absorption spectra peaking at energy E_- corresponding to the $\vec{D}_- \propto \hat{y}$ state. The subtraction of these two spectra recorded from perpendicular polarizations, the LD, is finite whenever $\delta E = (E_+ - E_-)/2$ does not vanish, which occurs, according to eq 6, strictly due to the resonance coupling $V_{k,k'}$, which breaks the circular symmetry of the assembly. Explicitly, on the basis of eq 6, the effect is greatest for a linear chain ($R = 1$) and a saturation for both the red shift, δE, and splitting, δE, is expected, as $\cos\frac{\pi}{Q+1} \approx 1$ already for $Q \approx 5$–6 rings.

Experimental Determination of Förster Rates. Besides controlling the linear optical response, the resonance coupling dictates the rate at which, on a longer time scale, excitations migrate incoherently between complexes.[38,52] The transfer among different bands that can be resolved spectrally permits experimental schemes that make use of the different spectral components to separate dynamical contributions.[41,53−56] In the case of isoenergetic transfer steps, like LH1 → LH1, this is not possible and it becomes hard to identify the nature of individual dynamical components. Excitation annihilation was used to determine the transfer rate between LH2 rings in *R. sphaeroides*,[57] and techniques based on transient depolarization, such as anisotropy absorption recovery, have been valuable to recognize multiple dynamical contributions at low temperatures in the core complex of *R. rubrum*[58−64] but have failed to unequivocally identify components arising from intraring relaxation or from inter-ring energy transfer. The accurate determination of these rates is crucial for understanding the efficiency of photosynthesis.

We show here that the possibility to obtain the resonance coupling between isoenergetic species of LH1 or LH2 complexes, through the absorption measurements just discussed, circumvents the ambiguity in these isoenergetic landscapes and opens up a promising experimental scheme to quantify their mutual transfer rates.

Two facts of major importance, illustrated in Figure 3, are that the shift of the unpolarized absorption is $\delta E = V_{1,1}\cos(\pi/(Q+1))$ and that the splitting between bright tranitions is $2\delta E = 4|V_{1,-1}|\cos(\pi/(Q+1))$ for linear geometries. Accordingly, measurement of the shift in the unpolarized absorption spectrum determines $V_{1,1}$ whereas, as will be shown shortly, the determination of $V_{1,-1}$ through an LD measurement is possible. A good quantitative agreement between the full calculated spectrum and the subtraction of two Lorentzian line

DOI: 10.1021/acs.jpca.5b04804
J. Phys. Chem. A XXXX, XXX, XXX−XXX

shapes with full width $\Gamma \approx 465\ \mathrm{cm}^{-1}$ (in agreement with experiment) separated by $V_{1,-1}$ permits us to extract the relation

$$\mathrm{LD}_{\max} = C_1 \frac{|V_{1,-1}|}{\Gamma} + O\left(\left(\frac{|V_{1,-1}|}{\Gamma}\right)^3\right) \tag{7}$$

for the LD amplitude, $\mathrm{LD}_{\max}$, with a constant $C_1 = \frac{3\sqrt{3}}{2}$ in the case of two rings, which accounts for the specific choice of Lorentzian line shapes. Accordingly, it is possible to determine through the unpolarized spectrum and the LD amplitude, the values of $V_{1,1}$ and $V_{1,-1}$ independently.

Generalized Förster theory is often used to calculate the rate of incoherent transfer $\gamma_{k\to k'}$ from a donor exciton k to acceptor exciton k'

$$\gamma_{k\to k'} = \frac{2\pi}{\hbar}|V_{k,k'}|^2 Z_k I_{k,k'} \tag{8}$$

where $V_{k,k'}$ is, as before, the coherent excitonic coupling among single-ring states, Z_k is the thermal population (Boltzmann factor), and $I_{k,k'} = \int_0^\infty F_k(\epsilon)\, A_{k'}(\epsilon)\, \mathrm{d}\epsilon$ denotes the spectral overlap integral of the donor fluorescence from exciton k and acceptor absorption of exciton k', F, and A, respectively.[43,65] The total transfer rate from donor to acceptor is $\gamma \approx \sum_{k,k'}\gamma_{k\to k'}$. Although we have taken a large inhomogeneous broadening in our calculations, there is experimental evidence of a predominance of homogeneous broadening of LH1 at room temperature.[43−46] Under the assumption that the emission is also spectrally homogeneous, the total rate is $\gamma \approx \sum_{k,k'}\gamma_{k\to k'}$, and the Förster rate can be calculated as

$$\gamma = \frac{2\pi}{\hbar}(2\,|V_{1,1}|^2 + 2\,|V_{1,-1}|^2) Z_1 I \tag{9}$$

where $I = \int_0^\infty F(\epsilon)\, A(\epsilon)\, \mathrm{d}\epsilon$ is the full spectral overlap and Z_1 is the thermal population of the $|k = \pm 1\rangle$ states, which depends on the single-ring model.

As shown above, $V_{1,1} = -1.8\ \mathrm{cm}^{-1}$ and $|V_{1,-1}| = 4.4\ \mathrm{cm}^{-1}$ are quantified by shifts in absorption and nonzero LD contrast, respectively, which allow a calculation of the Förster rate with a minimum of model input. The dipole moments $|\vec{d}|$ and the dielectric contant $\kappa = 2$ predict an inter-ring transfer time of 8 ps, which is well within the bounds (∼1−20 ps) of estimates from current experiments and theoretical calculations.[31,59,64] Determination of the inter-ring coupling strength by measurement of the LD thus provides a new method to determine Förster transfer rates. This procedure would then provide further insight into the values of the dielectric constant and the BChl dipole moment *in vivo*, which are parameters usually estimated indirectly. Figure 4a plots the transfer time, LD contrast, and absorption shift as a function of these quantities according to eq 9.

Several elements have to be brought together in an experiment that confirms excitonic delocalization across extended domains. A speculative setup is illustrated in Figure 4b on the basis of mutagenesis of blue-shifted LH 1s.[36,51] If a link between LH 1s by means of mechanical bridges or affinity domains is accomplished, the formation of linear-like assemblies will be possible. Additionally, these assemblies must be *macroscopically* aligned to set the polarization excitation directions. The blue-shifted LH 1s will serve then to build the membrane scaffold to accommodate the linear arrays of nonmutated LH 1s and fix their orientations.

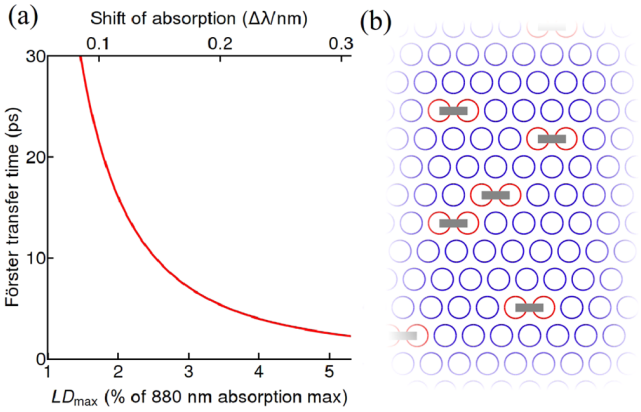

Figure 4. Absorption measurements can provide direct information on the magnitude of transfer rates. In (a) is presented the transfer time between LH1 complexes as a function of the LD contrast and/or shift in the unpolarized absorption (which depend on the resonance coupling $V_{k,k'}$, itself a function of the dielectric constant). An experimental ensemble measurement of the LD signal mitigates the effects of structural disorder and allows a direct absorption readout. Such an experiment is shown in (b), where "blue" rings, mutated to maximally absorb at less than 880 nm,[36,51] are grown in a membrane with "red" rings, absorbing at 880 nm and linked in pairs. The aggregation of blue-shifted LH 1s leads to their vanishing LD, whereas, if the axes of the red pairs align, their nonzero LD signal can be measured.

Fluorescence yield detection upon polarized excitation performed on single assemblies[33] is also a promising technique to confirm/disregard the hypothesis of long-range excitonic delocalization in natural LH aggregates.

CONCLUSIONS

In summary, we have modeled and characterized, through analytical expressions and numerical calculations, the optical response due to resonance coupling between multiple rings in photosynthetic membranes of purple bacteria. This investigation highlights the importance of a description, at room temperature, of light absorption beyond the standard assumption of excitons restricted to individual rings. The dipole moment redistribution that emerges in 2D arrays of LH1 rings, due to extended excitons, leads us to propose an experimental procedure, based on polarized and unpolarized absorption spectra of small linear-like arrays of rings, which quantifies inter-ring resonance coupling. We show that this experimental procedure allows an alternative, indirect measurement of their incoherent Förster transfer rate, which carries additional information on currently poorly characterized parameters, like the dielectric constant or the *in vivo* BChls dipole moment. Such a measurement could be accomplished through absorption of an ensemble of oriented linear-like assemblies or through fluorescence yield detection of single assemblies which have been excited by polarized fields.

ASSOCIATED CONTENT

Supporting Information

The Supporting Information is available free of charge on the ACS Publications website at DOI: 10.1021/acs.jpca.5b04804.

Study of the effects of inhomogeneous broadening on measures of exciton delocalization and a generalization of the results to alternate membrane geometries (PDF)

DOI: 10.1021/acs.jpca.5b04804
J. Phys. Chem. A XXXX, XXX, XXX−XXX

AUTHOR INFORMATION

Corresponding Author

*M. B. Plenio. E-mail: martin.plenio@uni-ulm.de.

Author Contributions

¶These authors contributed equally

Notes

The authors declare no competing financial interest.

ACKNOWLEDGMENTS

This work was funded by the EU STREP projects PAPETS and QUCHIP, the ERC Synergy grant BioQ and an Alexander von Humboldt Professorship. Additional support was provided by the National Science Foundation through PFC@JQI and the National Science Foundation Graduate Research Fellowship Program under DGE-1322106. Any opinions, findings, and conclusions and recommendations expressed in this material are those of the authors and do not necessarily reflect the views of the National Science Foundation. The authors would like to thank R. Ghosh (University of Stuttgart), F. Jelezko (University of Ulm) and Shai Machnes (Weizmann Institute, Israel) for discussion at early stages of this work, and R. Ghosh for experimental data and a careful and critical reading of the manuscript.

REFERENCES

(1) Visschers, R. W.; Chang, M. C.; van Mourik, F.; Parkes-Loach, P. S.; Heller, B. A.; Loach, P. A.; van Grondelle, R. Fluorescence Polarization and Low-Temperature Absorption Spectroscopy of a Subunit Form of Light-Harvesting Complex I from Purple Photosynthetic Bacteria. *Biochemistry* **1991**, *30*, 5734−5742.

(2) Karrasch, S.; Bullough, P. A.; Ghosh, R. The 8.5 Å Projection Map of the Light Harvesting Complex I from *Rhodospirillum rubrum* Reveals a Ring Composed of 16 Subunits. *EMBO J.* **1995**, *14*, 631.

(3) Bahatyrova, S.; Freese, R. N.; Siebert, C. A.; Olsen, J. D.; van der Werf, K. A.; van Grondelle, R.; Niederman, R. A.; Bullough, O. A.; Otto, C.; Hunter, N. C. The Native Architecture of a Photosynthetic Membrane. *Nature* **2004**, *430*, 1058.

(4) Scheuring, S.; Goncalves, R. P.; Prima, V.; Sturgis, J. The Photosynthetic Apparatus of *Rhodopseudomnas palustris:* Structure and Organization. *J. Mol. Biol.* **2006**, *358*, 83.

(5) Shreve, A. P.; Trautman, J. K.; Franck, H. A.; Owens, T. G.; Albrecht, A. C. Femtosecond Energy-transfer Processes in the B800-B850 Light-Harvesting Complex of Rhodobacter sphaeroides 2.4.1. *Biochim. Biophys. Acta, Bioenerg.* **1991**, *1058*, 280−288.

(6) Siebert, C. A.; Qian, P.; Fotiadis, D.; Engel, A.; Hunter, N. C.; Bullough, P. A. Molecular Architecture of Photosynthetic Membranes in *Rhodobacter sphaeroides*: the Role of PufX. *EMBO J.* **2004**, *23*, 690.

(7) Hu, X.; Ritz, T.; Damjanović, A.; Authennrieth, F.; Schulten, K. Photosynthetic apparatus of purple bacteria. *Q. Rev. Biophys.* **2002**, *35*, 1−62.

(8) Strumpfer, J.; Schulten, K. Excited State Dynamics in Photosynthetic Reaction Center and Light Harvesting Complex 1. *J. Chem. Phys.* **2012**, *137*, 065101.

(9) Cheng, R. C.; Silbey, R. J. Coherence in the B800 Ring of Purple Bacteria LH2. *Phys. Rev. Lett.* **2006**, *96*, 028103−028106.

(10) Strümpfer, J.; Séner, M.; Schulten, K. How Quantum Coherence Assists Photosynthetic Light-Harvesting. *J. Phys. Chem. Lett.* **2012**, *3*, 536−542.

(11) Romero, E.; Augulis, R.; Novoderezhkin, V. I.; Ferreti, M.; Thieme, J.; Zigmantas, E.; van Grondelle, R. Quantum Coherence in Photosynthesis for Efficient Solar-Energy Conversion. *Nat. Phys.* **2014**, *10*, 676−682.

(12) Fuller, F.; Pan, J.; Gelzinis, A.; Butkus, V.; Seckin Senlik, S.; Wilcox, D. E.; Yocum, C.; Valkunas, L.; Abramavicius, D.; Ogilvie, J. P. Vibronic Coherence in Oxygenic Photosynthesis. *Nat. Chem.* **2014**, *6*, 706−711.

(13) Lee, H.; Cheng, Y. C.; Flemming, G. R. Coherence Dynamics in Photosynthesis: Protein Protection of Excitonic Coherence. *Science* **2007**, *316*, 1462−1465.

(14) Panitchayangkoon, G.; Hayes, D.; Fransted, K. A.; Caram, J. R.; Harel, E.; Wen, J.; Blankenship, R.; Engel, G. S. Long-lived Quantum Coherence in Photosynthetic Complexes at Physiological Temperature. *Proc. Natl. Acad. Sci. U. S. A.* **2010**, *107*, 12766−12770.

(15) Engel, G. S.; Calhoun, T.; Read, E.; Ahn, T.; Mancal, T.; Cheng, Y.; Blankenship, R.; Fleming, G. R. Evidence for Wavelike Energy Transfer through Quantum Coherence in Photosynthetic Systems. *Nature* **2007**, *446*, 782−786.

(16) Brixner, T.; Stenger, J.; Vaswani, H. M.; Cho, M.; Blankenship, R. E.; Fleming, R. G. Two-dimensional Spectroscopy of Electronic Couplings in Photosynthesis. *Nature* **2005**, *434*, 625−628.

(17) Hayes, D.; Panitchayangkoon, G.; Fransted, K. A.; Caram, J. R.; Wen, J.; Freed, K. F.; Engel, G. S. Dynamics of Electronic Dephasing in the Fenna-Matthews-Olson Complex. *New J. Phys.* **2010**, *12*, 065042.

(18) Mohseni, M.; Rebentrost, P.; Lloyd, S.; Aspuru-Guzik, A. Environment-assisted Quantum Walks in Photosynthetic Energy Transfer. *J. Chem. Phys.* **2008**, *129*, 174106.

(19) Plenio, M. B.; Huelga, S. F. Dephasing-assisted Transport: Quantum Networks and Biomolecules. *New J. Phys.* **2008**, *10*, 113019.

(20) Olaya-Castro, A.; Lee, C.; Olsen, F.; Johnson, N. Efficiency of Energy Transfer in a Light-Harvesting System under Quantum Coherence. *Phys. Rev. B: Condens. Matter Mater. Phys.* **2008**, *78*, 085115.

(21) Autenrieth, F. The Photosynthetic Apparatus of *Rhodospirillum rubrum*: a Computational Approach. *Diploma Thesis*, University of Stuttgart, 2002.

(22) Adolphs, J.; Renger, T. How Proteins Trigger Excitation Energy Transfer in the FMO Complex of Green Sulfur Bacteria. *Biophys. J.* **2006**, *91*, 2778−2797.

(23) Strumpfer, J.; Schulten, K. Light Harvesting Complex II B850 Excitation Dynamics. *J. Chem. Phys.* **2009**, *131*, 225101.

(24) Timpmann, K.; Trinkunas, G.; Qian, P.; Hunter, C.; Freiberg, A. Excitons in Core LH1 Antenna Complexes of Photosynthetic Bacteria: Evidence for Strong Resonant Coupling and Off-diagonal Disorder. *Chem. Phys. Lett.* **2005**, *414*, 359−363.

(25) Trinkunas, G.; Freiberg, A. A Disordered Polaron Model for Polarized Fluorescence Excitation Spectra of LH1 and LH2 Bacteriochlorophyll Antenna Aggregates. *J. Lumin.* **2006**, *119−120*, 105−110.

(26) Caycedo-Soler, F.; Schroeder, C. A.; Autenrieth, C.; Ghosh, R.; Huelga, S. F.; Plenio, M. B. *Quantum Delocalization Directs Antenna Absorption to Photosynthetic Reaction Centres.* **2015**, submitted for publication.

(27) Scheuring, S.; Busselez, J.; Levy, D. Structure of the dimeric PufX-containing core complex of *Rhodobacter sphaeroides*. *J. Biol. Chem.* **2005**, *279*, 3620.

(28) Scheuring, S.; Sturgis, J. N.; Prima, V.; Bernadac, D.; Levi, D.; Rigaud, J. L. Watching the Photosynthetic Apparatus in Native Membranes. *Proc. Natl. Acad. Sci. U. S. A.* **2004**, *101*, 11293.

(29) Walz, T.; Ghosh, R. Two-dimensional Crystallization of the Light-Harvesting I Reaction Centre Photounit from *Rhodospirillum rubrum*. *J. Mol. Biol.* **1997**, *265*, 107−111.

(30) Caycedo-Soler, F.; Rodríguez, F. J.; Quiroga, L.; Johnson, N. F. Light-harvesting Mechanism of Bacteria Exploits a Critical Interplay between the Dynamics of Transport and Trapping. *Phys. Rev. Lett.* **2010**, *104*, 15832.

(31) Ritz, T.; Park, S.; Schulten, K. Kinetics of Excitation Migration and Trapping in the Photosynthetic Unit of Purple Bacteria. *J. Phys. Chem. B* **2001**, *105*, 8259−8267.

(32) Niwa, S.; Yu, L. J.; Takeda, K.; Hirano, Y.; Kawakami, T.; Wang-Otomo, Z. Y.; Miki, T. Structure of the LH1−RC complex from Thermochromatium tepidum at 3.0 Å. *Nature* **2014**, *508*, 228−232.

(33) Gerken, U.; Lupo, D.; Tietz, C.; Wrachtrup, J.; Ghosh, R. Circular Symmetry of the Light-harvesting 1 Complex from

DOI: 10.1021/acs.jpca.5b04804
J. Phys. Chem. A XXXX, XXX, XXX−XXX

Rhodospirillum rubrum is not Perturbed by Interaction with the Reaction Center. *Biochemistry* **2003**, *42*, 10354−10360.
(34) Cogdell, R. J.; Gall, A.; Köhler, J. The Architecture and Function of the Light-harvesting Apparatus of Purple Bacteria: from Single Molecules to *in vivo* Membranes. *Q. Rev. Biophys.* **2006**, *39*, 227−324.
(35) Stahlberg, H.; Dubochet, J.; Vogel, H.; Ghosh, R. Are the Light-harvesting I Complexes from *Rhodospirillum rubrum* Arranged Around the Reaction Centre in a Square Geometry? *J. Mol. Biol.* **1998**, *282*, 819−831.
(36) Ghosh, R.; Hauser, H.; Bachofen, R. Reversible Dissociation of the B873 Light-harvesting Complex from *Rhodospirillum rubrum* G9+. *Biochemistry* **1988**, *27*, 1004−1014.
(37) van Amerongen, H.; Valkunas, L.; van Grondelle, R. *Photosynthetic Excitons*; World Scientific Publishing Co. Pte. Ltd.: Singapore, 2000.
(38) Förster, T. In *Delocalized Excitation and Excitation Transfer*; Beyerle, M.-M., Ed.; Academic Press: New York, 1965; pp 93−137.
(39) Tannor, D. J. *Introduction to Quantum Mechanics: a Time-Dependent Perspective*; University Science Books: Sausolito, CA, 2006.
(40) Harel, E.; Engel, G. S. Quantum Coherence Spectroscopy Reveals Complex Dynamics in Bacterial Light-harvesting Complex 2 (LH2). *Proc. Natl. Acad. Sci. U. S. A.* **2012**, *109*, 706−711.
(41) Hildner, R.; Brinks, D.; Nieder, J. B.; Cogdell, R. J.; Van Hulst, N. F. Quantum Coherent Energy Transfer over Varying Pathways in Single Light-Harvesting Complexes. *Science* **2013**, *340*, 1448−1451.
(42) Monshouwer, R.; Abrahamsson, M.; van Mourik, F.; van Grondelle, R. Superradiance and Exciton Delocalization in Bacterial Photosynthetic Light-harvesting Systems. *J. Phys. Chem. B* **1997**, *101*, 7241−7248.
(43) Scholes, G. D. Long-range Resonance Energy Transfer in Molecular Systems. *Annu. Rev. Phys. Chem.* **2003**, *54*, 57−87.
(44) Freiberg, A.; Timpmann, K. Picosecond Fluorescence Spectroscopy of Light-harvesting Antenna Complexes from Rhodospirillum rubrum in the 300−4 K Temperature Range. Comparison with the Data on Chromatophores. *J. Photochem. Photobiol., B* **1992**, *15*, 151−158.
(45) Kramer, H.; Pennoyer, J.; van Grondelle, R.; Westerhuis, W.; Niedermann, R.; Amesz, J. Low-temperature Optical Properties and Pigment Organization of the B875 Light-harvesting Bacteriochlorophyll-protein Complex of Purple Photosynthetic Bacteria. *Biochim. Biophys. Acta, Bioenerg.* **1984**, *767*, 335−344.
(46) Rijgersberg, C.; van Grondelle, R.; Amesz, J. Energy transfer and Bacteriochlorophyll Fluorescence in Purple Bacteria at Low Temperature. *Biochim. Biophys. Acta, Bioenerg.* **1980**, *592*, 53−64.
(47) Thouless, D. J. Electrons in Disordered Systems and the Theory of Localization. *Phys. Rep.* **1974**, *13*, 93−142.
(48) Dahlbom, M.; Pullerits, T.; Mukamel, S.; Sundström, V. Exciton Delocalization in the B850 Light-Harvesting Complex: Comparison of Different Measures. *J. Phys. Chem. B* **2001**, *105*, 5515−5524.
(49) Davydov, A. The Theory of Molecular Excitons. *Usp. Fiz. Nauk* **1964**, *82*, 393−448.
(50) Wu, H.-M.; Ratsep, M.; Lee, I.-J.; Cogdell, R.; Small, G. Exciton Level Structure and Energy Disorder of the B850 Ring of the LH2 Antenna Complex. *J. Phys. Chem. B* **1997**, *101*, 7654−7663.
(51) Olsen, J. D.; Sturgis, J.; Westerhuis, W. H. J.; Fowler, G. J. S.; Hunter, C. N.; Robert, B. Site-directed Modifications of the Ligands to the Bacteriochlorophylls of the Light-harvesting LH1 and LH2 Complexes of Rhodobacter sphaeroides. *Biochemistry* **1997**, *36*, 12625−12632.
(52) Pullerits, T.; Sundström, V. Photosynthetic Light-Harvesting Pigment-Protein Complexes: Toward Understanding How and Why. *Acc. Chem. Res.* **1996**, *29*, 381−389.
(53) Fidler, A.; Singh, V.; Long, P.; Dahlberg, P.; Engel, G. Probing Energy Transfer Events in the Light-harvesting Complex 2 (LH2) of *Rhodobacter sphaeroides* with Two-dimensional Spectroscopy. *J. Chem. Phys.* **2013**, *139*, 155101.
(54) Dahlberg, P.; Fidler, A.; Caram, J.; Long, P.; Engel, G. Energy Transfer Observed in Live Cells using Two-dimensional Electronic Spectroscopy. *J. Phys. Chem. Lett.* **2013**, *4*, 3636−3640.
(55) Brüggermann, B.; Christensson, N.; Pullerits, T. Temperature Dependent Exciton-exciton Annihilation in the LH2 Antenna Complex. *Chem. Phys.* **2009**, *357*, 140−143.
(56) Hess, S.; Cachisvilis, M.; Timpmann, K. E.; Jones, M.; Fowler, G.; Hunter, N. C.; Sundstrom, V. Temporally and Spectrally Resolved Subpicosecond Energy Transfer within the Peripheral Antenna Complex (LH2) and from LH2 to the Core Antenna Complex in Photosynthetic Purple Bacteria. *Proc. Natl. Acad. Sci. U. S. A.* **1995**, *92*, 12333.
(57) Schubert, A.; Stenstam, A.; Beenken, W. J. D.; Herek, J. L.; Cogdell, R.; Pullerits, T.; Sundström, V. In Vitro Self-Assembly of the Light Harvesting Pigment-Protein LH2 Revealed by Ultrafast Spectroscopy and Electron Microscopy. *Biophys. J.* **2004**, *86*, 2363−2373.
(58) Hunter, N.; Bergström, H.; van Grondelle, R.; Sundström, V. Energy-transfer Dynamics in Three Light-harvesting Mutants of *Rhodobacter sphaeroides*: a Picosecond Spectroscopy Study. *Biochemistry* **1990**, *29*, 3203−3207.
(59) Sundström, V.; van Grondelle, R.; Bergström, H.; Åkesson, E.; Gillbro, T. Excitation-energy Transport in the Bacteriochlorophyll Antenna Systems of *Rhodospirillum rubrum* and *Rhodobacter sphaeroides*, Studied by Low-intensity Picosecond Absorption Spectroscopy. *Biochim. Biophys. Acta, Bioenerg.* **1986**, *851*, 431−446.
(60) Bergström, H.; Westerhuis, W.; Sundström, V.; van Grondelle, R.; Niederman, R.; Gillbro, T. Energy Transfer within the Isolated B875 Light-harvesting Pigment-protein Complex of Rhodobacter sphaeroides at 77 K Studied by Picosecond Absorption Spectroscopy. *FEBS Lett.* **1988**, *233*, 12−16.
(61) Pullerits, T.; Visscher, K.; Hess, S.; Sundström, V.; Freiberg, A.; Timpmann, K.; van Grondelle, R. Energy transfer in the Inhomogeneously Broadened Core Antenna of Purple Bacteria: A Simultaneous Fit of Low-intensity Picosecond Absorption and Fluorescence Kinetics. *Biophys. J.* **1994**, *66*, 236−248.
(62) Bradforth, S.; Jimenez, R.; van Mourik, F.; van Grondelle, R.; Fleming, G. Excitation Transfer in the Core Light-harvesting Complex (LH-1) of *Rhodobacter sphaeroides*: An Ultrafast Fluorescence Depolarization and Annihilation Study. *J. Phys. Chem.* **1995**, *99*, 16179−16191.
(63) Bergström, H.; Sundström, V.; van Grondelle, R.; Gillbro, T.; Cogdell, R. Energy Transfer Dynamics of Isolated B800-B850 and B800-B820 Pigment-protein Complexes of *Rhodobacter sphaeroides and Rhodopseudomonas acidophila*. *Biochim. Biophys. Acta, Bioenerg.* **1988**, *936*, 90−98.
(64) Sundström, V.; van Grondelle, R. *Anoxygenic Photosynthetic Bacteria*; Springer: Berlin, 1995; pp 349−372.
(65) Jang, S.; Newton, M.; Silbey, R. Multichromophoric Förster Resonance Energy Transfer. *Phys. Rev. Lett.* **2004**, *92*, 218301.

DOI: 10.1021/acs.jpca.5b04804
J. Phys. Chem. A XXXX, XXX, XXX−XXX

Supporting Information: "Optical signatures of quantum delocalization over extended domains in photosynthetic membranes"

Christopher A. Schroeder[1,2,*], Felipe Caycedo-Soler[1,*], Susana F. Huelga [1], and Martin B. Plenio[1]
[*] *These authors contributed equally.*
[1] *Institute of Theoretical Physics, University of Ulm, Albert-Einstein-Allee 11 D - 89069 Ulm, Germany and*
[2] *Joint Quantum Institute, Department of Physics, University of Maryland and National Institute of Standards and Technology, College Park, MD 20742, USA*

I. HAMILTONIAN OF LH1 COMPLEX

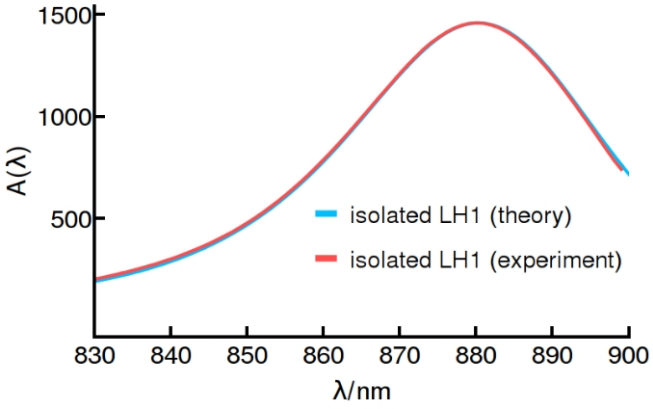

FIG. 1. The Hamiltonian and noise parameters taken in this study reproduce the experimentally-observed absorption spectrum.

In this study we have employed a model of the *R. rubrum* LH1 where 32 BChl molecules, bound to 16 α and β polypeptides as $\alpha\beta(\mathrm{BChl})_2$ subunits, are equidistantly arranged along a ring of radius $r = 47$ Å. Dipole moments are taken to be tangential to, and in the plane of, the ring. The sub-nanometer distance between neighbouring chromophores implies that the nearest-neighbour couplings depend on the geometry of the electronic wave-function of each chromophore and cannot be inferred directly from a dipolar interaction in the point-dipole approximation. Couplings on the ring can be fitted using fluorescence anisotropy measurements, resulting in nearest-neighbor couplings $Q_1 = 600$ cm^{-1} and $Q_2 = 377$ cm^{-1} for the intra- and inter-dimer couplings, respectively[1]. As discussed in the text, homogeneous broadening is taken into account using either a Lindbladian master equation with a pure dephasing rate of $\gamma_d = 106$ cm^{-1} or the equivalent protocol of dressing excitonic stick-spectra with a Lorentzian of full-width half-maximum $2 \times \gamma_d$. These parameters reproduce the experimentally-measured absorption spectrum of isolated LH1, see Fig.1. Coupling between dipoles on different rings, separated by $a = 120$ Å, is calculated using the dipole-dipole interaction

$$J_{n,m} = \frac{1}{4\pi\kappa}\left(\frac{\vec{d}_m\cdot\vec{d}_n}{|\Delta\vec{r}_{n,m}|^3} - \frac{3\left(\vec{d}_n\cdot\Delta\vec{r}_{n,m}\right)\left(\vec{d}_m\cdot\Delta\vec{r}_{n,m}\right)}{|\Delta\vec{r}_{n,m}|^5}\right), \tag{1}$$

where $\Delta\vec{r}_{n,m} = \vec{r}_n - \vec{r}_m$ and κ=2 is the relative permittivity. The LH1 dipoles are taken to be of magnitude $\sqrt{2.4}\times 6.3$ D $= 9.8$ D to take into account the observed hyperchromism[2].

II. MEASURES OF EXTENDED DELOCALIZATION

Excitonic properties from purple bacteria membranes can be obtained from the Coulomb exchange Hamiltonian

$$H = \sum_{m}^{2NR}(\epsilon_m + \delta_{\epsilon_m})\,|m\rangle\langle m| + \sum_{m\neq n}^{2NR} J_{mn}(|n\rangle\langle m| + |m\rangle\langle n|) \tag{2}$$

where J_{nm} denotes the interaction strength between the induced transition-dipoles of pigments n and m, corresponding to electronic excited states $|n\rangle$ and $|m\rangle$ with energies ϵ_n and ϵ_m. Note that each ring contains $2N = 32$ pigments and we examine a line of rings (Q=1), as in the main text. The wavefuntions take a remarkable simple form in the absence of protein inhomogeneities ($\delta_{\epsilon_m} = 0$), as given in eq (5) of the main text.

Explicitly, the bright states of relevance for the optical response are

$$|\pm, k_x = k_y = 1, Q = 1\rangle \propto \sum_r \sin\left(\frac{\pi}{R+1}\right)|\pm, r\rangle\,. \tag{3}$$

These states present populations in each ring proportional to $\sin^2(\pi r/(R+1))$ which is largest for the rings lying in the middle of the linear chain. Note that in the abscence of coherent interaction among rings, all states should have populations concentrated in single rings. As a consequence, on average, a density operator will present a statistical mixture with populations being equally shared among all rings.

Absorption is a linear functional in the density operator. Hence, we concentrate on the density operator

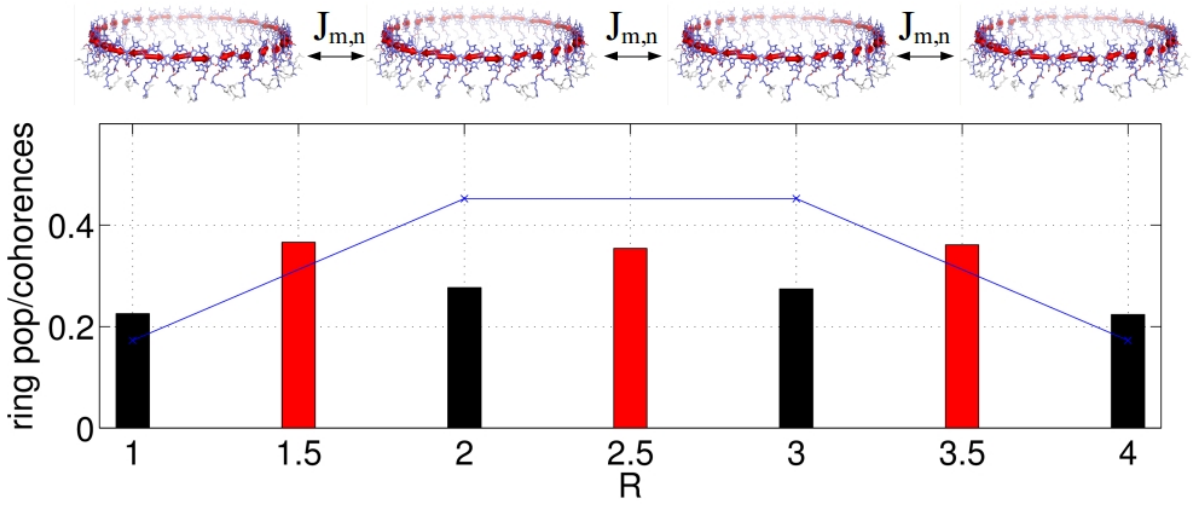

FIG. 2. The linear array of rings in top presents ring populations $\sum_{n\epsilon r} |\langle n|\rho|n\rangle|$ and total inter-ring coherences $\sum_{n\epsilon r_1, m\epsilon r_2} |\langle n|\rho|m\rangle|$ shown in black and red bars, as a result from averages of 50000 stochastic realisations of inhomogeneous noise. The result of the the noise-less model for populations is presented in blue connected crosses.

$\rho = \overline{|\alpha\rangle\langle\alpha|}$ which results from averaging the eigenstates of eq (2) under realistic conditions, i.e. with appropriate magnitude for protein-induced fluctuations $\sqrt{\langle\delta_\epsilon^2\rangle} = 325$ cm^{-1}. Our choice of magnitude of these fluctuations is justified by a detailed analysis of absorption spectra of LH1 in *R. rubrum*, see Fig. 1.

The average population of each ring for the subset of states $|\alpha\rangle$ with the largest light-induced dipole strength, is presented in Figure 2. Here, a non-uniform population in the linear configuration of rings can be seen, where the complexes in the middle of the chain present a greater population compared to the rings at the chain edges. The pattern of ring populations displayed in the presence of inhomogeneities resembles the noiseless case from states $|\pm, k_x = k_y = 1, Q = 1\rangle$, which illustrates the formation of excitons fulfilling the full array boundary conditions in the presence of quasi-static fluctuations. The resilience of the excitons to the inhomogeneous disorder illustrates that the disorder produce noticable smearing out of excitonic delocalization, but does not completely erase its features. Another indicator of excitonic coherence among neighbouring rings is also presented in Figure 2, namely the total coherence $\rho_{r_1,r_2} = \sum_{n\epsilon r_1, m\epsilon r_2} |\langle n|\rho|m\rangle|$ among all chromophores that belong to *neighbouring* rings r_1 and r_2. This total inter-ring coherence, ussually assumed to be negligible for inter-ring exciton transfer, is manifestly non-zero in Figure 2, and is the cause for the absorption anisotropy that produces the finite linear dichroism (LD) discussed in the main text.

To characterise the excitons formed upon photon absorption, useful quantities are the conventional inverse participation ratio

$$IPR_C \equiv \left(\sum_i^{2NR} |c_i^\alpha|^4\right)^{-1} \tag{4}$$

and a generalisation which we denote the ring inverse participation ratio

$$IPR_R \equiv \left(\sum_{r=1}^{R}\left(\sum_{i\epsilon r}^{N} |c_i^\alpha|^2\right)^2\right)^{-1} \tag{5}$$

where the inner and outer sums are performed over BChls that belong to a specific ring r and over all rings in the array, respectively.

As defined, IPR_C ranges from 1 to the total number of pigments in the array and measures how many chromophores participate in a given exciton, while IPR_R ranges from 1 for any exciton confined to a single ring, to $IPR_R = R$ for pure states that are evenly delocalised over the entire array of R rings. For $IPR_R > 1$ or $IPR_C > 32$, these two quantitites demonstrate unambiguously the presence of bright excitons over domains greater than a single ring (see Figure 3(a)). A general trend shows larger exciton lengths for arrays with higher number of rings. Figure 3(a) highlights realisations extending over more than 2 rings ($IPR_R > 2$), which extend well beyond the current paradigm of single ring excitons (lying flat with $IPR_R = 1$), sufficient for the description of processes with a longer built-in timescale.

The dependence of excitons length with the size of the array is made conspicuous in Figure 3(b) where the average $\overline{IPR}_R$ is shown as a function of the linear ($Q = 1$) array size for the two brightest states $|\alpha\rangle$ of each realisation. Here, it can be appreciated an increase in exciton size with the array extension in the same qualitative manner as the homogeneous wavefunctions of eq (3) (also shown in the same figure).

Based on the observations that the wavefunction and the excitonic length from averages of inhomogeneous noise resemble qualitatively the features that arise from a noiseless treatment, it can be safely assumed that the

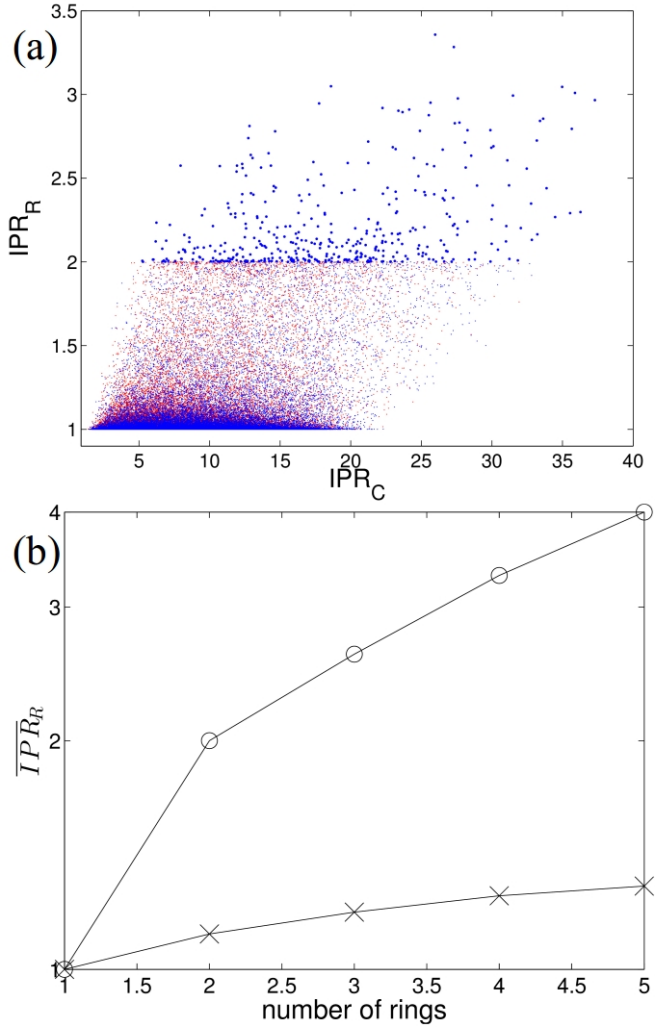

FIG. 3. (a) Scatter plot (points) of the IPR_C and IPR_R from eqs.(4,5) for two (red) and five (blue) rings, for states with the greatest dipole moment in realisations of the quasi-static fluctuations in eq 2. States that delocalize beyond 2 rings are highlighted. In (b) is presented the average $\overline{IPR}_R$ for the brightest state in each noise realisation (crosses) and for the noiseless wavefunction in eq (3) (circles), as a function of the length of the array. Symbols connected by straight lines to guide the eye.

inhomogeneous broadening is included, the noiseless features are not completely smeared out. It becomes natural therefore, to assert the properties of the system based on the noiseless characterization presented through equations (5)-(7) in the main text.

III. SHIFT OF THE UNPOLARISED ABSORPTION SPECTRUM: DEPENDENCE OF $V_{1,1}$ ON THE GEOMETRY OF THE RING DIPOLES

The resonant interaction between rings in general assemblies can result in a shift of the absorption spectra,

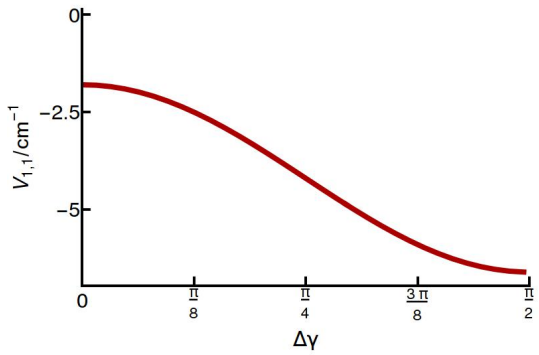

FIG. 4. Coupling $V_{1,1}$ as a function of the angle $\Delta\gamma$ between the Q_y transition dipole and the ring tangent.

addressed by equation 6 in the main text and numerically supported by Figure 2(b) and 2(d) in the main text. The magnitude of this shift, in comparison to the isolated ring situation, depends on the structural details of the rings. As it has been stated in section I of this SI, we have used a structure where the Q_y transition dipoles are tangent to the circumference of the ring. However if this angle, $\Delta\gamma$, is increased, the magnitude of $V_{1,1}$ increases, as presented in Figure 4. Accordingly, the determination of the shift in the spectra reflects specific details of the rings, which escape measures performed on single rings, but are otherwise accessible through the observation of assemblies.

IV. INHOMOGENEOUS BROADENING.

The spectral lineshape and width are determined by both homogeneous and inhomogeneous contributions. Two effects are manifested when inhomogeneities are introduced in excitonic transitions, namely, lineshape modifications and energy shifts. Figure 5 (a) shows that overlapping spectra are obtained with different combinations of homogeneous and inhomogneous broadening, being the most conspicuous signature of their slightly different lineshapes, the difference in the low energy tails. For the case of smaller inhomogeneous broadening, a Lorentzian-like lineshape appears with slower rise as compared to the result with higher inhomogeneity with a Gaussian-like lineshape. For values of inhomogeneous disorder bounded by the full spectral width, the energy splitting between absorption spectra along orthogonal polarizations is greater with the inhomogeneous noise Figure 5 (b). This phenomenon can be understood by the excitonic repulsion which results in slightly larger splittings for greater levels of noise[3]. Accordingly, the LD changes due to the inhomogeneous noise (see inset of Figure 5 (b)), with a very counter-intuitive result, namely, greater inhomogenities produce greater LD amplitude. Such increase can only be traced back with full numerical simulations, as it

requires to account for all the dark levels in order to quantitatively assert the shift calculated in the inset of Figure 5 (b). Note however that within the inhomogenities expected in these systems, the energy difference among orthogonal absorption spectra does not produce dramatic changes in the LD, given that we have been careful to reproduce in all cases the absorption profile shown in Figure 5 (a). The major change in the LD will be due to the full broadening of the optical transition transition – labeled in Figure 5 (a) as Γ– as it becomes conspicuous by comparison of the LD from homogeneously broadened spectra with a width of 2×106 cm^{-1} in Figure 1 of the main text, and the LD of full spectrum, here presented. In the former case, the amplitude of the LD can reach about 5% of the absorption spectrum, while in the latter case the LD amplitude is reduced quite generally to $2-3\%$, as Figure 5 (b) illustrates. It can be concluded from this analysis, that the LD changes only slightly depending on the inhomogeneous component in the spectra with a robustness only vulnerable to the total width Γ of the absorption spectrum.

The noise model presented above accounts for environmentally-induced inhomogeneities in the pigment energies. However, it does not account for explicit perturbations of the chromatophore vesicle, such as variations in the inter-complex distance or for structural perturbations, such as elliptical deformations of the rings.

Examination of paracrystalline[4] domains of LH2 in *Rsp. photometricum* and close-packed orthorhombic crystals[5,6] in *R. rubrum* imply variations of only a few Angstroms in the center-to-center distances among neighbouring ring structures[4,7]. Figure 5(c) shows the effect on the LD when the inter-complex distance suffers stochastic variations which are much greater than the variations observed from pair correlation functions calculated from atomic force microscopy (AFM) experiments ($\sqrt{\langle \delta r^2 \rangle} = 0, 5, 10, 15$ Å as compared to $\sqrt{\langle \delta r^2 \rangle} \sim 1$ Å observed in[4]). This figure illustrates that the contrast in the LD actually increases with greater center-to-center distance variations. This surprising result can be understood from the functional form of the Coulomb interaction. At a center-to-center distance of a few tens of nanomenters, the Coulomb interaction scales as $1/r^3$ which means that bringing rings together by δr increases the coupling more than it is decreased by separating them by δr, hence, the LD is enhanced in average. A further signature is apparent for large variations reflected by the red shift of the LD. This signature can be traced back to the amplitude of absoprtion along $\hat{x}$ and $\hat{y}$ axes, which for strong variation of the center-to-center distance makes the former absorption greater than the latter, and hence produces a LD which is slightly asymmetric. Note, however, that the few Angstrom variations observed in experiments are too small to appreciably affect the LD signal by its magnitude or to enhance appreciably the absorption along one of the polarization direction with respect to the orthogonal, by means of inter-ring distance inhomogeneities.

In general, LH complexes in purple bacteria express geometries which may differ from the circular ring of *R. rubrum* in our model. Another conformation of the LH1 in *R. rubrum* has been observed to be significantly ellipsoidal[6]. In addition, the LH2 of *Rubrivax gelatinosus*, obtained by AFM[8], and the latest LH1 X-ray structure of *Tch. tepidum* both exhibit a degree of ellipticity[9]. It is not known if the long axes of elliptical rings may be aligned or randomly oriented along the membranes where they are synthesized. A study of elliptical structures is therefore in order as it might clarify the scope of the LD to witness extended delocalization.

Oval structures with an apparently small eccentricity $\sqrt{1-\left(\frac{a}{b}\right)^2} = 0.32$, where a and b are the minor and major axes, respectively, produce energy shifts among $k=\pm1$ states of $\simeq 100$ cm^{-1} in a single ring[10], which is 10 times larger than the shifts due to inter-ring excitonic coupling, presented in the inset of Fig. 5 (b). In these experiments the excitation polarisation was fixed with respect to the major axis of the single elliptical ring. In an ensemble, there is no reason to believe that the orientations of major axes will or will not correlate. In order to isolate the effect from elliptical deformation, we momentarily set the pigment energy inhomogeneities to zero. Now, if an ensemble presents randomly-oriented major axes and the rings do not couple coherently, then the finite LD signals, stemming from the elliptical geometries, cancel out and lead to a vanishing LD (see Fig. 5 (d)). In order to account for the elliptical deformations we use an interaction between nearest neighbours with a functional form that only depends on their relative distance $J_{n,m} = \frac{\Delta r_0^3}{\Delta r_{n,m}^3} Q_{1,2}$ where $r_0 \approx 9.2\mathring{A}$ is the distance among pigments in the circular geometry, and $Q_{1,2}$ are the nearest-neighbour couplings. In the same fashion, if an ensemble of randomly-oriented coupled rings is considered, then the LD arising from the elliptical perturbation vanishes and only the nonzero signal arising from the coherent interaction remains. Figure 4(e) shows that the nonzero LD for coherently-coupled linear arrays is robust to the ensemble-averaged elliptical perturbation, as it results in a maximum value of 5 % for two rings, which, as expected, is similar to the value, with just homogeneous noise, presented in Fig. 1 of the main text.

It was observed that the macromolecular assembly in purple bacteria vesicles can indeed present long-range organisation[11]. Therefore, the likelihood of having affinity domains in each ring that set specific connecting residues to neighbouring units and result in an overall specific orientation of all major axes, is not out of the question. If the macromolecular assembly has a preferred orientation of rings-ellipse axes, a finite LD will be measured even in the absence of appreciable inter-ring excitonic delocalization.

In general, if the geometrical contribution to the LD is independent of the size of the assembly, then a simple subtraction among LD signals, ΔLD, arising from different assemblies lengths will therefore represent the

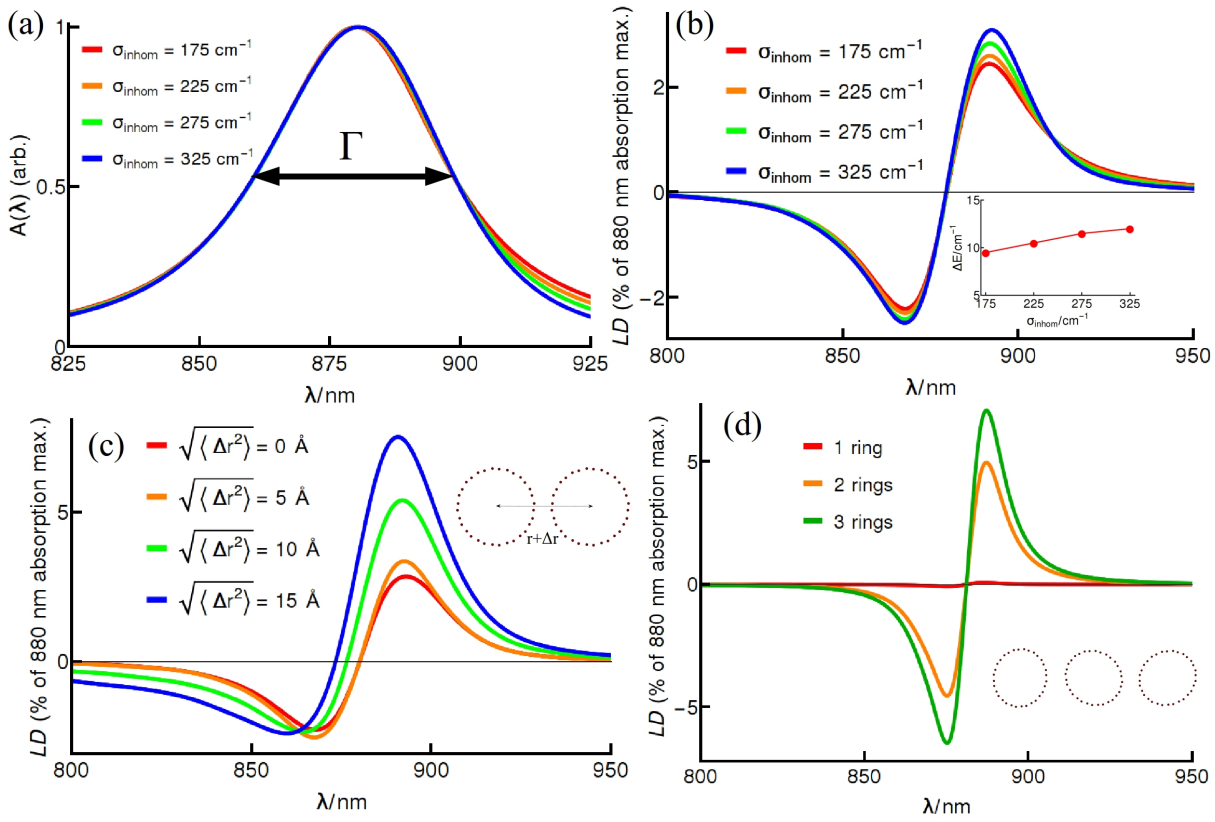

FIG. 5. Effects of energetic and structural disorder on LD. In (a), the overall absorption spectra takes on more Gaussian lineshape, manifested from steeper tails of the spectra as inhomogeneous disorder is increased. The splitting between orthogonally-polarized manifolds, ΔE, in (inset b), has only a slight increase with inhomogeneous noise, which results in an LD signal (b) robust to energetic disorder (σ_{inhom} = 175 - 325 cm^{-1}). The LD is also robust to variations of the inter-ring distance, as shown in (c). In (d) the LD ensemble averaged over randomly-oriented oval structures in linear arrays with 1, 2 and 3 rings.

residual contribution resulting from the extended excitonic delocalisation among such assemblies.

V. GENERAL 2D GEOMETRIES

The description in the main text of excitonic delocalisation over extended domains made use of square unit-cell lattices. It was concluded that arrays with a large aspect ratio and small width are desirable in order to obtain an polarized optical response which encodes the symmetries of the extended excitons. Here we generalise these statements to arrays with other unit cells. Specifically, we analyse a triangular lattice and, to prove the generality of our statemements, we also study a square unit cell with non-nearest-neighbour interactions.

The possibility to use the natural assembly of these complexes to probe inter-ring excitonic delocalization is investigated by numerical diagonalization of the Hamiltonian in the manifold $|k|, |k'| = 1$ for a triangular unit-cell lattice (Figure 6). The triangular unit cell approximates the natural "quasi-hexagonal" aggregation state observed for LH1 complexes in photosynthetic membranes of *R. rubrum*[12]. Triangular para-crystaline domains of LH2 complexes also form in *Rsp. photometricum* at low light intensity conditions[13]. Figure 6(a), shows that the dipole strength in the triangular lattice is concentrated at the band edges, analogous to the prediction made by eqs (3-5) in the main text. As shown in this figure, states polarized along and perpendicular to the long-axis of the array are split in energy, leading to a finite LD once the stick spectra is dressed with appropriate line-shape functions. Figure 6(b) highlights another important feature. Here, even though an asymmetric array is being considered with the same aspect ratio, the LD signal is, in fact, smaller ($LD_{max} \approx 0.6$ % in (b) as opposed to $LD_{max} \approx 0.7$ % in (a)). This can be understood from eq (7) in the main text, which shows that the energy splitting between bright states decreases for arrays of the same aspect ratio but increasing size. Hence, independent of unit-cell configurations, only arrays with a width of a few rings will be suitable to probe extended excitonic delocalization through LD.

The same conclusion can be drawn based on a square unit-cell with non-diagonal interactions, as shown in Figure 7. The additional interactions produce addi-

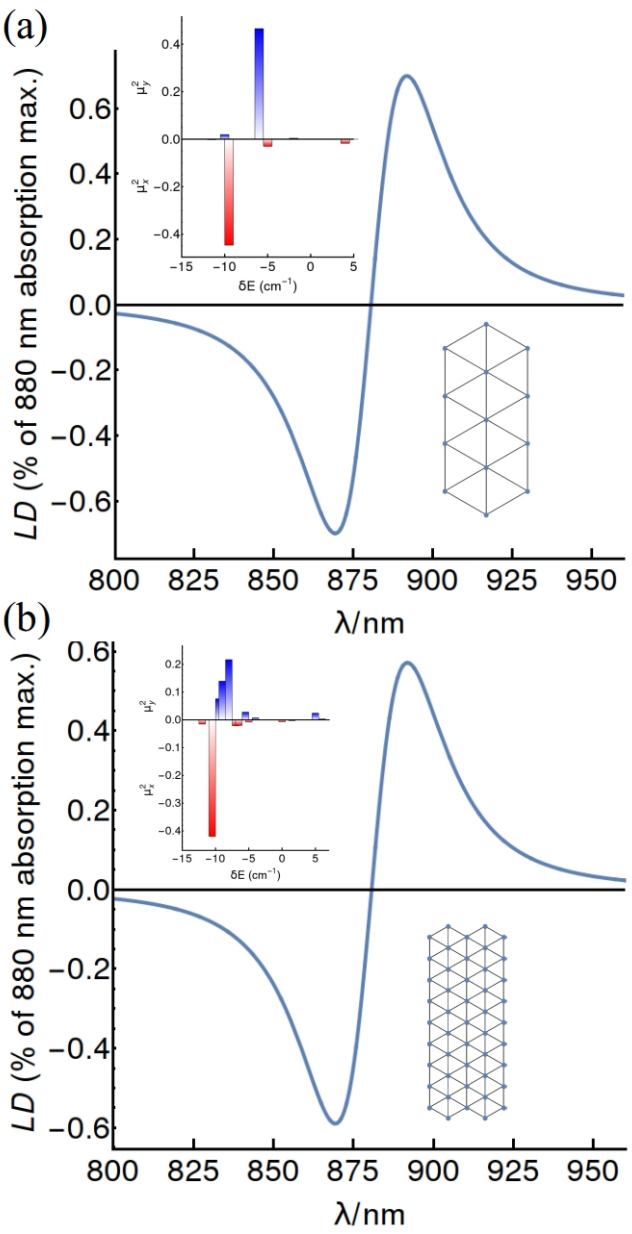

FIG. 6. *LD* spectra for the triangular lattice configuration and increasing array size. Insets show the lattice configuration studied and stick polarized spectra. A small asymmetric array, as in (a), exhibits a larger *LD* than its double (b) due to a decreased splitting of polarized states. This can be qualitatively understood from the results for the square unit-cell, eq (7) of the main text.

tional splittings, and arrays with appreciable aspect ratio ($Q/R \gg 1$ or $Q/R \ll 1$) still present a dipole moment redistribution that leads to polarization anisotropy. If the array is symmetric, the polarized states are not split in energy and the array shows zero *LD*, which can be seen from eq (7) in the main text. These results show that, independent of the unit-cell geometry, it is possible to witness *LD* in general arrays of small width and appreciable aspect ratio.

[1] K. Timpmann, G. Trinkunas, P. Qian, C. Hunter, and A. Freiberg, "Excitons in Core LH1 Antenna Complexes of Photosynthetic Bacteria: Evidence for Strong Resonant Coupling and Off-diagonal Disorder," Chemical Physics Letters **414**, 359–363 (2005).

[2] R. Ghosh, H. Hauser, and R. Bachofen, "Reversible Dissociation of the B873 Light-harvesting Complex from *Rhodospirillum rubrum* G9+," Biochemistry **27**, 1004–1014 (1988).

[3] S. Jang and R. Silbey, "Theory of Single Molecule Line Shapes of Multichromophoric Macromolecules," J. Chem. Phys **118**, 9312–9323 (2003).

[4] S. Scheuring and J. Sturgis, "Chromatic Adaptation of Purple Bacteria," Science **309**, 484 (2005).

[5] R. Ghosh, J. Kessi, H. Hause, E. Wherli, and R. Bachofen, *Molecular Biology of Membrane-bound Complexes in Phototrophic Bacteria*, edited by G. Drews and E. A. Dawes (Plenum Press, New York, 1990) pp. 245–251.

[6] S. J. Jamieson, P. Wang, P. Qian, J. Y. Kirkland, M. J. Conroy, C. N. Hunter, and P. Bullough, "Projection Structure of the Photosynthetic Reaction Centre-antenna Complex of *Rhodospirillum rubrum* at 8.5 Å Resolution." EMBO J. **21**, 3927–3935 (2002).

[7] S. Scheuring, J. L. Rigaud, and J. N. Sturgis, "Variable LH2 Stoichiometry and Core Clustering in Native Membranes of *Rhodospirillum photometricum*," EMBO **23**, 4127 (2004).

[8] S. Scheuring, F. Reiss-Husson, A. Engel, J.-L. Rigaud, and J.-L. Ranck, "High-resolution AFM Topography of *Rubrivax gelatinosus* Light-harvesting Complex LH2," EMBO J. **20**, 3029–3035 (2001).

[9] S. Satomi Niwa, L. J. Yu, K. Takeda, Y. Hirano, T. Kawakami, Z. Y. Wang-Otomo, and T. Miki, "Structure of the LH1-RC Complex from *Thermochromatium tepidum* at 3.0 Å," Nature **508**, 228 (2014).

[10] U. Gerken, F. Jelezko, B. Götze, M. Branschädel, C. Tietz, R. Ghosh, and J. . Wrachtrup, "Membrane Environment Reduces the Accessible Conformational Space Available to an Integral Membrane Protein," J. Phys. Chem. B **107**, 338–343 (2003).

[11] R. N. Freese, C. A. Siebert, R. A. Niederman, N. C. Hunter, C. Otto, and R. van Grondelle, "The Long-range Organization of a Native Photosynthetic Membrane," PNAS **101**, 17994–17999 (2004).

[12] S. Karrasch, P. A. Bullough, and R. Ghosh, "The 8.5 Å Projection Map of the Light Harvesting Complex I from *Rhodospirillum rubrum* Reveals a Ring Composed of 16 Subunits," EMBO Journal **14**, 631 (1995).

[13] S. Scheuring, R. P. Goncalves, V. Prima, and J. Sturgis, "The Photosynthetic Apparatus of *Rhodopseudomnas palustris:* Structure and Organization," Journal of Molecular Biology **358**, 83 (2006).

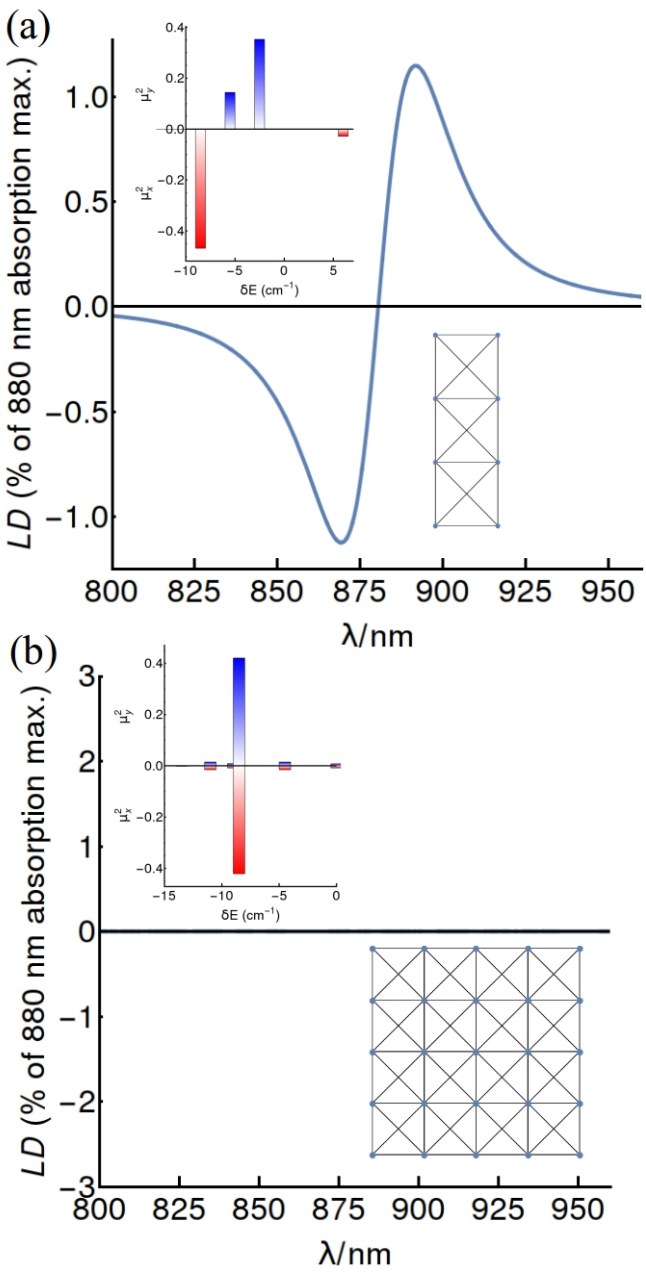

FIG. 7. *LD* spectra for the square lattice configuration and non-nearest-neighbor interactions. Insets show the lattice configuration studied and stick polarized specta. The strip of dimers in (a) reflects the native organization of LH1s in membranes containing LH1 and LH2, and exhibits a non-zero *LD*. Symmetric arrays ($Q = R$), as in (b), show zero *LD* since the polarized states are degenerate in energy. These results are qualitatively similar to those for the square unit-cell with nearest-neighbor interactions, eq (7) of the main text.

Chapter 5: Quantum Delocalization Directs Antenna Absorption to Photosynthetic Reaction Centers

Previous work has recognized electronic coherence within tightly-packed light-harvesting (LH) units or within individual reaction centers (RCs) as an important ingredient for a complete understanding of excitation energy transfer dynamics. However, the electronic coherence across RC *and* LH units has been consistently neglected as it does not play a significant role during these relatively slow transfer processes. This chapter examines the absorption process, which has a much shorter built-in timescale. We demonstrate that the - often overlooked - spatially extended but short-lived excitonic delocalization across RC *and* LH units plays a relevant role in general photosynthetic systems, as it causes a redistribution of direct absorption towards the charge separation unit. Using the complete core complex of *Rhodospirillum rubrum*, we verify experimentally a 90 % increase in the direct optical absorption of the RC *in situ* as compared to isolated RCs. Numerical calculations reveal that similar enhancements can be expected for a wide variety of photosynthetic units in both plant and bacterial systems, suggesting that this mechanism is conserved across species and providing a clear new design principle for artificial light-harvesting nanostructures.

5.1 The Role of Excitonic Couplings

Excitonic dynamics between tightly-packed pigments, such as within the RC *or* within the LH units, has been recognized to be of considerable importance for characterizing their individual optical responses and for determining the associated time-scales for excitation energy transfer steps [50, 58–62]. It is natural then to ask what role excitonic couplings *between* RC and LH units play in the primary processes, and on what timescale they survive. Long-lasting oscillatory signals measured in these systems [3–8] have driven a wave of theoretical work that has successfully explained the experimental observations [9–12], broadened our understanding of the role of the vibrational environment [2, 13–18, 20] and hint that coherences may exist on surprising length- and timescales. These studies have provided input for useful refinements of models for excitonic energy transfer and confirmed that, even when assuming the electronic coherence between RC and LH units to survive hundreds of femtoseconds, its effect on energy transfer processes between LH and RC, which take place on time scales of tens of picoseconds, is minor [20]. As a consequence, quantum mechanical excitonic delocalization across RC and LH units has so far been consistently ignored. However, we will show that for processes that have a built-in timescale shorter than energy transfer, such as absorption, excitonic delocalisation among RC and LH pigments may become relevant. These principles are illustrated in Fig. 5.1 (A).

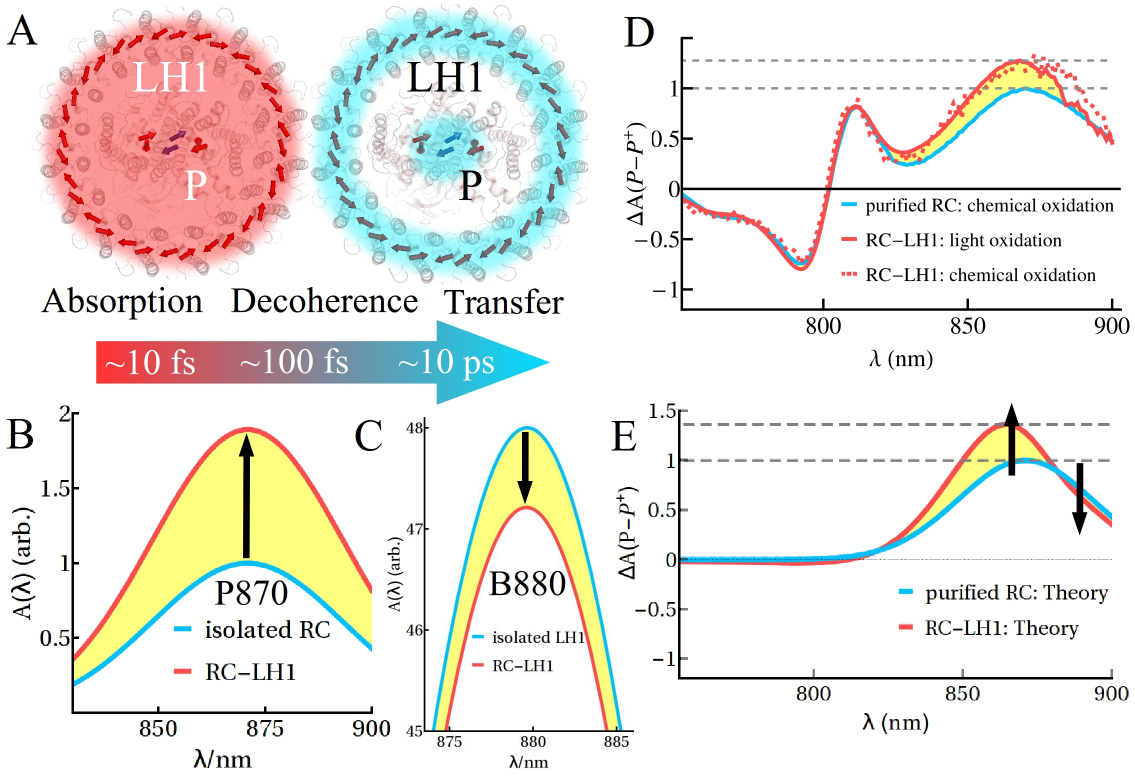

Figure 5.1: (A) Schematic representation of the *R. rubrum* RC-LH1 bacteriochlorophyll (BChl) pigments. After $\sim$ 100 fs, environment-induced dephasing will degrade the quantum mechanical delocalization between the antenna *and* the RC (red shading), and transforms the state into a statistical mixture of populations residing *either* on the antenna *or* the RC (blue shading). The subsequent EET can be accurately described by incoherent classical hopping [20]. It is known that excitonic couplings are crucial in an accurate description of the absorption of the P870 band of the purified RC (B) and the B880 band of the purified LH1 (C) of *R. rubrum*. The dark-minus-light spectrum of the complete core complex (D) witnesses spectral shifts and redistribution of absorption intensity due to excitonic coupling between RC and LH1, as explained in the main text. The experimental observation can be reproduced (E) by increasing the absorption intensity of the P870 band by 90 %, illustrated by the area (yellow) between the spectra for the core complex and for purified RC, with a concomitant decrease of the B880 band.

5.2 Redistribution of Absorption in the RC-LH1 Core Complex

Excitonic couplings are known to cause spectral shifts and redistribute intensity in the observable corresponding to the absorption process, namely the ab-

sorption spectrum [63]. Our model RC-LH1 system for exploring excitonic coupling between RC and LH pigments is the core complex of the purple bacterium *R. rubrum* [64]. This organism is a fresh-water bacterium found in shallow, turbid ponds under conditions of low-light intensity and low oxygen tension. The core complex possesses a photosynthetic RC, containing a "special pair" (P) of bacteriochlorophyll (BChl) molecules which mediate the primary process of light-induced charge separation, surrounded by an LH1 complex containing 32 BChls arranged in a protein with ring-like geometry around the RC (Fig. 5.1 (A)). The absorption spectrum $A(\lambda)$ of the P pigments peaks around 870 nm, whereas the LH1 exhibits a single absorption band at 880 nm, denoted the P870 band and B880 band, respectively (Fig. 5.1 (B)-(C)). The single LH1 band arises due to the coherent interactions between the 32 BChls, arranged on a ring with the Q_y transition dipoles lying almost tangential to it.

Tracing spectral changes in the core complex due to coherent interactions between RC and LH1 is complicated experimentally by the fact that the P870 absorption spectrum overlaps with the much stronger optical response of the LH1 B880 band, as discussed in Ch. 2. We make use of the oxidation of the P-pigments, $P \rightarrow P^+$, upon excitation, as they donate an electron to the charge separation process. Upon oxidation the $P870$ resonance shifts to 1260 nm, far into the infrared region, and therefore effectively suppresses the resonant coherent interaction between P and LH1 pigments [65]. Subtracting core complex spectra of oxidized P^+ from those of neutral P filters out the overwhelming B880 component and highlights the changes in the absorbing bands due to the coherent interaction. We carried out

two independent procedures for the oxidation reaction, $P \rightarrow P^{+}$, namely, optical excitation or stoichiometric addition– in the dark– of the oxidising agent potassium ferricyanide. With both procedures we observed difference spectra from core complexes and purified RCs (Fig. 5.1 (D)) which are consistent with a 90 % increase in P870 absorption in the former over the latter (Fig. 5.1 (B)-(C), (E)). Further experimental details are given in Appendix 8.

5.3 Theory: Analytical Results.

In this section we show that the key experimental result, a redistribution of absorption intensity from the B880 band to the P870 band, can be understood by a simple model with two effective excited states $|P870\rangle$ and $|B880\rangle$– and associated dipole moments $\vec{D}_{P870}$ and $\vec{D}_{B880}$– which are split in energy by ΔE, coherently coupled with strength V through the Coulomb exchange interaction between their transition dipoles. As we will show in the next section, the effects of local dephasing, which models homogeneous broadening, is reproduced by a simple dressing of stick spectra, meaning the fully-delocalized states must be used to understand absorption according to $A(\lambda) \propto |\vec{D}_{\lambda}|^2$. The coherent nature of the coupling is manifested in two measurable optical signatures: spectral shifts and absorption intensity redistributions, which, as shown below, scale as $(V/\Delta E)^2$ and $V/\Delta E$, respectively, to lowest order. Hence, in the core complex, where coupling among RC and LH1 satisfies $V \ll \Delta E$, excitonic coupling may lead to a measurable absorption intensity redistribution while leaving spectral positions almost unaffected due to the quadratic

dependence on $(V/\Delta E)$.

Excitonic properties of membranes subject to low-intensity illumination can be obtained from the electronic Hamiltonian in the single excitation subspace

$$\mathscr{H} = \sum_i \epsilon_i \left|i\right\rangle \left\langle i\right| + \sum_{i,j} C_{i,j} \left|i\right\rangle \left\langle j\right| = \sum_\alpha \omega_\alpha \left|\alpha\right\rangle \left\langle \alpha\right| \tag{5.1}$$

where ϵ_i is the excitation energy of pigment i and $C_{i,j}$ is the coupling, through the Coulomb exchange mechanism, between the Q_y induced transition dipoles, $\vec{d_i}$, of the electronic excited-states $|i\rangle$ and $|j\rangle$ on pigments n and m [63]. The sub-nanometer distance between neighbouring P-pigments and neighboring ring pigments implies that the nearest-neighbour couplings depend on the geometry of the electronic wave-function of each chromophore and cannot be inferred directly from a dipolar interaction in the point-dipole approximation. Couplings on the ring can be fitted using fluorescence anisotropy measurements, resulting in nearest-neighbor couplings $Q_1 = 600$ cm^{-1} and $Q_2 = 377$ cm^{-1} for the intra- and inter-dimer couplings, respectively [66]. The coupling between P-pigments is taken to be $V_P = 400$ cm^{-1} [58]. Finally, coupling between LH1 and P-pigments is calculated using the dipole-dipole interaction

$$C_{i,j} = J\left(\hat{d}_i^{LH1} \cdot \hat{d}_i^P - 3(\hat{d}_i^{LH1} \cdot \Delta\hat{r}_{i,j})(\hat{d}_j^P \cdot \Delta\hat{r}_{i,j})\right) \tag{5.2}$$

$$= J(-1)^{i+j} \sin\left(\frac{2\pi}{M} i\right) \tag{5.3}$$

where $\Delta\hat{r}_{i,j} = \vec{r}_i^{LH1} - \vec{r}_j^P$, $\kappa = 2$ is the relative permittivity, $d^{RC} = 6.3$ D and d^{LH1}

$= \sqrt{2.4} \times 6.3$ D $= 9.8$ D to take into account the observed hyperchromism [47], and J $= \frac{5042}{\kappa} \frac{d^{LH1} d^P}{R^3} = 1.5$ cm^{-1} with R $= 47$ Å. Diagonalization of Eq. 5.1 leads to delocalized wavefunctions (excitons) $|\alpha\rangle = \sum_i c_i^\alpha |i\rangle$ and associated excitonic dipole moments $\vec{D}_\alpha = \sum_i c_i^\alpha \vec{d}_i$.

The exciton states of circular aggregates are well-known (see Ref. [51] and Ch. 3), and modeling the LH1 complex with a C_{16} symmetry allows simple analytical expressions for spectral observables. Due to the periodic symmetry of the LH1, its Hamiltonian, from Eq. 5.1, is best examined in the Fourier basis. Considering degenerate dimers and taking into account only the nearest-neighbour couplings Q_1 and Q_2, this leads to wave-functions

$$|k, \nu\rangle = \frac{1}{\sqrt{M/2}} \sum_{m=1}^{M} e^{i \frac{4\pi}{M} k \lceil \frac{m}{2} \rceil} U(k)_{\nu, m \,(mod 2)+1} |m\rangle \tag{5.4}$$

$$U(k) = \begin{pmatrix} e^{i\Phi(k)/2} \cos\Theta(k) & -e^{-i\Phi(k)/2} \sin\Theta(k) \\ e^{i\Phi(k)/2} \sin\Theta(k) & e^{-i\Phi(k)/2} \cos\Theta(k), \end{pmatrix} \tag{5.5}$$

where $M = 32$, $k \in \{-M/4+1, \ldots, M/4\}$, $\lceil \frac{m}{2} \rceil$ is the smallest integer greater than $m/2$, $\Theta(k) = \frac{\pi}{4}$ and $\Phi(k) = \arctan \frac{Q_2 \sin \frac{4\pi}{M} k}{Q_1 + Q_2 \cos \frac{4\pi}{M} k}$. These angles reflect the "amount of dimerization": $\Phi(k)$ captures the difference between intra- and inter-dimer coupling (Q_1 and Q_2), and $\Theta(k)$ captures the site energy differences (here taken to be zero).

These exciton wavefunctions leading to dipole moments $\vec{D}_{k,\nu}$ and energies

$E(k,\nu)$

$$\vec{D}_{k,1} = \delta_{k,\pm1} d^{LH1} \sqrt{M/2} \cos\left(\frac{\Phi(1) - {}^{2\pi}/_{32}}{2}\right) \begin{pmatrix} \mp{}^{i}/_{\sqrt{2}} \\ {}^{1}/_{\sqrt{2}} \end{pmatrix}$$

$$\approx \delta_{k,\pm1} d^{LH1} \sqrt{M/2} \begin{pmatrix} \mp{}^{i}/_{\sqrt{2}} \\ {}^{1}/_{\sqrt{2}} \end{pmatrix} \tag{5.6}$$

$$\vec{D}_{k,2} = \delta_{k,\pm1} d^{LH1} \sqrt{M/2} \sin\left(\frac{\Phi(1) - {}^{2\pi}/_{32}}{2}\right) \begin{pmatrix} {}^{1}/_{\sqrt{2}} \\ \pm{}^{i}/_{\sqrt{2}} \end{pmatrix}$$

$$\approx 0 \tag{5.7}$$

$$E(k,\nu) = \epsilon + (-1)^{\nu} \left(Q_1 + Q_2 \cos\left(\frac{4\pi}{M} k\right)\right), \tag{5.8}$$

The circular symmetry is manifest in the two-fold degeneracy $E_{k,\nu} = E_{-k,\nu}$ and the dipole selection rule $\vec{D}_{k,\nu} \propto \delta_{k,\pm1}$, and the dimerisation in the splitting by $2(Q_1 - Q_2)$ of the energies into two bands, denoted by ν.

The concentration of dipole strength in the upper and lower bands is a function of $\Phi(1) - {}^{2\pi}/_{32} \approx 0$, which reflects the amount of dimerisation. As $Q_1 \to Q_2$, $\Phi(1) \to {}^{2\pi}/_{M}$ and, consequently, more dipole strength is concentrated in the lower band. For the LH1, more than 99% of the total absorbing strength is in the low-lying $|k = \pm1, 1\rangle$, which is responsible for the strong response of the LH1 at $E(\pm1, 1) \equiv$ 880 nm. Since the optical properties are determined by the bright state $|k = \pm1, 1\rangle$, we consider only the lower manifold and drop the index ν in what follows.

The bright $P870$ band corresponds to absorption by the anti-symmetric superposition state $|P870\rangle$ since the dipole moments of the P-pigments are anti-parallel.

Its coherent coupling to the ring excitons is, using Eq. 5.2 and Eq. 5.6,

$$V_k \equiv \langle P870| \mathscr{H} |k,1\rangle = \delta_{k,\pm 1} (\mp i) \frac{\sqrt{MN}}{2} J. \tag{5.9}$$

This expressions illustrate a selection rule, $V_k \propto \delta_{k,\pm 1}$, for the coupling between P-pigment and LH1 excitons. Since $|P870\rangle$ only couples to $|k = \pm 1, 1\rangle$, we need only three levels in order to characterize RC-LH1 interactions. The reduced Hamiltonian is

$$\mathscr{H} = \begin{pmatrix} \Delta E & V_1 & V_{-1} \\ V_1^* & 0 & 0 \\ V_{-1}^* & 0 & 0 \end{pmatrix}. \tag{5.10}$$

where $\Delta E \equiv 130$ cm^{-1} is the energy difference between the bright 870 nm and 880 bands, and $V_1 = 6$ cm^{-1} using Eq. 5.9. This three-level system can be reduced to an effective two-level system by choosing a suitable basis for the degenerate $k = \pm 1$ subspace. This basis is found to be

$$|B880\rangle = \frac{1}{\sqrt{2}} \left(e^{-i\psi} |k = 1\rangle + e^{i\psi} |k = -1\rangle \right), \tag{5.11}$$

$$|\emptyset\rangle = \frac{1}{\sqrt{2}} \left(e^{-i\psi} |k = 1\rangle - e^{i\psi} |k = -1\rangle \right) \tag{5.12}$$

where $\psi = \arg(V_1)$. Note that $|\vec{D}_{B880}|^2 = M/2$. In that basis the Hamiltonian

becomes

$$\mathscr{H} = \begin{pmatrix} \Delta E & V & 0 \\ V & 0 & 0 \\ 0 & 0 & 0 \end{pmatrix}, \tag{5.13}$$

where $V = \sqrt{2}|V_1| = \sqrt{MN/2}J = 8.5\ \mathrm{cm}^{-1} \ll \Delta E$. The effective two-level Hamiltonian in Eq. 5.39 illustrates all the features of extended delocalization in the RC-LH1 system. Diagonalization of Eq. 5.39 leads to delocalized eigenstates and shifted energies

$$\left|P870'\right\rangle = \cos\theta\,|P870\rangle + \sin\theta\,|B880\rangle\,, \tag{5.14}$$

$$\left|B880'\right\rangle = -\sin\theta\,|P870\rangle + \cos\theta\,|B880\rangle\,, \tag{5.15}$$

$$\theta = \frac{1}{2}\arctan\left(\frac{2V}{\Delta E}\right) \tag{5.16}$$

$$E_{P870'} = \frac{\Delta E}{2}\left(1 + \sqrt{1 + \frac{4V^2}{\Delta E^2}}\right) \approx \Delta E\left(1 + \left(\frac{V}{\Delta E}\right)^2\right) \tag{5.17}$$

$$E_{P880'} = \frac{\Delta E}{2}\left(1 - \sqrt{1 + \frac{4V^2}{\Delta E^2}}\right) \approx -\Delta E\left(\frac{V}{\Delta E}\right)^2 \tag{5.18}$$

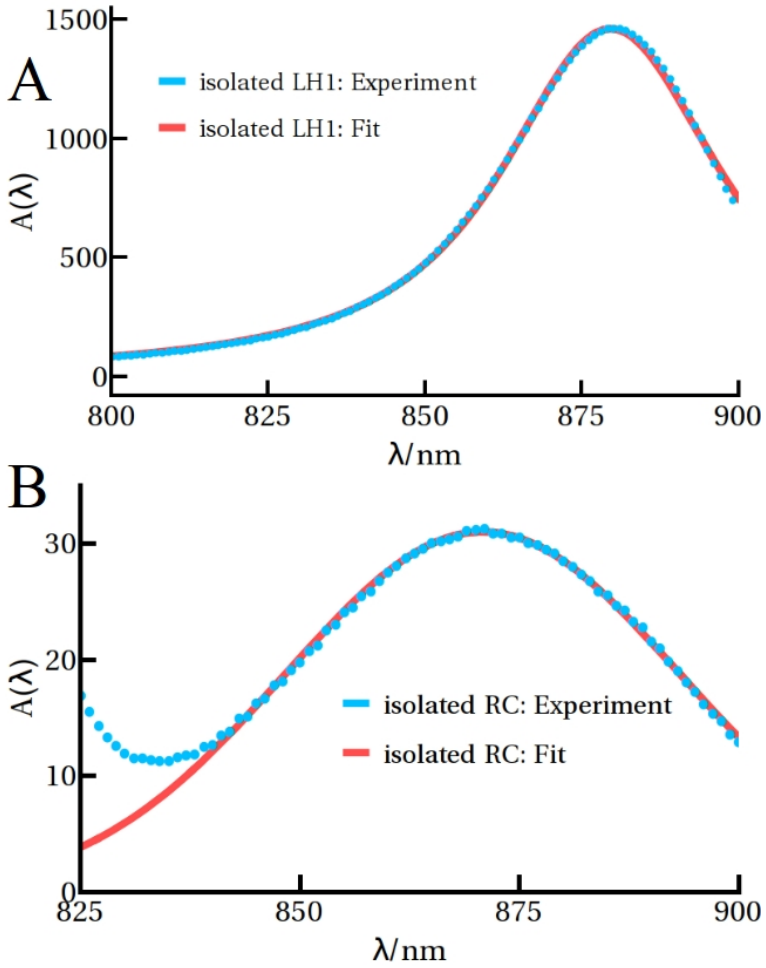

Figure 5.2: The absorption lineshape of the isolated LH1 (**A**) can be well-fit by a Voigt function, which is a convolution of a Lorentzian $L(x,\gamma)$ and a Gaussian $G(x,\sigma)$ according to $V(x,c,\sigma,\gamma,a^{LH1}) = a^{LH1}\int_{\infty}^{\infty} G(x',\sigma)L(x-c-x',\gamma)dx'$. Best-fit parameters a^{LH1} = 93161 (arb.), c = 879.6 nm, σ = 5 nm and γ = 19 nm lead to average error of less than 1 %. The P870 band (**B**) is well-fit by a simple Gaussian $G(x,c,\sigma,a^P) = a^P/\sqrt{2\pi\sigma^2}exp(-(x-c)^2/(2\sigma^2))$. Best-fit parameters a^P = 1743 (arb.), c = 870.8 nm and σ = 22.4 nm lead to average error of less than 1 %. According to Eq. 5.23, the absorption intensity redistributed is, in these arbitrary but absolute units, $\delta a = 1557$.

Hence, the $P870$ band energy does not shift to first-order in $^{V}/_{\Delta E} \ll 1$, ac-

cording to Eq. 5.17, but has a modified dipole strength

$$|\vec{D}'_{P870}|^2 = |\cos\theta\,\vec{D}_{P870} + \sin\theta\,\vec{D}_{B880}|^2 \tag{5.19}$$

$$\approx |\vec{D}_{P870}|^2 + 2\Re\left\{\vec{D}^*_{P870}\cdot\vec{D}_{B880}\right\}\left(\frac{V}{\Delta E}\right) \tag{5.20}$$

$$= N\,(d^P)^2 + \frac{MN}{\sqrt{2}}\frac{J}{\Delta E}d^P d^{LH1}. \tag{5.21}$$

Equation 5.21 shows that the $P870$ band increases its absorption intensity since $\Delta E > 0$. Hence, the uphill energy landscape, $\Delta E > 0$, which sets transfer-to-trap as the bottleneck in the core complex, increases direct absorption in the $P870$ band. An equivalent expression can be obtained for the case that the angle between the Q_y dipole moments and the ring tangent, $\Delta\gamma$, is not zero

$$|\vec{D}'_{P870}|^2 \approx N\,(d^P)^2 + \frac{MN}{\sqrt{2}}\frac{J}{\Delta E}d^P d^{LH1}(1 - 3\sin^2\Delta\gamma), \tag{5.22}$$

and shows that the tangential orientation, $\Delta\gamma = 0$, maximizes dipole redistribution to the RC. Finally, note that, in accordance with the dipole sum rule, the B880 band strength

$$|\vec{D}'_{B880}|^2 = |\cos\theta\,\vec{D}_{B880} - \sin\theta\,\vec{D}_{P870}|^2 \tag{5.23}$$

decreases by an amount such that the total absorption intensity $|\vec{D}'_{B880}|^2 + |\vec{D}'_{P870}|^2 + |\vec{D}_{\emptyset}|^2 = M\,(d^{LH1})^2 + N\,(d^P)^2$ remains constant.

Remarkably, these analytic results give quantitative agreement with experi-

mental measurement of the absorption redistribution, as shown in Fig. 5.1 (D)-(E). In short, we fit Gaussian and Voigt functions to the isolated RC and isolated LH1 spectra, respectively, to capture the lineshape and use Eqs. 5.19 and 5.23 to predict how the absorption intensity is redistributed according to

$$A(\omega) = \sum_{\alpha} |\vec{D}'_{\alpha}|^2 f_{\alpha}(\omega - \omega_{\alpha}) \tag{5.24}$$

where f_α is the spectral lineshape of the isolated constituent. The absorption intensity– that is, the integrated area of the absorption band– is redistributed according to

$$a^{LH1} \rightarrow \frac{|\vec{D}'_{B880}|^2}{|\vec{D}_{B880}|^2} a^{LH1} \equiv a^{LH1} - \delta a \tag{5.25}$$

$$a^{P} \rightarrow a^{P} + \delta a \tag{5.26}$$

These equations predict a 90 % increase ($\delta a / a^P$) of absorption intensity in the P870 band.

5.4 Theory: Numerical Results.

The theory used in the last section, in which all the environmental degrees of freedom are captured by a simple lineshape function, does not take into account the possibly-nontrivial effects of the fluctuating environment that lead to exciton dephasing and localization. In this section, the absorption spectrum is calculated from a microscopic model which takes into account these effects, and it is shown to be

robust to harsh dephasing, which leads to homogeneous broadening of the spectrum, and static energy-level fluctuations, which lead to inhomogeneous broadening.

As discussed in Ch. 3, the unpolarized absorption spectrum $A(\omega)$ is obtained from the Laplace-Fourier transform of the dipole-dipole correlation function (DDCF) [67],

$$A(\omega) = \int_0^\infty \langle \vec{D}(t)\vec{D}(0)\rangle e^{i\omega t} dt \tag{5.27}$$

$$\approx \int_0^\infty \mathrm{Tr}\{e^{\mathcal{L}t}\vec{D}(0)\vec{D}(0)\rho^{(0)}\}e^{i\omega t} dt \tag{5.28}$$

$$\approx \sum_\alpha |\vec{D}_\alpha|^2 f(\omega - \omega_\alpha) \tag{5.29}$$

where $\rho^{(0)} \approx |0\rangle\langle 0|$ (the ground state) and the propagator $e^{\mathcal{L}t}$ contains the Hamiltonian evolution, according to Eq. 5.1, as well as the dissipative effects of the environment which act within the excitation lifetime (homogeneous broadening), modelled here using a Markovian master equation with the pure-dephasing superoperator $\mathcal{L}_d\rho = \sum_m \frac{\gamma_d}{2}(\sigma_z^m \rho \sigma_z^m - \rho)$, with $\sigma_z^m = |m\rangle\langle m| - |0\rangle\langle 0|$ and $\gamma_d = 106$ cm^{-1}, corresponding to a coherence time of $\tau = 50$ fs. With this dissipative model, the DDCF decays as $exp(-t/\tau)$. The homogeneously-broadened spectrum using the DDCF can be reproduced using the usual, and simpler, procedure of dressing excitonic stick spectra with a Lorentzian lineshape function, $L(\omega - \omega_\alpha) = \frac{1}{\pi}\frac{^1/_2\Gamma_{hom}}{(\omega-\omega_\alpha)^2+(^1/_2\Gamma_{hom})^2}$ with $\Gamma_{hom} = 2 \times \gamma_d$, according to Eq. 5.24 (Fig. 5.3 (C)). Indeed, this exact equivalence can be shown analytically by examining the evolution of the ground-excited-state coherence, $\rho_{0,\alpha}$, under the action of the dissipator, which is the quantity of interest

when calculating the DDCF.

$$\langle 0|\, \mathcal{L}_d \rho\, |\alpha\rangle = -\sum_{\alpha'} \rho_{0,\alpha'} \sum_n \gamma_n c_n^{\alpha} c_n^{\alpha'*} = -\gamma_d\, \rho_{0,\alpha} \tag{5.30}$$

where the last equality follows because the dephasing rate $\gamma_n = \gamma_d$ is the same for all pigments and the exciton states $|\alpha\rangle = \sum_n c_n^{\alpha} |n\rangle$ are orthonormal. Hence, the ground-exciton coherences decouple and decay mono-exponentially with a rate γ_d, which leads to a Lorentzian lineshape identitical to that obtained from the dressing procedure. However, when the coherence times of the RC and LH1 pigments differ, the hybrid (delocalized) states have a hybrid width weighted by the probability amplitudes. That is, the coherences mix because the evolution of $\rho_{0,\alpha}$ depends on $\rho_{0,\alpha'}$ with $\alpha \neq \alpha'$. Ignoring this mixing enables a dressing procedure whereby the decay rate is given by

$$\gamma_d^{\alpha} = \gamma_{RC}\, p_{RC}^{\alpha} + \gamma_{LH1}\, p_{LH1}^{\alpha}, \tag{5.31}$$

where γ_{RC} (γ_{LH1}) is the dephasing rate of the RC (LH1) pigments, and p_{RC}^{α} (p_{LH1}^{α}) is the probability of measuring exciton $|\alpha\rangle$ to be in the RC (LH1). As can be seen in Fig. 5.3 (C), this procedure overestimates the dark-minus-light contrast, as the neglected terms mix and destroy the delocalized excitons. In what follows, only equal coherence times of $\tau_{RC} = \tau_{LH1} = 50$ fs will be considered, as 3PEPS (three-pulse echo peak shift) experiments on both LH1 and RC have measured a homogeneous width of $\sim 200\ \mathrm{cm}^{-1} \approx \mathrm{kT}$ [49]. All coherences are destroyed using a pure dephasing

model as the system evolves towards a completely mixed state. Markovian Redfield equations or the non-Markovian hierarchy equations of motion could provide further insight into the effects of decoherence on the absorption spectrum, as information about the spectral density and the consequent inter-exciton dynamics is explicitly included [68]. In particular, such an approach captures the evolution of the system towards a near-Boltzmann steady-state distribution of excitons, which is reached within a few hundred femtoseconds to one picosecond [69].

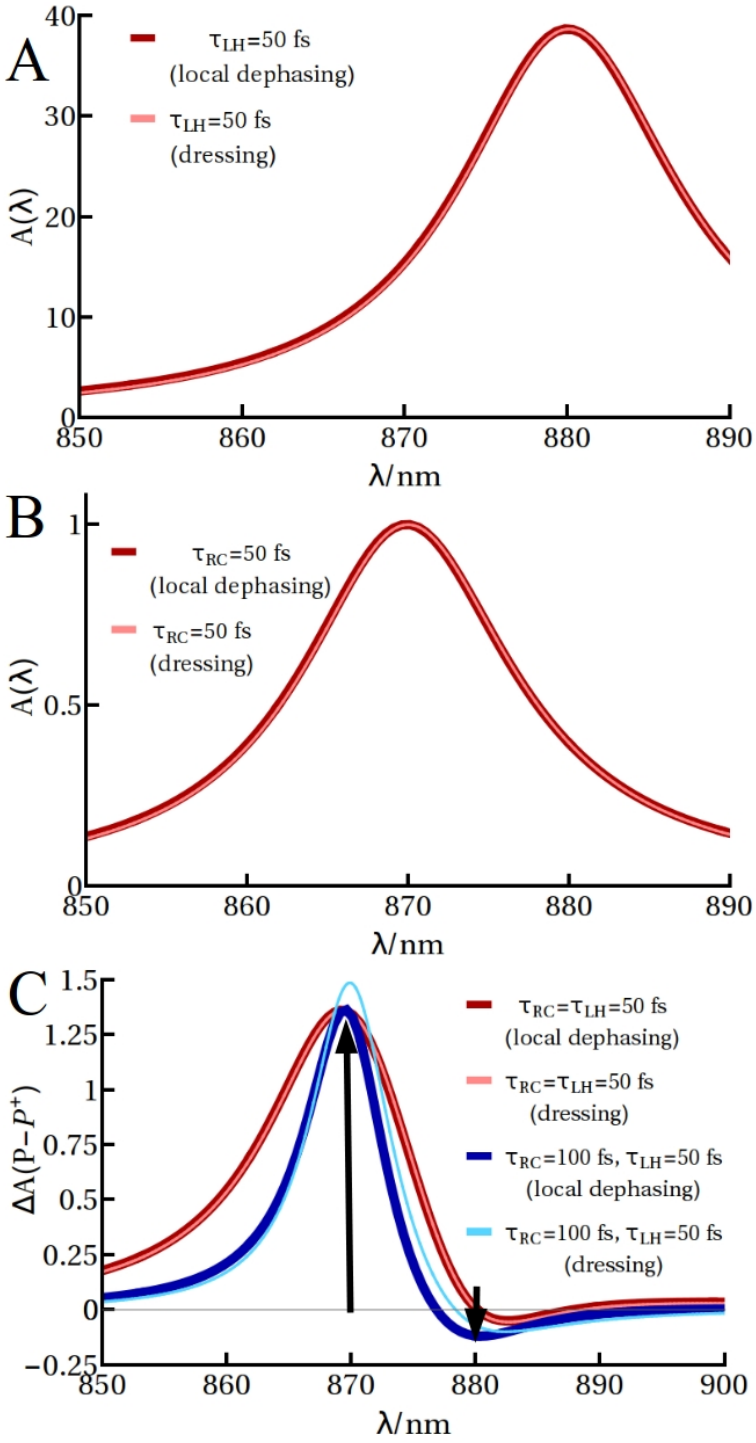

Figure 5.3: The homogeneously-broadened (A) isolated LH1, (B) isolated RC and (C) dark-minus-light spectra calculated using the DDCF, Eq. 5.28, are virtually indistinguishable from a simple dressing of stick spectra with Lorentzian lineshape functions according to Eq. 5.24 when the coherence times of the LH1 and RC pigments are the same.

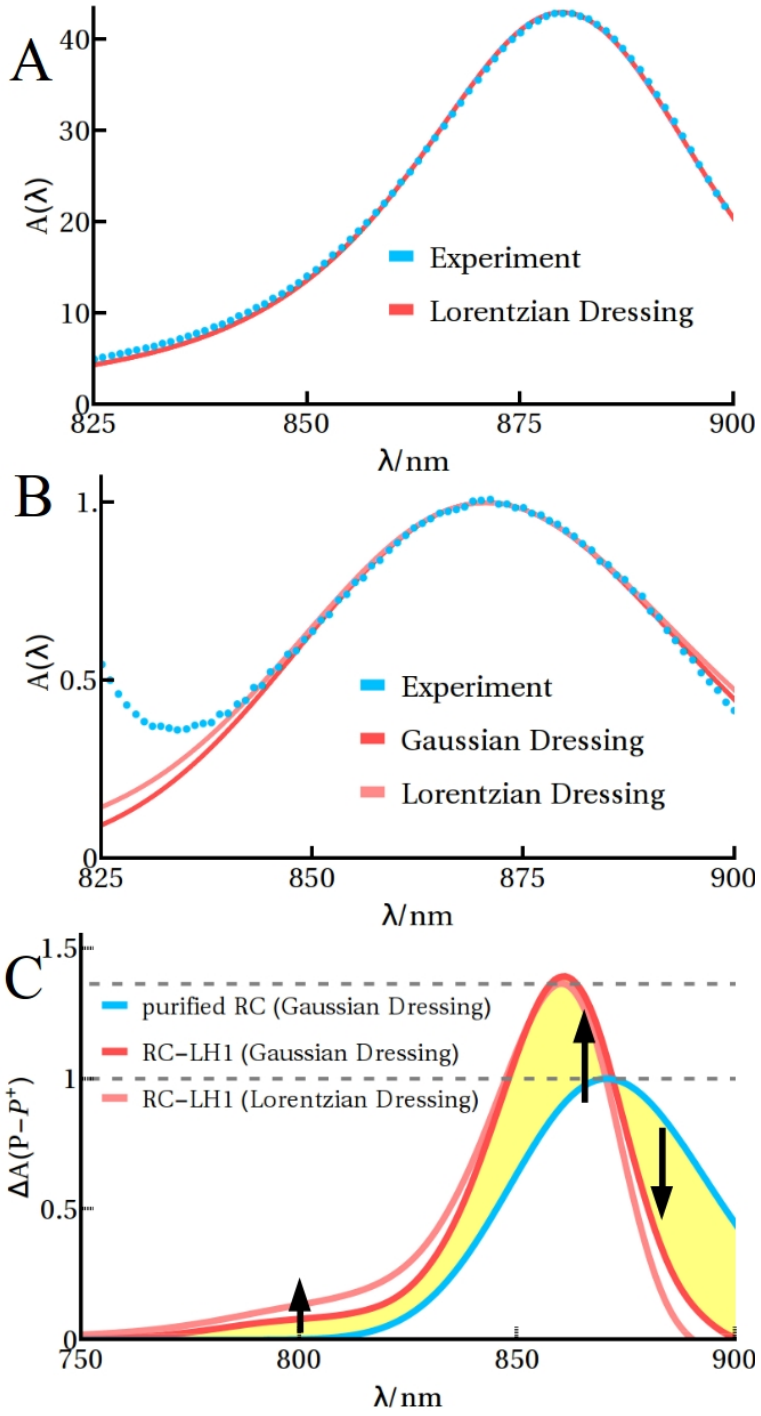

Figure 5.4: Dressing excitonic stick spectra with homogeneous lineshape functions and stochastic realizations of static energy-level fluctuations (A)-(B) reproduces experimentally-measured spectra of the isolated LH1 and isolated RC. The full dark-minus-light spectrum (C) drops sharply in the red compared to the experiment, Fig. 5.1 (D), due to spectral inhomogeneities, as discussed in the text. 500,000 realizations of static energy level fluctuations (diagonal disorder).

The homogeneous dressing function captures the short-time dynamics of the pigments coupled to their environment, and a Lorentzian lineshape corresponds to the Markovian dynamics modelled here. However, there is evidence that the time evolution of the P-pigments, the excited states of which have some charge-transfer character, is non-Markovian [58]. Less-harsh non-Markovian dynamics can lead to a decay of the DDCF which goes as $exp(-(t/\tau)^2)$. The corresponding lineshape is also Gaussian $G(\omega-\omega_\alpha) = \frac{1}{\sqrt{2\pi\sigma_{hom}^2}} exp\left(-(\omega-\omega_\alpha)^2/(2\sigma_{hom}^2)\right)$ with $\sigma_{hom} = \sqrt{2}\times\gamma_d$. The quasi-static fluctuations of the excitation energies (inhomogeneous broadening) can be modelled by performing stochastic realizations of the homogeneous spectrum with $\epsilon_i \rightarrow \epsilon_i + \delta_{\epsilon_i}$ in Eq. 5.1, where δ_{ϵ_i} is drawn from a Gaussian distribution with a standard deviation of $\sigma_{inhom}^{LH1} = 325$ cm^{-1} for the LH1 and $\sigma_{inhom}^{RC} = 385$ cm^{-1} for the P-pigments. Since the results from the DDCF are equivalent to the simple dressing procedure at the homogeneous level, the complete spectrum (homogeneous + inhomogeneous broadening) is calculated by performing stochastic averages of the dressed stick spectra due to computational complexity. This procedure, dressing the stick spectra of the P-pigments with Lorentzians and Gaussians, reproduces the experimentally-measured absorption spectrum of isolated LH1 and isolated RC, see Fig. 5.4 (B)-(C).

The calculated dark-minus-light spectrum of the complete core complex is robust to the microscopic details of environmental effects, Fig. 5.4 (C), but the experimental dark-minus-light spectrum cannot be well-fit with our parameters (compare to Fig. 5.1 (D)-(E)). A better fit is obtained if the inhomogneities are decreased, as dipole strength is not redistributed to higher-lying dark states of the LH1, which

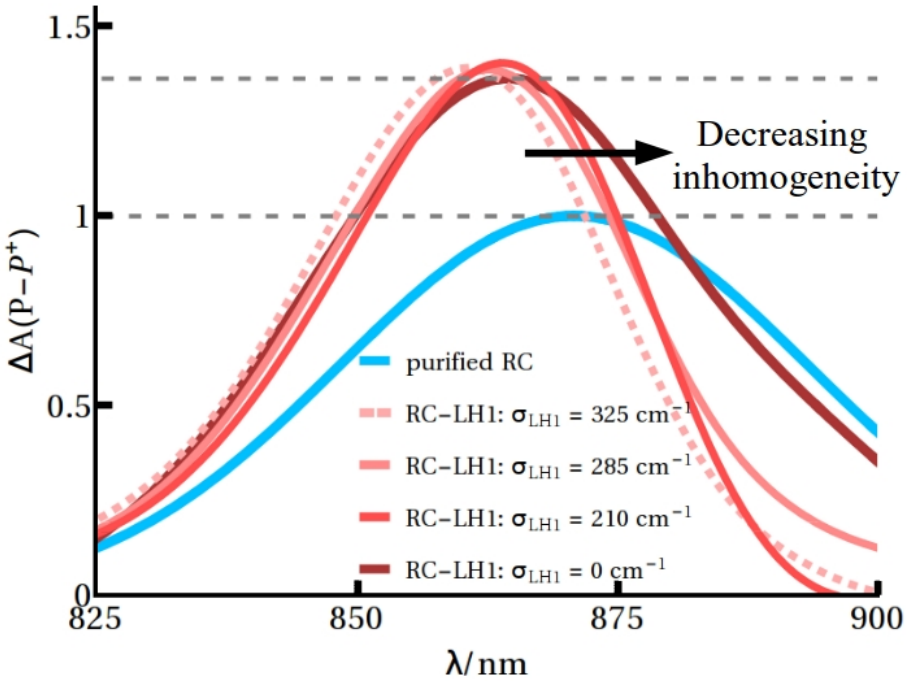

Figure 5.5: Inhomogeneous broadening, σ_{LH1}, of the LH1 absorption spectrum distributes dipole strength to dark states which may be close to resonance with the P870 exciton. Decreasing the spectral inhomogeneities of the LH1 leads to a better fit of the experimental dark-minus-light spectrum. For $\sigma_{LH1} = 325$ cm^{-1}, $J = 3.75$ cm^{-1}, for $\sigma_{LH1} = 285$ cm^{-1}, $J = 3.25$ cm^{-1}, for $\sigma_{LH1} = 210$ cm^{-1}, $J = 2.5$ cm^{-1} and for $\sigma_{LH1} = 0$ cm^{-1}, $J = 1.5$ cm^{-1}. Values ranging from $J = 1.4$ cm^{-1} to $J = 3.35$ cm^{-1} have been taken in the literature [70, 71]. For the $\sigma_{LH1} = 210$ cm^{-1} dark-minus-light spectrum, nearest-neighbor couplings were changed to $Q_1 = 300$ cm^{-1}, $Q_2 = 233$ cm^{-1} [71].

couple to the RC excitons and change the dark-minus-light lineshape (Fig. 5.5). An increased dephasing rate of $\gamma_d = 212$ cm^{-1}, corresponding to a dephasing time of 25 fs, requires an inhomogeneous broadening of $\sigma_{inhom}^{LH1} = 210$ cm^{-1} to capture the experimental width, and leads to a better fit. A better fit is also obtained by decreasing the nearest-neighbor couplings on the LH1 ring to $Q_1 = 300$ cm^{-1} and $Q_2 = 233$ cm^{-1} [71]; the homogeneous broadening remains fixed at $\gamma_d = 106$ cm^{-1}. This decreases the gap between exciton states according to Eq. 5.8 and, consequently, a smaller inhomogeneous broadening, $\sigma_{inhom}^{LH1} = 285$ cm^{-1}, is required to recover the experimental spectral width as dipole strength is more easily redistributed to the higher-lying dark states. Experimental measurements of fluorescence anisotropy of LH1 provide evidence for a predominance of homogeneous broadening at room temperature [57, 72–74], an assumption which would lead to the well-fit spectrum of Fig. 5.1 (E). In summary, the redistribution of absorption intensity is robust to the harsh dephasing and large inhomogeneities taken here, but a microscopic model with smaller inhomogeneities– perhaps justified with Redfield equations or the hierarchichal equations of motion and an explicit spectral density– is required for quantitative agreement.

5.5 Population Redistribution

The enhanced absorption of the P870 band leads to the excitation of a state that is partially delocalized over P and LH1 pigments, so it is not immediately clear that increased absorption at 870 nm implies the increased excitation of the P-

pigments, which is desirable as it places excitations directly where charge separation takes place. Under weak incoherent illumination, the excitation rate R_α can be determined by Fermi's Golden Rule, and hence $R_\alpha \propto |D_\alpha|^2$. We have shown that absorption is best described by states $|\alpha'\rangle$ which are delocalized over the RC and LH unit. Hence, the distribution of excited states upon excitation, ρ^{exc}, is best-described by a statistical mixture of the delocalized states $|\alpha'\rangle$, with weights given by their respective excitation rates, and hence, their dipole strengths

$$\rho^{exc} = \frac{\sum_{\alpha'} R_{\alpha'} |\alpha'\rangle \langle\alpha'|}{\sum_\alpha R_{\alpha'}} = \frac{\sum_{\alpha'} |\vec{D}_{\alpha'}|^2 |\alpha'\rangle \langle\alpha'|}{\sum_\alpha |\vec{D}_{\alpha'}|^2}. \tag{5.32}$$

Hence, the population in the special pair is calculated, using equations 5.14, 5.15, 5.19 and 5.23, to be

$$P_P = Tr\{\rho^{exc} |P\rangle \langle P|\} \tag{5.33}$$

$$= \frac{|\vec{D}_{P870}|^2(3+\cos 4\theta) + 2\Re\left\{\vec{D}^*_{P870} \cdot \vec{D}_{B880}\right\} \sin 4\theta + |\vec{D}_{B880}|^2(1-\cos 4\theta)}{4(|\vec{D}_{P870}|^2 + |\vec{D}_{B880}|^2 + |\vec{D}_\emptyset|^2)} \tag{5.34}$$

where Tr is the trace operation. The results for the RC-LH1 geometry can be generalized to any number of M excitonically-coupled harvesting units encircling the N pigments that initiate charge separation in the RC using $|\vec{D}_{P870}|^2 = N|\vec{d}^{RC}|^2$, $|\vec{D}_{B880}|^2 = {}^M/_2 |\vec{d}^{LH1}|^2$ and $|\vec{D}_\emptyset|^2 = {}^M/_2 |\vec{d}^{LH1}|^2$. The requirement that many harvesting pigments should surround fewer charge separation pigments in order to increase the excitation of charge separation pigments, is illustrated by expanding Eq. 5.34

to second order in $\frac{V}{\Delta E}$ and assuming, for simplicity, $|\vec{d}^{LH1}|^2 = |\vec{d}^{RC}|^2$

$$P_P = \frac{1}{M+N}\left(N + \sqrt{2MN}\left(\frac{V}{\Delta E}\right) + (M-2N)\left(\frac{V}{\Delta E}\right)^2 + \ldots\right). \qquad (5.35)$$

In the particular case of the core complex these correspond to $M = 32$ pigments for the LH1 and $N = 2$ pigments for the special pair. Full numerical simulations of the complete core complex result in a two-fold average increase of population P_P due to extended delocalization over antenna pigments, and it provides the initial condition for dynamical simulations of Excitation Energy Transfer (EET), described in a later section.

5.6 Extension to Other Species and Higher Plants

The redirection of excitation towards the special pair due to extended quantum delocalization can be generalized to other organisms by theoretical analysis. When environmentally-induced disorder is included, numerical simulations predict similar redistributions of excitation population in purple bacteria species *Rb. sphaeroides* and *Rps. palustris* ($N = 2, M = 28 - 32$), which show structural deviations from a closed circular ring, see Fig. 5.6.

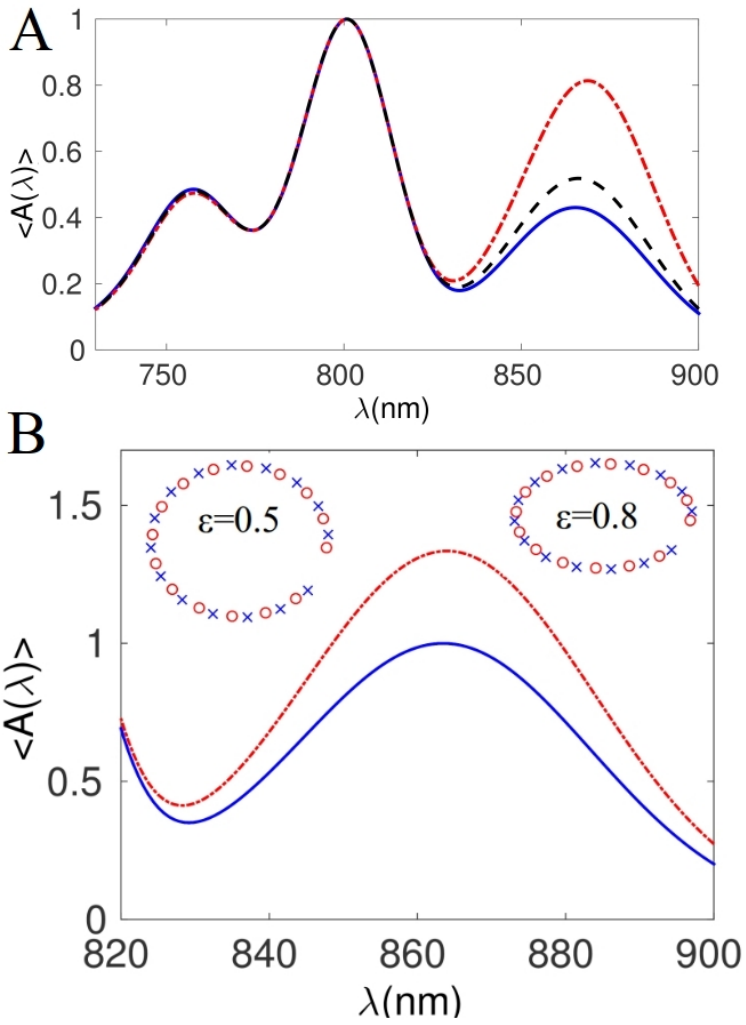

Figure 5.6: (A) The RC spectra of purple bacteria species *Rb. sphaeroides* shows an enhancement of the special pair absorption when delocalization over its harvesting antenna LH1 is taken into account. The calculated spectra of the isolated RC (solid blue), of the RC-LH1 using the bare BChl dipole moment 6.3 D (dashed black) and of the RC-LH1 using a hyperchromic dipole moment $\sqrt{2.4}$ 6.3 D = 9.8 D (dash-dotted red). Hyperchromism in this case refers to the dipole strength borrowing of the Q_y band from the Soret band, leading to a larger apparent dipole moment. (B) The purple bacteria species *Rps. palustris* could exhibit an elliptical and broken ring, as pictured in the inset. Despite these structural perturbations, the special pair band exhibits an enhancement when extended delocalization over the antenna complex is taken into account (dash-dotted red) as compared to the isolated RC (solid blue). Simulations performed by F.C.-S.

To explore the effects of extended delocalization in Photosystem 1 (PS1) and

Photosystem 2 (PS2), the main light-harvesting photo-units in higher plants [75], we examine Hamiltonians of the form

$$\mathscr{H} = \begin{pmatrix} \mathscr{H}_{RC} & V \\ V & \mathscr{H}_{LH} \end{pmatrix} \tag{5.36}$$

where $\mathscr{H}_{RC}$ is the Hamiltonian of the full RC alone and $\mathscr{H}_{LH}$ is the Hamiltonian of the isolated antenna complexes. The coupling between RC and LH pigments is captured by the matrix V. In this simplified calculation, site energies are taken from the literature and couplings between pigments are calculated in the point-dipole approximation using $d = 4.48$ D, $\kappa = 1$ and $d = 4.4$ D, $\kappa = 1.5$ for PS1 and PS2, respectively [76–78]. Dipole moments, $\vec{D}_i$, are calculated along the direction connecting the N_B and N_D atoms of the porphyrin rings of each chlorophyll using the atomic coordinates taken from the X-ray structures (Protein Data Bank (PDB) accession codes 1JB0 and 3ARC, the latter now obsolete and superseded by 3WU2), and rotated 15° towards N_C in the case of PS2 [33, 79]. Fluctuations in the pigment energies, drawn from a Gaussian distribution, capture spectral inhomogeneities, which are known to fluctuate with temperature. We take Gaussian standard deviations of $\sigma = 80$ cm^{-1} (fit from low temperature spectra) and $\sigma = 28$ cm^{-1} (fit from room temperature spectra) for PS1 and PS2, respectively [80,81]. For each realization of the Hamiltonian, $\mathscr{H}$, we find a unitary U which diagonalizes it and calculate the dipole moments of the exciton states, $|k\rangle = \sum_i U_{i,k} |i\rangle$, according

to $\vec{D'}_k = \sum_i U_{i,k}\vec{D}_i$. The population in the P pigments is calculated according to:

$$\rho^{exc} = \frac{\sum_\alpha |\vec{D'}_\alpha|^2 \, |\alpha\rangle \langle\alpha|}{\sum_\alpha |\vec{D'}_\alpha|^2}, \tag{5.37}$$

$$P_P = \sum_{i=1}^{N} Tr\{\rho^{exc} \, |P_i\rangle \langle P_i| \}. \tag{5.38}$$

where $N = 2$ for PS1 and PS2 monomer and $N = 4$ for the PS2 dimer. We compare the calculation of equation 5.38 for $V = 0$ (uncoupled RC and antennae) and $V \neq 0$ (coherently coupled RC and antennae). In PS1 ($N = 2, M = 83$), our analysis, summarized in Figs. 5.7 and 5.8, indicates a 14 % increase of the excitation population of the P-pigments due to excitonic delocalization over antenna pigments. For the PS2 we predict a 12 % increase in P-excitation for both the monomer ($N = 2, M = 35$) and natural dimeric structure ($N = 4, M = 70$). These calculations predict an increase in the excitation of P pigments due to excitonic delocalisation over antenna chlorophylls observed in the X-ray structures. Excitation redistribution from antenna to P pigments is robust to, albeit reduced by, disorder. A more sophisticated calculation, which we leave for a future work, will likely require the determination of nearest-neighbor couplings beyond the dipole-dipole approximation, which is known to break down at distances of approximately 10 $\mathring{A}$.

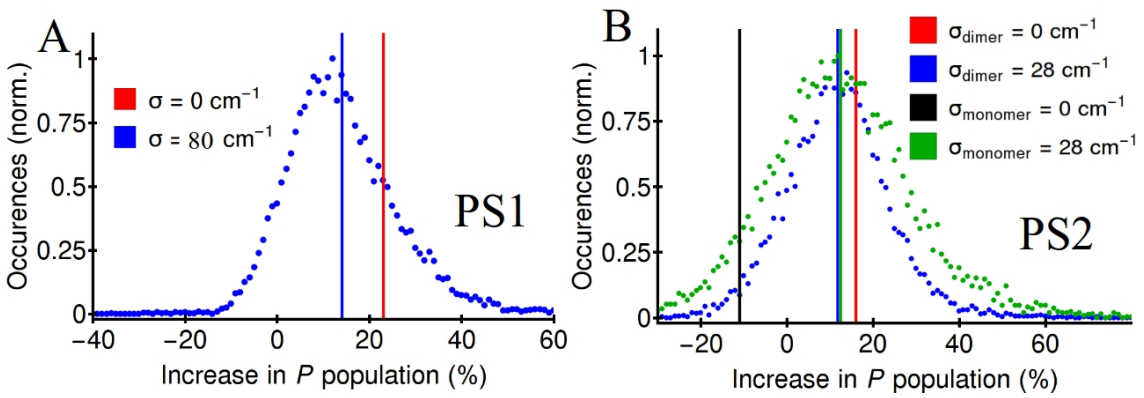

Figure 5.7: Excitation redistribution from antenna to P pigments in PS1 (A) and PS2 (B) is robust to Gaussian disorder in the site energies. The average change of P population in PS1 shifts from +23% with no disorder to +14% with 80 cm^{-1} inhomogeneous broadening; the distribution has a Lorentzian FWHM of 20%. In the PS2 dimer, the redistribution shifts from +16% with no disorder to +12%, Gaussian std 11%, with 28 cm^{-1} inhomogeneous broadening, and the PS2 monomer shifts from −11% to +12%, std +15%, with the same inhomogeneous broadening. Hence, although disorder eliminates the difference between the PS2 dimer and monomer in average, extended couplings in the dimer increase robustness to site energy fluctuations, as the distribution is narrower for the dimer.

5.7 Design Principles: Population Redistribution

In fact, Eq. 5.34 holds generally for any excitonic system which can be reduced, by symmetry and the subsequent selection rules, to a two-level system. It is interesting, then, to examine the extent to which the design of the LH1-RC unit is optimized with respect to the population redistribution due to excitonic delocalization, as such a study may suggest general design principles for efficient light-harvesting. As shown above, the population in the "target" pigments, P_T – in the case that the excitonic

system can be reduced to a two-level system

$$H = \begin{pmatrix} \Delta E & V \\ V & 0 \end{pmatrix} \tag{5.39}$$

due to symmetry/selection rules– depends on the dipole moments of the isolated target and antenna excitonic bands $\vec{D}_T$ and $\vec{D}_A$, respectively, according to

$$\begin{aligned} P_T &= Tr\left\{\rho^{exc}\left|T\right\rangle\left\langle T\right|\right\} && (5.40)\\ &= \frac{1}{4(M+N)\,d^2}\Big\{|\vec{D}_T|^2(3+\cos 4\theta)+ \\ &\quad + 2\Re\left\{\vec{D}_T^{*}\cdot\vec{D}_A\right\}\sin 4\theta+ \\ &\quad + |\vec{D}_A|^2(1-\cos 4\theta)\Big\} && (5.41)\end{aligned}$$

where M and N are the total number of antenna and target pigments, respectively and $\theta = \frac{1}{2}\arctan\left(\frac{2V}{\Delta E}\right)$. Assuming that $\Re\left\{\vec{D}_T^{*}\cdot\vec{D}_A\right\} = D_T D_A$, which holds in the cases we will consider, the optimal angle θ (that is, the optimal energy landscape), can be found according to

$$\frac{dP_T}{d\theta} \equiv 0 \rightarrow \tan 4\theta = \frac{2D_T D_A}{D_T^2 - D_A^2}. \tag{5.42}$$

Choosing this energy landscape, the maximal population in the target pigments is then

$$P_T^{max} = \frac{D_A^2 + 2D_T^2}{2(M+N)}. \tag{5.43}$$

On the other hand, if one considers a landscape in which the system is resonant, $\Delta E \to 0$, then $\theta \to \pi/4$ and the population redistributed is

$$P_T^{res} = \frac{D_A^2 + D_T^2}{2(M+N)}, \tag{5.44}$$

which is smaller ($P_T^{res} < P_T^{max}$).

In the case of the RC-LH1, where the antenna dipoles are tangent to the ring, the dipole strength is concentrated in two exciton states $k = \pm 1$, but only one of these states couples to the RC, so we have

$$|\vec{D}_A|^2 = \frac{M}{2},\ |\vec{D}_T|^2 = N \tag{5.45}$$

$$P_T^{max} = \frac{M/2 + 2N}{2(M+N)} \underset{M\to\infty}{\to} \frac{1}{4} \tag{5.46}$$

$$P_T^{res} = \frac{M/2 + N}{2(M+N)} \underset{M\to\infty}{\to} \frac{1}{4}. \tag{5.47}$$

However, if the dipoles are perpendicular to the plane of the ring and parallel (like a "sheaf of arrows"), the dipole strength is concentrated in a single exciton

state $k = 0$, and the population redistribution is even greater

$$|\vec{D}_A|^2 = M,\ |\vec{D}_T|^2 = N \tag{5.48}$$

$$P_T^{max} = \frac{M + 2N}{2(M + N)} \underset{M\to\infty}{\to} \frac{1}{2} \tag{5.49}$$

$$P_T^{res} = \frac{M + N}{2(M + N)} \underset{M\to\infty}{\to} \frac{1}{2}. \tag{5.50}$$

These expressions show that, by a suitable choice of geometry and energy landscape, one can direct more than 50 % of the excitation to the target pigments. Numerical calculations which explore random pigment arrangements show that Eq. 5.49 is the best that one can do.

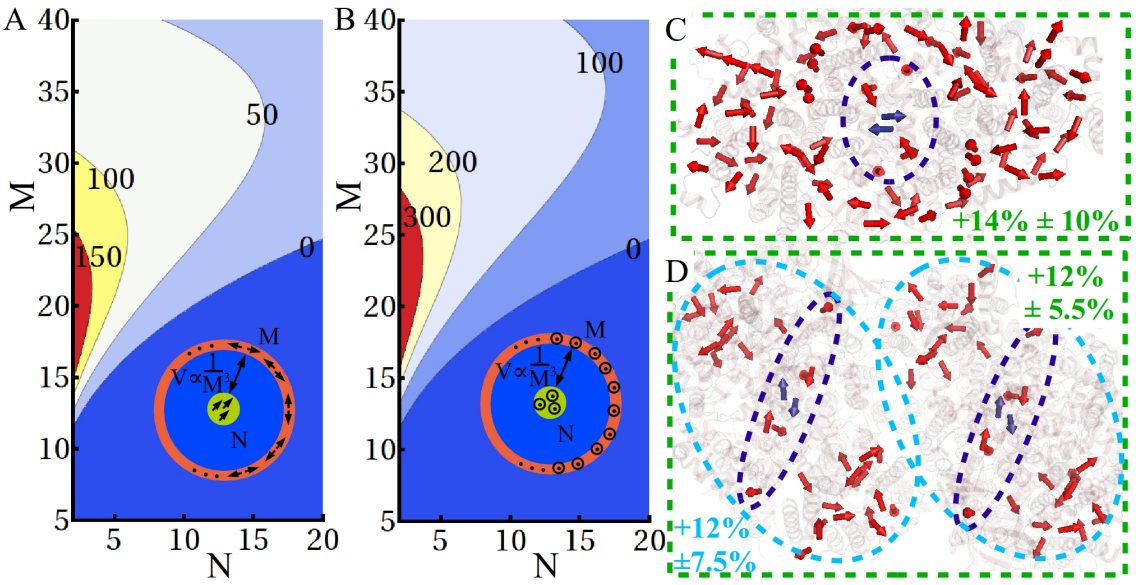

Figure 5.8: Using a simplified model for a general circular aggregate (A) and (B), the percent increase of the initial excitation of the P-pigments is calculated as a function of the number N of P-pigments and number M of LH pigments. The enhancement of direct P-pigment excitation requires $N \ll M$ and is maximized for $M \sim 20 - 25$. PS1 (C) and PS2 (D) exhibit clustering of many LH pigments around fewer RC pigments (bound in dark blue). The excitation population of the P-pigments (dark blue arrows) *increases* when extended delocalization over all antenna pigments (bound in green) is taken into account. Error bound corresponds to the width of distribution when averaging over the effects of environmental disorder.

However, it is important to note that, as the number of ring pigments increases, the radius of the ring increases linearly for a fixed inter-pigment distance. In the case of the RC-LH1 this distance is likely fixed by the protein $\alpha\beta$ subunit. Hence, the coupling between antenna exciton and target exciton is $V = J\sqrt{\frac{MN}{2}}\left(\frac{32}{M}\right)^3$ if the dipoles are in the plane of, and tangent to, the ring and $V = J\sqrt{MN}\left(\frac{32}{M}\right)^3$ if the dipoles are perpendicular to the plane of the ring (and hence parallel to each other).

Fig. 5.8 plots the percent increase in P-population due to extended delocalization

$$\Delta P_P = \frac{\Big(P_P - N/(M+N)\Big)}{N/(M+N)} \times 100 \tag{5.51}$$

for varying M and N using the population redistribution Eq. 5.41 with J = 1.5 cm^{-1}. Figure 5.8 (A) and (B) shows that the optimal population redistribution from LH to RC occurs when the RC contains a small number of pigments, N, able to initiate charge separation, while the LH unit contains a few tens of pigments, M, i.e. $N \ll M$, as expected from Eq. 5.35. Photosynthetic complexes typically contain $N = 2$ pigments which promote charge separation. In this case, the maximal enhancement for direct excitation is achieved with $M \sim 20 - 25$ pigments in the LH unit, closely resembling the LH1 structure. The RC-LH configuration with all dipoles parallel to each other and perpendicular to the plane of the ring, Fig. 5.8 (B), shows enhancements of greater than 300 %.

5.8 Charge Separation Dynamics

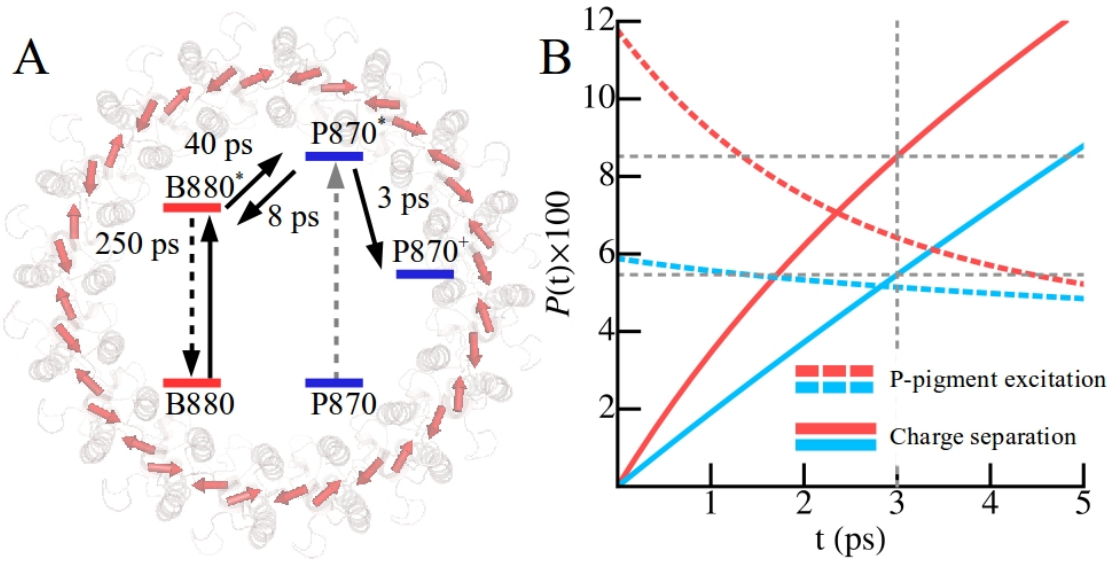

Figure 5.9: (A) Transport dynamics in *R. rubrum* can be accurately modeled using classical rate equations. (B) Both the initial excitation of P-pigments ($P_P(t)$ (dashed lines)) and the resulting process of charge separation, $P_{P^+}(t)$ (solid lines), are increased when absorption is delocalized across the core complex (red) as compared to absorption occuring either on the RC or LH1 (blue). The enhancement is relevant on a timescale comparable to the charge separation process (3 ps, grey line), well before EET from LH1 to RC takes place (∼40 ps). The initial excitation of P-pigments increases from $\frac{2}{34}$ to $\frac{4}{34}$ (an increase of 100%), and results in a $\sim 1\%$ increase in photosynthetic efficiency at long times.

The EET between the RC and LH1 occurs via a Coulomb exchange mechanism on a picosecond time-scale [28], while vibrational dephasing destroys coherences in hundreds of femtoseconds [3, 82]. The Coulomb interaction de-excites an initially excited electron in the donor complex while simultaneously exciting an electron in the acceptor complex. As dephasing occurs, the excited states of donor and acceptor acquire random relative phases, which inhibits quantum mechanical delocalization. Transfer rates measured from pump-probe experiments agree with those obtained

from calculations using generalized Förster theory [28]. The theoretical approach to date averages transfer from different excitonic delocalized states from a donor complex, assumed to be in a canonical equilibrium of excited states, to the acceptor complex. LH1→ RC transfer occurs through the second and third lowest exciton lying states, giving rates in agreement with an experimentally measured transfer time of $f = 40$ ps [83,84]. Back transfer from RC to LH1 occurs in a calculated time of $b = 8.1$ ps [85], close to the experimentally measured 7-9 ps, which was estimated from decay kinetics after RC excitation [86], and further verified numerically by careful modelling of environmental effects [70]. The first electron transfer step, $P^* \rightarrow P^+$, occurs in the RC within $c = 3$ ps [87]. Fluorescence, inter-system crossing, internal conversion and further dissipative mechanisms, have been included in kinetic models with a single lifetime of $l = 250$ ps [72]. The rates are presented schematically in Fig. 5.9.

Excitonic transfer among LH1 and RC pigments occurs in a regime where coherent delocalisation across RC and LH1 shows no appreciable effects [70]. Therefore, to describe excitation transfer in the core complex a model of classical rate equations taking into account LH1, P, a charge separation state P^+ and a loss sink

is sufficient. The system evolves according to

$$\begin{aligned}
\dot{p}_{LH1} &= -\frac{1}{f}\,p_{LH1} + \frac{1}{b}\,p_P - \frac{1}{l}\,p_{LH1} \\
\dot{p}_P &= \frac{1}{f}\,p_{LH1} - \frac{1}{b}\,p_P - \frac{1}{c}\,p_P - \frac{1}{l}\,p_P \\
\dot{p}_{P^+} &= \frac{1}{c}\,p_P \\
\dot{p}_{loss} &= \frac{1}{l}\,(p_{LH1} + p_P),
\end{aligned} \tag{5.52}$$

with the initial conditions

$$\begin{aligned}
p_P(0) &= P_P \\
p_{LH1}(0) &= 1 - P_P \\
p_{P^+}(0) &= 0 \\
p_{loss}(0) &= 0.
\end{aligned} \tag{5.53}$$

For the case of coherently coupled LH1-RC, P_P follows from Eq. 5.33, while $P_P = N/(N+M)$ when the interaction between P-pigments and the LH1 is neglected. As shown in Fig. 5.9 (B), the probability of charge separation, $P_{P^+}(t)$, increases very slightly (about 1 % at long times) as extended delocalization focuses the excitation into the special pair, allowing the excitation to avoid the slow transfer step from LH1 to RC. This increase in charge separation provides a quantitative link between a coherent quantum effect and enhanced functionality, although it may be too small to be biologically relevant or exert evolutionary pressure.

5.9 Design Principles: Charge Separation Dynamics

The effects of the population redistribution on subsequent charge separation can be better understood by a close examination of Eqs. 5.52, which can be solved analytically for the probability of charge separation at long times

$$p_{P^+}(t \to \infty) = b\, l \left(\frac{l + f P_P}{c\, f\, l + b(c+l)(f+l)} \right). \tag{5.54}$$

We are interested in the increase of charge separation due to extended delocalization, which changes the initial condition P_P. Defining $\delta = \frac{2}{34}$ to be the initial population in the P-pigments without extended delocalization, and $\tilde{\delta} \approx \frac{4}{34} > \delta$ with extended delocalization, the percent increase in charge separation, which is the change in efficiency $\Delta\epsilon$, is given by:

$$\Delta\epsilon = \frac{f\,(\tilde{\delta} - \delta)}{l + f\,\delta} \tag{5.55}$$

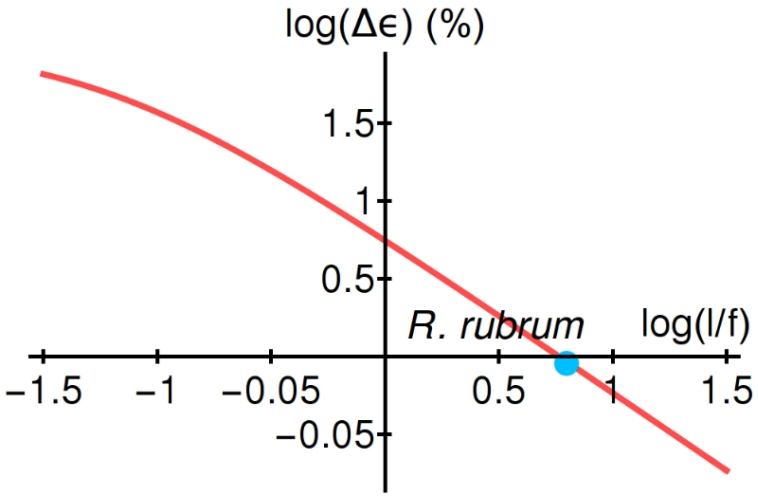

Figure 5.10: Increase in efficiency due to quantum delocalization as a function of the relevant incoherent transfer rates, l and f, according to equation 5.55. Since transfer between light-harvesting units occurs much more quickly than excitation loss ($l/f \sim 6$), the increase in efficiency is small for *R. rubrum*. However, this plot illustrates that this design principle could lead to higher increases in efficiency in artificial systems like quantum dots and, in general, when the system is limited by loss ($l/f < 1$).

Figure 5.10 shows the increase in charge separation according to Eq. 5.55 for variable values of l/f, the ratio of the dissipation to the forward transfer time scales, which determines the increase in efficiency. Since $f > l$ in *R. rubrum*, charge separation is very efficient ($\sim 83\%$) and the benefit from population redistribution due to extended delocalization is small ($\sim 1\%$). However, for lossy systems $f < l$, the benefit of extended delocalization can be very large. Figure 5.11, discussed below, gives a concrete example of a system where the probability of charge separation increases from 0.21 to 0.33, an increase in efficiency of 54 %.

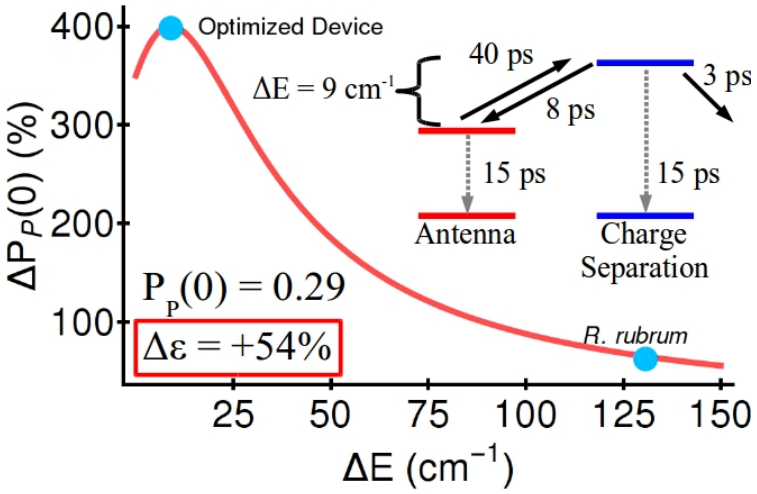

Figure 5.11: Tuning the resonance condition, $\Delta E = 9$ cm^{-1}, maximizes the population redistribution ($P_P = \frac{10}{34} = 0.29$) according to Eq. 5.34, leading to a 400 % increase in direct excitation of the P-pigments. For a situation in which the pigments are subject to fast losses (f = 40 ps, b = 8 ps, c = 3 ps, l = 15 ps), the population redistribution increases the probability of charge separation from 0.21 to 0.33, a 54 % increase in efficiency.

A quantitative understanding of light harvesting in the LH1-RC complex illuminates clear design principles for devices engineered to direct light collection. These principles could prevent photobleaching and lengthen the lifetime of harvesting devices by directing absorption to stable target pigments, in addition to increasing the efficiency from photon absorption to charge separation. By tuning the resonance condition ΔE in a ring-like geometry, a 400% increase in the absorption of a few target pigments can be achieved. Moreover, in devices where dissipation is fast ($\sim$ 15 ps as opposed to 250 ps in LH1 [72]), these configurations will lead to a 54% gain in achieving charge separation following photon absorption.

5.10 Outlook

In conclusion, theoretical considerations have led us to identify a new design principle which exploits quantum delocalization to redirect light absorption to the RC in several photosynthetic systems. Given the generality of the design principle described here, it is tempting to equate this principle with increased evolutionary fitness of certain biological systems. We use the term evolutionary fitness here to describe an adaptive property which may help an organism survive under given environmental conditions (e.g. low light intensity), and not in its usual context of increased growth rate, which may be determined by other factors not under consideration here. We have verified this principle experimentally in the core complexes of *R. rubrum*, and our detailed theoretical analysis illuminates clear guidelines for the design of light-harvesting devices that direct photon absorption. This new quantum design principle provides a quantitative link between structure and function, broadening our understanding of the role of quantum mechanics in light harvesting.

Chapter 6: Collective Plasmon Resonance Directs Absorption in Metal-Nanoparticle Arrays

The main task of this thesis has been to describe the changes to absorption spectra, and the consequently modified excitation transport, when a light-harvesting (LH) antenna is coupled to a reaction center (RC), where charge separation takes place. It was shown that, regardless of the coherent or incoherent nature of transport, absorption is a coherent process. Accordingly, extended delocalization over the LH antenna and RC must be taken into account in an accurate description of the absorption process. It was shown that this (quantum-mechanical) collective effect directs absorption to the RC, enhancing the photosynthetic efficiency as less excitation must travel from the antenna to the RC, possibly decaying and being lost along the way. In this chapter, we examine a mesoscopic system of classical dipoles which is calculated to exhibit the same behavior. In particular, we propose an experiment involving commercially-available polarizable metal nanoparticles anchored to a 2-dimensional scaffold of DNA in a circular arrangement resembling the RC-LH1 core complex. It will be shown that the collective resonances of the system can be engineered such that the absorption of a central, spectrally-distinct nanoparticle can be increased by 60 %. This represents the first step towards an

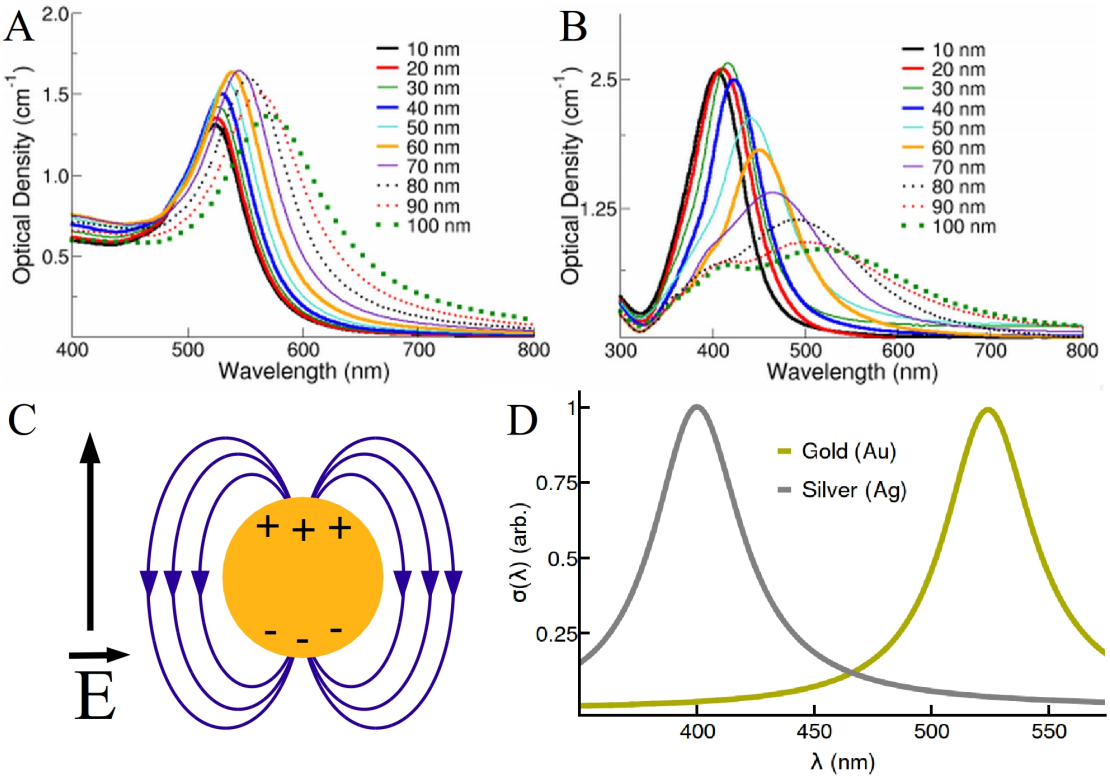

Figure 6.1: Measured extinction (the sum of scattering and absorption) of commercially-available gold (A) and silver (B) nanoparticles (*reproduced from Ref. [88, 89]*). Theoretically, the collective plasmonic resonance of the surface electrons can be described, when sufficiently far from the nanoparticle, using Mie theory truncated at the dipolar term. In this formalism, the metal nanoparticle is a polarizable dielectric which emits a dipole field, as in (C), when excited by a polarized field. The calculated absorption of 10 nm nanoparticles using this theory (D) agrees well with experiment.

artificial nano-device which exploits the tunable funnelling of absorption in order to optimize light-harvesting. Finally, the analytical results derived here are general to polarizable media, and we leave open to speculation the application of these principles to other wavelength regimes. The microwave regime, for example, could have consequences for wireless communication and charging of personal electronics.

6.1 Plasmonic Resonance of Metal Nanoparticles

The metal nanoparticles we will consider are mesoscopic objects (radius $a =$ 10 nm) and there are consequently many electrons ($\sim 10^5$– 10^6, as compared to ~ 10 in the case of BChl) involved in the (classically) coherent oscillations driven by light [90]. These oscillations are indeed classically coherent, as it is known from hole-burning experiments that the (quantum) coherence time is about 10 femtoseconds [91, 92]. The frequent collisions quickly destroy quantum superpositions, and a classical theory is sufficient. Consequently, a theory of their optical properties considers metal nanoparticles as spherical dielectrics with a classical polarizability α and permittivity ϵ, modelled using a Drude spectral density, excited by light with electric field $\vec{E}$

$$\vec{d} = \alpha \vec{E} \tag{6.1}$$

$$\alpha(\omega) = a^3 \frac{\epsilon(\omega) - 1}{\epsilon(\omega) + 2} \tag{6.2}$$

$$\epsilon(\omega) = 1 - \frac{\omega_p^2}{\omega(\omega + i\nu)}, \tag{6.3}$$

where $a = 10$ nm is the radius of the nanoparticle, and the width ν and plasma frequency ω_p are chosen– or derived from boundary conditions, like particle size– such that the single particle spectrum (resonance $\omega_0 = \omega_p/\sqrt{3}$) agrees with experiment [92–94]. Hole-burning experiments on Au nanoparticles find a homogeneous width of 25 THz, but we take $\nu_{Au} = \nu_{Ag} = 50$ THz, for gold (Au) and silver (Ag) nanoparticles, to reproduce the full experimental width. A more rigorous calcu-

lation would take into account inhomogeneous broadening by stochastic averages over excitation energy, as in Ch. 4 and Ch. 5, and is left for a future work. The polarizability is derived by enforcing Maxwell's equations at the interface between the nanoparticle and the surrounding medium [90]. As the particle is polarizable, the induced dipole moment aligns with the field, which will play an important role in the following. An expression for the extinction coefficient is well-known

$$\sigma(\omega) \propto \omega \sum_{i=1}^{N} Im\left(\vec{E} \cdot \vec{d_i}\right). \tag{6.4}$$

This simple theory, known as Mie theory, reproduces experimental absorption spectra, as shown in Fig. 6.1. Importantly, the plasmon resonance is red-shifted for increasing nanoparticle size.

6.2 Collective Resonance: Two Nanoparticles

When multiple nanoparticles are brought in proximity, the total field experienced by nanoparticle i upon excitation is composed of the external incident field, $\vec{E}_{ext,i}$ and the induced electric field emitted from other nanoparticles $\vec{E}_{ind,i}$. Hence, an aggregation of metal nanoparticles exhibits modified optical properties. This effect has been observed in systems of metal nanoparticles tethered to DNA helices, where the collective plasmon resonance of the nanoparticles mirrors the geometry of the helix, leading to a non-zero circular-dichroism (CD) signal in the visible [95, 96]. Mathematically, the induced dipole moments of the collective system obey the set

of coupled equations

$$\vec{d}_i = \alpha \left(\vec{E}_{ext,i} + \vec{E}_{ind,i} \right) \tag{6.5}$$

$$\vec{E}_{ind,i} = \sum_{j \neq i} \left[\frac{3(\vec{d}_j \cdot \vec{n}_{ji})\vec{n}_{ji} - \vec{d}_j}{r_{ji}^3}(1 - ikr_{ji}) + k^2 \frac{\vec{d}_j - (\vec{d}_j \cdot \vec{n}_{ji})\vec{n}_{ji}}{r_{ji}} \right] e^{ikr_{ji}}. \tag{6.6}$$

where $\vec{n}_{ji} = \vec{r}_{ji}/r_{ji}$. If the separation between nanoparticles is much smaller than the wavelength, $kr_{ij} \ll \lambda$, retardation effects can be ignored and Eq. 6.6 simplifies greatly

$$\vec{E}_{ind,i} = \sum_{j \neq i} \frac{3(\vec{d}_j \cdot \vec{n}_{ji})\vec{n}_{ji} - \vec{d}_j}{r_{ji}^3}. \tag{6.7}$$

The most important features of the collective resonance can be understood by examining a system of two coupled particles as illustrated in Fig. 6.2. The particles are separated by $\vec{r} = 3 \times$ a $\hat{x} = 30$ nm $\hat{x}$. The incident light is assumed to propagate along the z-axis with polarization $\vec{E}_{ext,i} = E_0(\sin\theta\hat{x} + \cos\theta\hat{y})$. Equations 6.5 decouple along different axes, leaving the system of equations, using the simplified theory of Eq. 6.7

$$d_i^x = \alpha \left(E_0 \sin\theta + \sum_{j \neq i} \frac{2d_j^x}{r^3} \right) \tag{6.8}$$

$$d_i^y = \alpha \left(E_0 \cos\theta - \sum_{j \neq i} \frac{d_j^y}{r^3} \right). \tag{6.9}$$

These equations can be solved by simple substitution to yield

$$\vec{d_i} = \alpha E_0 \begin{pmatrix} \frac{\sin\theta}{1-\frac{2\alpha}{r^3}} \\ \\ \frac{\cos\theta}{1+\frac{\alpha}{r^3}} \end{pmatrix} \tag{6.10}$$

$$\vec{d_1} = \vec{d_2}. \tag{6.11}$$

The shifted collective resonances illustrated in Fig. 6.2 can be understood by Eq. 6.10-6.11. If the incident field is polarized *perpendicular* to the vector connecting the nanoparticles ($\theta = 0$), the induced field is *anti-parallel* to the incident field, and the collective resonance shifts *to the blue* 10 nm due to the *plus sign* in the denominator of the y-component in Eq. 6.10. If the incident field is polarized *parallel* to the vector connecting the nanoparticles ($\theta = \pi/2$), the induced field is *parallel* to the incident field, and the collective resonance shifts *to the red* 20 nm due the *minus sign* in the denominator of the x-component in Eq. 6.10. In addition, the factor of two in the denominator of the x-component means the red shift is larger than the respective blue shift, as illustrated in Fig. 6.2.

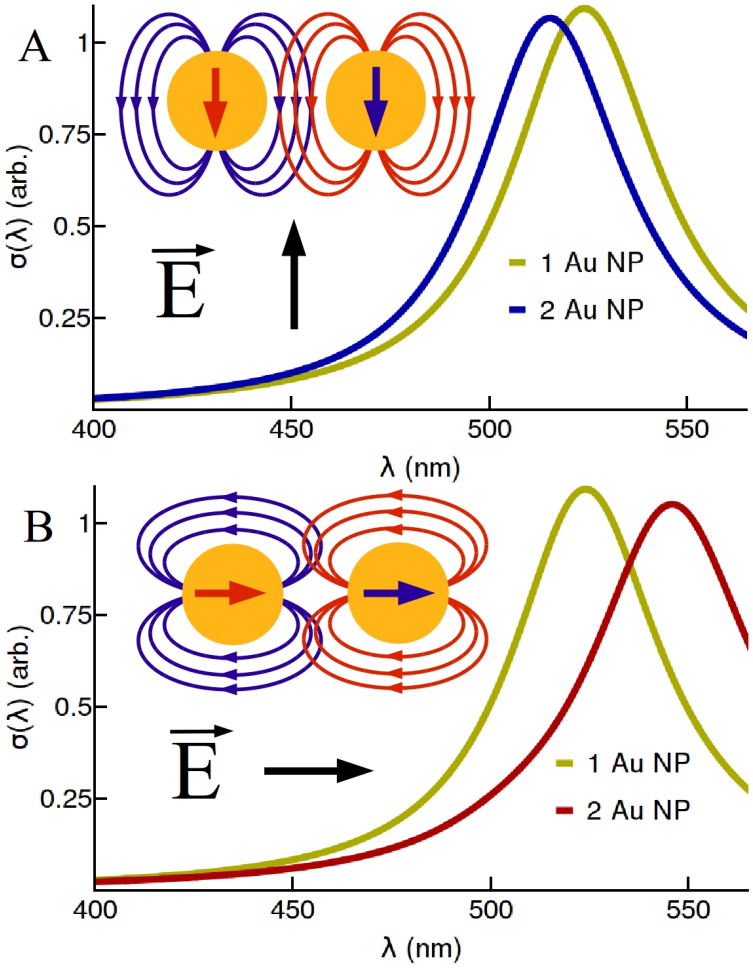

Figure 6.2: The dipolar Mie theory of Eqs. 6.5–6.6, illustrates the effect on the collective resonance when metal nanoparticles are in close proximity. If the incident field is polarized (A) *perpendicular* to the vector connecting the nanoparticles, the induced field is *anti-parallel* to the incident field, and the collective resonance shifts *to the blue*. If the incident field is polarized (B) *parallel* to the vector connecting the nanoparticles, the induced field is *parallel* to the incident field, and the collective resonance shifts *to the red*. The resonances also become broader due to the collective decay. This behavior has been measured experimentally in pairs of gold nanoparticles [97].

6.3 Collective Resonance: Ring of Nanoparticles

The results for two particles can easily be extended to a ring of nanoparticles as in Fig. 6.3, which we propose to use as an analogue of the light-harvesting antenna

in purple bacteria. In our proposed set-up, $N = 6$ gold nanoparticles are placed on a ring of radius 70 nm, so that the distance between nearest-neighbors on the ring is $r = 3a = 30$ nm and $kr = 30$ nm/524 nm $= 0.06 \ll 1$. The polarization of the light is chosen to be perpendicular to the plane of the ring such that $\vec{d}_j \cdot \vec{n}_{ji} = 0$, for reasons which will become clear when we consider the RC-LH1 analogue below. The dipole moments in such a configuration obey a very simple set of coupled equations, using the simplified induced fields of Eq. 6.7,

$$\vec{d}_i = \alpha\left(\vec{E}_{ext,i} - \sum_{j\neq i} \frac{\vec{d}_j}{r_{ji}^3}\right) \tag{6.12}$$

which can be written in the form

$$\hat{D} = \hat{E}_{ext} + \overleftrightarrow{E}_{ind}\hat{D} \tag{6.13}$$

$$\hat{D} = \left(\vec{d}_1, ..., \vec{d}_N\right) \tag{6.14}$$

$$\hat{E}_{ext} = \alpha\vec{E}_0\left(e^{i(kr_1-\omega t)}, ..., e^{i(kr_N-\omega t)}\right) \tag{6.15}$$

$$\overleftrightarrow{E}_{ind} = -\alpha\begin{pmatrix} 0 & \frac{1}{r_{12}^3} & \frac{1}{r_{13}^3} & \cdots \\ \frac{1}{r_{21}^3} & 0 & \frac{1}{r_{23}^3} & \\ \frac{1}{r_{31}^3} & \frac{1}{r_{32}^3} & 0 & \\ \vdots & & & \end{pmatrix}. \tag{6.16}$$

This inhomogeneous system of equations which can be solved using the standard methods

$$\hat{D} = (1 - \overleftrightarrow{E}_{ind})^{-1} \hat{E}_{ext} \tag{6.17}$$

$$(1 - \overleftrightarrow{E}_{ind})^{-1} = \overleftrightarrow{Q} \overleftrightarrow{\Lambda}^{-1} \overleftrightarrow{Q} \tag{6.18}$$

where $\overleftrightarrow{Q}$ diagonalizes $(1 - \overleftrightarrow{E}_{ind})$ and $\overleftrightarrow{\Lambda}^{-1}_{i,j} = \delta_{ij}/\lambda_i$, where λ_i is the ith eigenvalue. Considering the circular aggregate with nearest-neighbor couplings, the coupling matrix $\overleftrightarrow{E}_{ind}$ takes the form

$$\overleftrightarrow{E}_{ind} = -\frac{\alpha}{r^3} \begin{pmatrix} 0 & 1 & 0 & \dots & 1 \\ 1 & 0 & 1 & \dots & 0 \\ 0 & 1 & 0 & \dots & 0 \\ \vdots & \vdots & \vdots & & \vdots \\ 1 & 0 & 0 & \dots & 0 \end{pmatrix}. \tag{6.19}$$

The periodicity of $(1 - \overleftrightarrow{E}_{ind})$ means it can be diagonalized by a Fourier transform

$$\overleftrightarrow{Q}_{q,m} = \frac{1}{\sqrt{N}} e^{i\frac{2\pi}{N}qm} \tag{6.20}$$

$$\lambda_q = 1 + 2\frac{\alpha}{r^3} \cos\left(\frac{2\pi}{N} q\right). \tag{6.21}$$

We again assume that k r $\approx$ *constant* across the ring such that the field experienced by each dipole is the same, i.e. $\hat{E}_{ext} = \alpha \vec{E}_0 \, (1, ..., 1)$. Due to a selection rule for q = 0 (i.e. $\sum_m e^{i2\pi/Nqm} = N\delta_{q,0}$), a very simple expression exists for the dipole moments

on the ring

$$\vec{d_i} = \frac{\alpha}{1 + 2\frac{\alpha}{r^3}} \vec{E_0}, \tag{6.22}$$

where the factor of two in the denominator, as compared to Eq. 6.10 for $\theta = 0$, arises due to the two nearest-neighbors of each nanoparticle in the circular aggregate.

Derivation:

$$\begin{aligned}
\vec{d_m} &= (\overleftrightarrow{Q}\overleftrightarrow{\Lambda}^{-1}\overleftrightarrow{Q}\,\hat{E})_m \\
&= \sum_{n,q,r} \overleftrightarrow{Q}_{m,n} \overleftrightarrow{\Lambda}^{-1}_{n,q} \overleftrightarrow{Q}_{q,r} \hat{E}_r \\
&= \sum_{n,q,r} \overleftrightarrow{Q}_{m,n} \left(\frac{1}{\lambda_q}\delta_{n,q}\right) \overleftrightarrow{Q}_{q,r} \hat{E}_r \\
&= \alpha \vec{E}_0 \sum_q \frac{\overleftrightarrow{Q}_{m,q}}{\lambda_q} \sum_r \overleftrightarrow{Q}_{q,r} \\
&= \frac{\alpha \vec{E}_0}{N} \sum_q \frac{e^{i2\pi/Nmq}}{\lambda_q} \sum_r e^{i2\pi/Nqr} \\
&= \frac{\alpha \vec{E}_0}{N} \sum_q \frac{e^{i2\pi/Nmq}}{\lambda_q} N\delta_{q,0} \\
&= \frac{\alpha \vec{E}_0}{\lambda_0} = \frac{\alpha \vec{E}_0}{1 + 2\frac{\alpha}{r^3}}
\end{aligned} \tag{6.23}$$

Hence, the absorption of a ring is given by

$$\sigma(\omega) \propto \omega N |\vec{E}_0|^2 Im\left(\frac{\alpha}{1 + 2\frac{\alpha}{r^3}}\right). \tag{6.24}$$

The results are shown in Fig. 6.3. The most important feature is the blue shift of 20 nm, which is determined by the geometry of the set-up, i.e. through the value of $\alpha(\omega)/r^3$ in the denominator of Eq. 6.22.

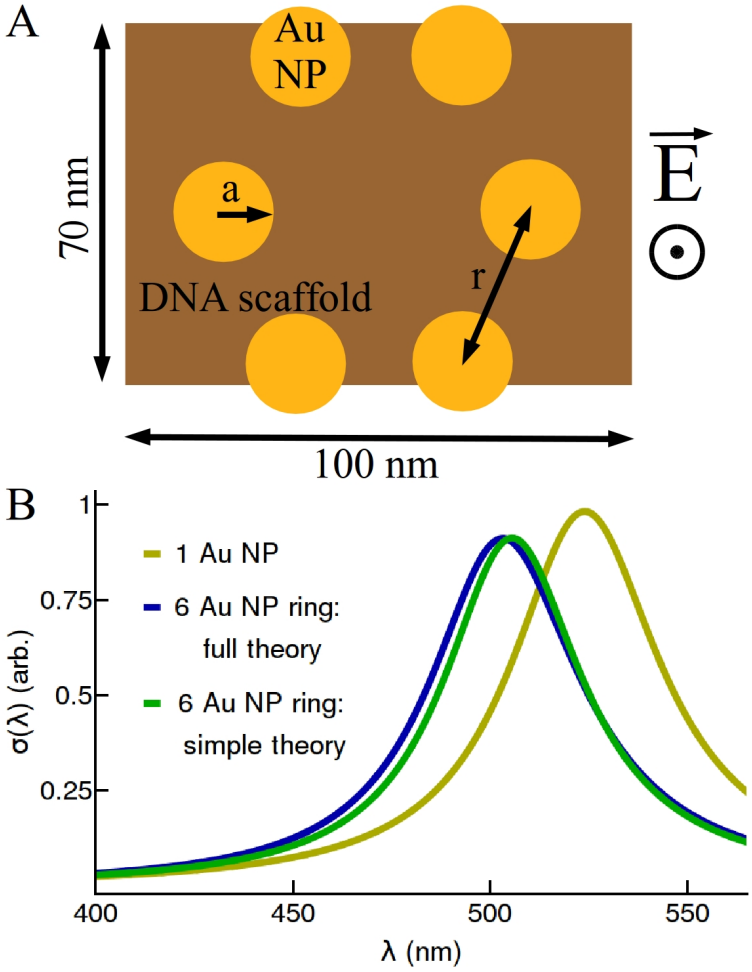

Figure 6.3: Six Au NP of radius 10 nm (A) anchored to a DNA scaffold of dimensions 70 nm $\times$ 100 nm is proposed as an analogue to the light-harvesting antenna in purple bacteria. Due to the dipolar fields induced by the applied field, with polarization perpendicular to the plane of the ring, the collective resonance of the system (B) is shifted 20 nm to the blue. The full theory, Eq. 6.6, includes retardation effects and the induced fields of all neighbors, while the simplified theory, Eq. 6.22, ignores retardation effects (kr = 0) and takes into account only nearest-neighbor interactions.

6.4 Collective Resonance: RC-LH1 Analogue

We can easily extend these results to an RC-LH1 analogue, where a silver (Ag) nanoparticle (with polarizability $\alpha'(\omega)$ and dielectric function $\epsilon'(\omega)$) is placed in the middle of the ring. The ring and RC nanoparticles have induced dipole moments

$$\vec{d}^{\,ring} = \sum_i \vec{d}_i^{\,ring} = \frac{N\alpha}{1+\frac{2\alpha}{r^3}}\vec{E}_0 - \frac{N\alpha}{r_{RC}^3}\vec{d}^{\,RC} \tag{6.25}$$

$$\vec{d}^{\,RC} = \alpha'\vec{E}_0 - \frac{\alpha'}{r_{RC}^3}\vec{d}^{\,ring} \tag{6.26}$$

where $r_{RC} = 30$ nm is the distance between the central RC Ag nanoparticle and the antenna Au nanoparticles. This system of equations is completely determined for $\vec{d}^{\,ring}$ and $\vec{d}^{RC}$ and can be solved again by simple substitution.

$$\vec{d}^{\,ring} = \frac{N\alpha}{1+\frac{2\alpha}{r^3}}\left(\frac{1-\frac{\alpha'}{r_{RC}^3}\left(1+\frac{2\alpha}{r^3}\right)}{1-\frac{N\alpha'\alpha}{r_{RC}^6}}\right)\vec{E}_0 \tag{6.27}$$

$$\vec{d}^{\,RC} = \alpha'\left(\frac{1-\frac{N\alpha}{r_{RC}^3}\frac{1}{1+\frac{2\alpha}{r^3}}}{1-\frac{N\alpha'\alpha}{r_{RC}^6}}\right)\vec{E}_0. \tag{6.28}$$

The absorption is calculated using the full and reduced models in Fig. 6.4. The system has been constructed in such a way that the collective resonance corresponding to absorption at the RC has increased by 60 %. This system also has the benefit that the antenna and RC-analogue bands are spectrally resolvable, which makes for an easy read-out and interpretation of the acquired spectra. The increase is limited here by the large energy gap between the resonances of commercially-available

gold and silver nanoparticle ($\sim$ 5000 cm^{-1}), and larger increases can be expected by tuning these resonances by modifying the particle size and/or composition. The proposed system represents the first step towards creating an artificial biomemetic nano-device which would direct absorption towards target pigments, where charge separation could take place, or photo-protection of fast-bleaching pigments.

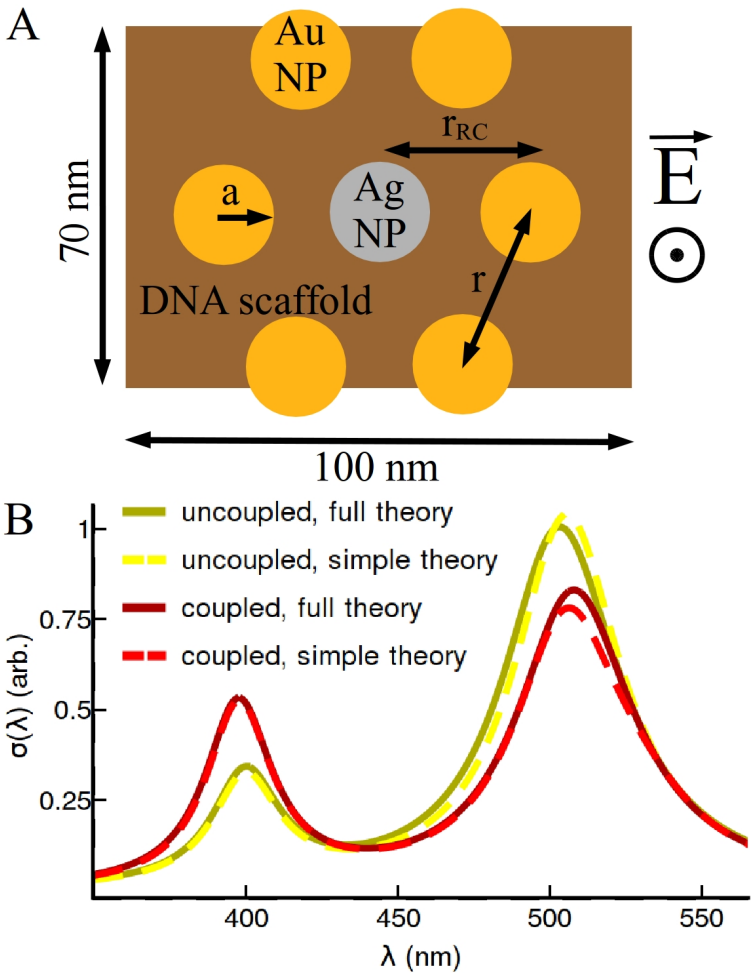

Figure 6.4: Six Au NP of radius 10 nm and a single Au NP or radius 10 nm (A) anchored to a DNA scaffold of dimensions 70 nm × 100 nm is proposed as an analogue to the RC-LH1 complex in purple bacteria. The collective resonances (B) of the coupled RC-LH1-analogue system are repelled with respect to the uncoupled, or isolated, antenna and RC. In addition, the absorption is directed in such a way that the RC-analogue absorbs 60% more light. The full theory, Eq. 6.6, includes retardation effects and the induced fields of all neighbors, while the simplified theory, Eq. 6.27-6.28, ignores retardation effects (kr = 0) and takes into account only nearest-neighbor interactions on the ring.

6.5 Effects of Polarization Angle

In the above discussion, the 2D assembly was assumed to lie in the x-y plane, and the light field to propogate in that plane with a polarization along the z-axis.

That is, the polarization of the light field is *perpendicular* to the vectors connecting the particles. The reason for this choice can be understood by the simple example quantified by Eqs. 6.10. There, and in Fig. 6.2, it is shown that such a configuration of particles and field leads to a *blue-shifted* absorption of the collective resonance. This is an advantageous set-up in the RC-LH1 analogue because (1) the collective Au resonance is then shifted closer to the higher-lying Ag resonance, increasing the redistribution of absorption and (2) the induced dipoles on the ring and the RC-analogue are parallel, leading to maximal coupling and an increase of the effect. Indeed, if the field is partially polarized in the x-y plane according to

$$\vec{E}_{ext,i} = E_0(\sin\theta\cos\phi\hat{x} + \sin\theta\sin\phi\hat{y} + \cos\theta\hat{z}), \tag{6.29}$$

the absorption redistribution to the Au band decreases with increasing θ, as shown in Fig. 6.5.

6.6 Outlook

In this chapter we have taken the first step towards exploiting the lessons learned in Ch. 2–5 about bacterial light-harvesting in order to create an artificial light-harvesting nano-device. Using techniques and tools common to today's laboratories – DNA origami and metal nanoparticles – we proposed an analogue to the RC-LH1 complex in purple bacteria which, according to our calculations, can redistribute absorption to a central target particle, increasing its direct absorption by 60 %. In any experimental realization, the yield of these nano-devices, in conjunc-

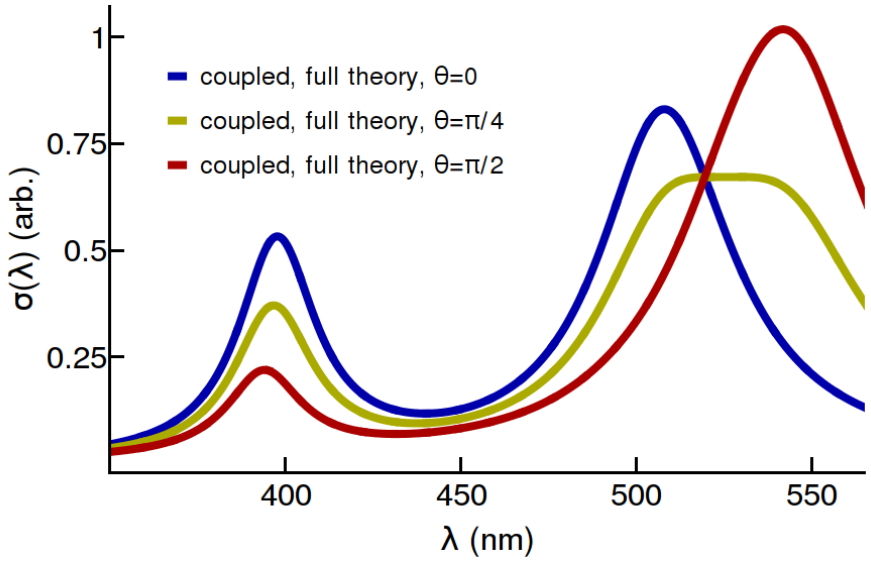

Figure 6.5: As the metal nanoparticles are polarizable, the polarization of the external field determines their induced fields. As shown in Fig. 6.2, the polarization angle can effect a red or blue shift of the collective resonance. The dipole strength redistribution depends on the resonance between the ring and RC analogue, hence it becomes smaller as the field polarization enters the plane of the ring, which shifts the ring resonance to the blue, further from the RC resonance.

tion with the polarization requirements for maximal redistribution, makes single-molecule experiments the most likely avenue to measure the effect. In this case, single-molecule fluorescence measurements, as opposed to absorption, will probably yield the best signal. Theoretically, the signatures of absorption redistribution in fluorescence measurements should be explored, as well as the effects of inhomogeneous broadening, as it is known that the homogeneous width is 25 THz, yet the full spectral linewidth is 50 THz. Next-generation experiments might replace the central target particle with a bacterial RC, and measure the effects of the collective ring resonance on absorption and charge separation. This set-up promises to be an exciting and realizable platform for exploring absorption redistribution, and its effects on subsequent transfer, in an artificial or hybrid system.

Chapter 7: Conclusions

This thesis was concerned with a description of absorption in natural and artificial light-harvesters. The coupling between light-harvesting units, although sometimes small compared to environmental couplings and dephasing rates, can lead to large, experimentally-accessible redistributions of absorption intensity between constituents. Here we recapitulate the main findings from Chapters 5-7.

In Chapter 5 we exploited the symmetry properties of light-harvesting antennae in purple bacteria to calculate theoretically the optical signatures of coupling between, and hence exciton delocalization across, the circular rings. The linear-dichroism (LD), a subtraction of orthogonally-polarized absorption spectra, is particularly sensitive to this coupling, which breaks the circular symmetry of excitons confined to a single ring. Analytical and numerical calculations show that the contrast of the LD can be directly related to the magnitude of the inter-ring coupling, which is responsible for the incoherent Förster energy transfer on the 1 - 10 ps timescale. Hence, our proposed experiment would allow an alternative, if indirect, measurement of the Förster rate using simple linear absorption measurements.

In Chapter 6 we showed, through experiment and theoretical calculations, that the short-lived exciton delocalization across the light-harvesting antennae and re-

action center in purple bacteria effects a redistribution of absorption intensity from the LH1 (B880 band) to the RC (P870 band) compared to the isolated spectra. Experimentally, dark-minus-light spectra circumvent the overwhelming contribution of the B880 band, which overlaps with the weaker P870 band and obscures the small (absolute) changes upon coherent coupling, and is consistent with a 90 % increase in direct absorption of the P870 band in the complete core complex. This redistribution of dipole strength leads directly to a redistribution of excitation population to the RC, leading to a small ($\sim$ 1 %) increase in the efficiency of charge separation at later times ($\sim$ 10-100 ps). Numerical calculations predict a similar excitation redistribution in other purple bacteria species and higher plants.

The high symmetry of the LH1-RC core complex allows analytical expressions for the redistribution of excitation, design principles which we exploited in Chapter 7 to propose an artificial light-harvesting device that funnels 60 % more excitation from an antenna to a spectrally-distinct RC-analogue. Although the system is composed of mesoscopic metal nanoparticles and hence can be described classically, the collective plasmon resonances exhibit the same phenomenology, and obey the same design principles, as the quantum system.

Many exciting avenues remain to be explored using the design principles illustrated in this thesis. Perhaps most exciting is the continuing possibility of constructing artificial light-harvesting systems that exploit the funnelling of excitation due to collective effects of the antenna and RC units. Using DNA origami as a scaffold and a hybrid toolbox– containing artificial elements like metal nanoparticles and quantum dots, as well as natural elements like pigment-protein complexes and

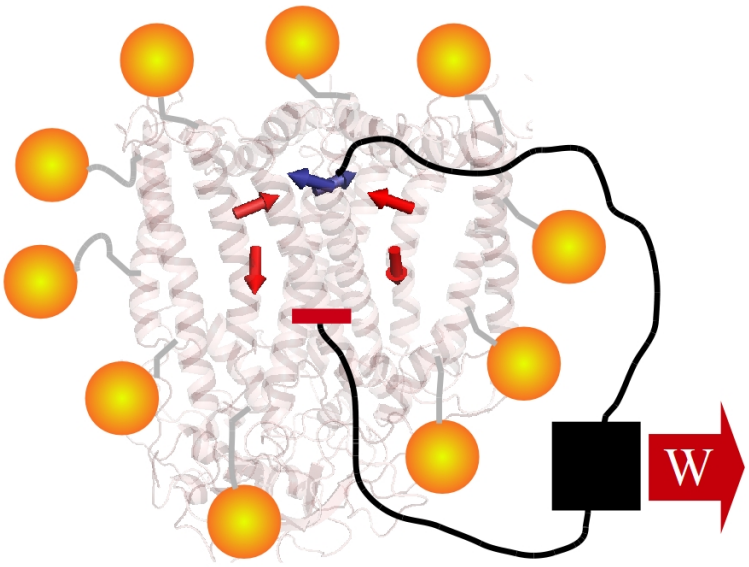

Figure 7.1: A hybrid device exploiting the design principles explored in this thesis, composed of metal nanoparticles mirroring the arrangment of BChl in the RC-LH1 complex around the bacterial RC, could funnel excitation to the charge separation unit. This could lead to large improvements in efficiency in noisy environments, where excitations are lost along a transfer pathway from the antenna to the RC.

cyanine dyes– the possibilities are limited only by functional chemistry and one's imagination. These design principles could increase the efficiency of an artificial light-harvester by funnelling excitations to the charge separation unit, thereby limiting the number of excitations which must be transferred across the device, along which they may be lost due to heating. Increases in efficiency are most dramatic in low-light conditions, where the intelligent use of every photon is required. A speculative hybrid device exploiting these principles, in which metal nanoparticles or cyanine dyes are functionalized on a bacterial reaction center to funnel absorption to the special pair, is illustrated in Fig. 7.1. In addition, extension of these results to spectral regions outside the visible, such as the microwave, could have implications for wireless communication and charging.

Appendix A: Measuring Dark-Minus-Light Spectrum in RC-LH1 Core Complex: Experiment Details

Methods for Determination of the RC-P870 Contribution After Oxidation of the Intact, Membrane-Embedded PSU with Stoichiometric Amounts of $K_3Fe(CN)_6$

Diagnostic Features of the RC Redox Spectrum

It is now well-accepted that the oxidation of the purified RC with small amounts of a strong oxidizing agent, such as $K_3Fe(CN)_6$, leads to spectral changes in the near-IR region which correspond perfectly to those observed after photobleaching with actinic light. A typical example, obtained by the $K_3Fe(CN)_6$-induced oxidation of the purified RC (in detergent solution) from *R. rubrum* is shown in Fig. 8.1 (A). Under these conditions of oxidation the P870 band is essentially abolished, and the 803 nm peak, corresponding to the accessory BChl is slightly increased in intensity and blue-shifted. It has been shown previously [58] that the absorption transitions contributing to P870 are in fact split upon oxidation to P870+, with one component being shifted to about 800 nm (hence the observed changes to the 803 nm peak) and the other to 1260 nm (which is not visible with our instrumentation). For diagnostic purposes with real biological preparations, the redox difference (reduced RC

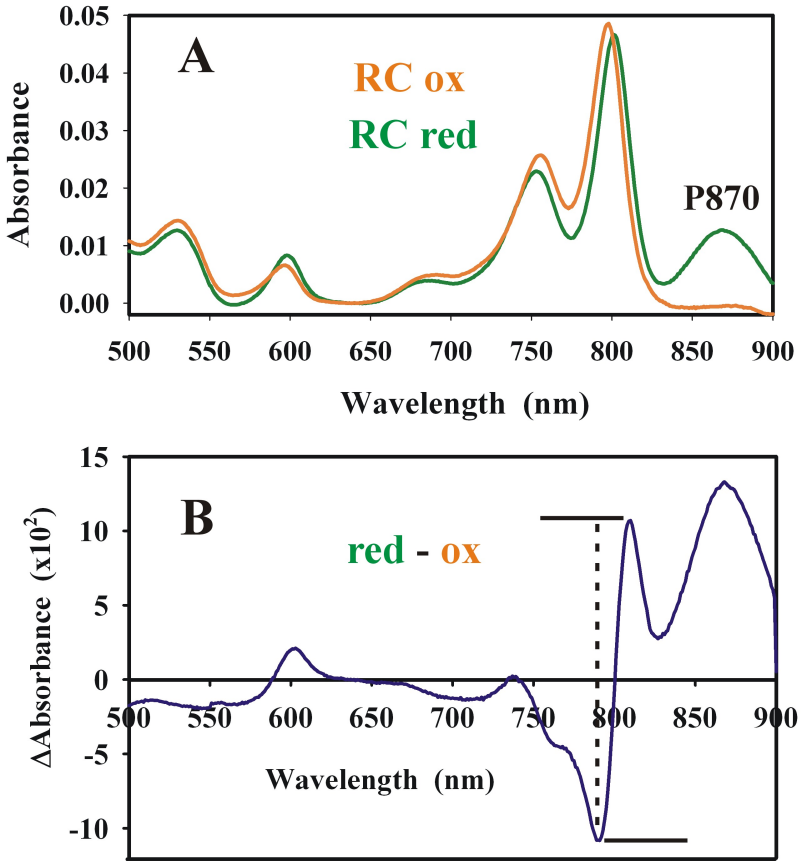

Figure 8.1: (A) Absorption spectra of reduced and oxidized RC, respectively. The position of the special pair (P870, Gaussian fit: λ_{max} = 869 nm, σ = 19.6 nm) is indicated. (B) Redox (reduced RC - oxidized RC) difference spectrum. The position and intensity of the 803 nm crossover, used as a reference point for fitting, is indicated.

- oxidized RC) spectrum (Fig. 8.1 (B)) is a more reliable indicator of RC activity, since any contributions due to inactive RC are cancelled out.

A very useful feature of the RC redox spectrum is the crossover point and relative intensities of the flanking regions (indicated by a dotted line in Fig. 8.1 (B)) at the 803 nm region. *This feature is uniquely due to RC oxidation*, and is not observed from isolated LH1s subject to oxidation. In a complex mixture, therefore, this feature can be used as a diagnostic feature to distinguish RC and LH1 contributions, respectively.

Measurement Conditions for Obtaining Spectra of Purified RCs and Chro-

matophores

Chromatophores (intracytoplasmic membranes containing the PSUs and reaction centers) were isolated from anaerobic, phototrophic cultures of *R. rubrum* S1 as described [98–100]. Absorbance spectra of 500 μl samples (chromatophores: diluted in 20 mM TrisHCl, pH 8.0 (20T8)) were usually measured at room temperature in 2 mm path-length cuvettes with a Jasco V-560 UV/VIS spectrophotometer equipped with a near-IR-sensitive photodiode detector for turbid samples (slit width 2 nm, scanning speed 200 nm/min, photomultiplier response *fast*). Purified RCs (purifed by a slightly modified method of Vadebonceur *et al.* [100], were diluted in 20 mM TrisHCl, pH 7.7 containing 50 mM NaCl and 0.05 % (w/v) dodecyl-β-D-maltoside, prior to measurement. For routine chemical oxidation of isolated RCs (A870 (2 mm path-length) = 0.016), a few grains of potassium ferricyanide ($K_3Fe(CN)_6$) were added directly to the cuvette prior to measurement.

Determination of the RC Concentration from a Spectrum Obtained from Total Chromatophores

A precise determination of the RC concentrations is an essential prerequisite for stoichiometric oxidation. In principle, the RC concentration in total *R. rubrum* chromatophores might be determined from the 803 nm peak, which is exclusively due to the RC-accessory BChl. Unfortunately, the 881 nm peak of the LH1 exhibits significant intensity in the flanking region at 803 nm (see Fig. 8.2), which makes the assignment of the baseline solely due to the RC 803 nm peak difficult. To solve this problem unambigously, we compared the spectrum from the wild-type (LH1+RC) with that of a RC-minus mutant, SKΔLM, where the L- and M subunits of the

RC have been deleted (described in Ref. [101]). We have previously shown that the absorption spectra and also ultrafast transfer times for energy transfer amongst BChl and carotenoid pigments of the LH1 of the mutant are unchanged when compared with those of the wild-type LH1 [101]. We then fitted the SKΔLM spectrum to the wild-type spectrum, using the criterium that the right flanking region, between 882 - 900 nm, is due solely to the contribution from the LH1. This fit (see Fig. 8.2, expanded insert) enabled us to set a reference point for the position of the RC baseline. We note that the SKΔLM fitted spectrum now corresponded perfectly to the position of the LH1 Q_x band at 589 nm (data not shown). This calculation showed that for the LH1+RC chromatophores, about 48% of the intensity at 803 nm arises from the RC accessory BChl. Using the millimolar extinction coefficient of $\epsilon(803\text{ nm}) = 329\text{ mM}^{-1}.\text{cm}^{-1}$ [100], we calculated that 243 nmol RC are present in the cuvette under the conditions used.

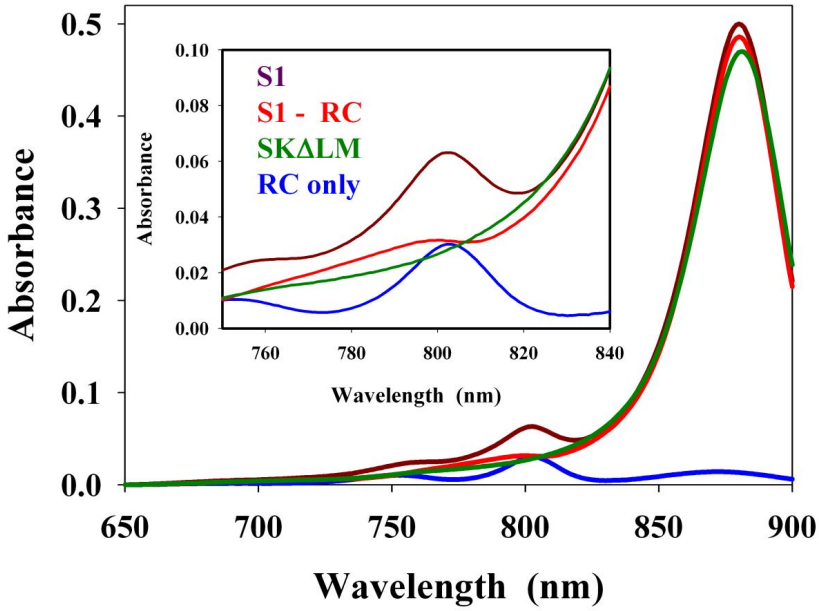

Figure 8.2: Absorption spectra used for the determination of the RC content. The effective RC baseline was determined from the difference in intensity at 803 nm from spectra of isolated chromatophores from the wild-type S1 (LH1 + RC, brown line) and a RC- mutant SKΔLM (LH1 only, green line). The calculated RC spectrum (using the spectrum obtained from purified RC (see Fig. S7A) is shown in blue. The spectrum shown in red corresponds to the (LH1+RC) chromatophores *minus* the calculated, purified RC spectrum.

Stoichiometric Oxidation of the RC with $K_3Fe(CN)_6$

For a precise titration of the RC special pair redox state in chromatophores (A881 (2 mm path-length) = 0.37), incremental amounts of $K_3Fe(CN)_6$ (0 - 560 nmol (stock solution 20 mM $K_3Fe(CN)_6$ solution (in H_2O))) were added to a chromatophore suspension, containing approximately 243 nmol RC, as calculated from the extinction at 803 nm. Generally, the chromatophores were incubated with redox agent at 25°C for 5 min prior to measurement in the Jasco spectrophotometer, as described above. Prior to quantitative analysis, the spectra were normalized to the baseline intensity at 640 nm, where no absorption due to pigment occurs.

The results of a typical redox titration are shown in Fig. 8.3 (A). We observed, that *even at stoichiometric levels of $K_3Fe(CN)_6$ to RC*, that the 882 nm peak due to the LH1 Q_y absorption maximum is also reduced (note that this bleaching corresponds to *chemical oxidation* of the LH1 BChl), and this reduction is concomitant with that of the special pair oxidation. To our knowledge, this is the first time that the effects of stoichiometric oxidation upon the LH1 complex have been reported.

To proceed further, we made the initial assumption, that at higher, but still near stoichiometric quantities of $K_3Fe(CN)_6$, the oxidation of the LH1 BChls (measured as the reduction of peak height at 881 nm) should be linear, whereas that of the RC (measured at 803 nm) should be constant. This can be most easily visualized by calculating the difference spectrum (A881 (0 mM $K_3Fe(CN)_6$) - A881 (x mM $K_3Fe(CN)_6$) = (ΔAbs881)). The spectral results, shown in Fig. 8.3 (B), confirm our hypothesis: above about 240 nmol $K_3Fe(CN)_6$, no further change in the 803 nm peak is observed with increasing oxidizing agent, but the A881 nm peak is incrementally reduced further. The inset in Fig. 8.3 (B) also shows that no spurious effects to turbidity changes arise during this process. Quantitative analysis of these data (Fig. 8.4 (A) and (B)) confirm the linearity of LH1 oxidation at $K_3Fe(CN)_6$ levels where the RC is completely oxidized (Fig. 8.4 (A)). The usable range for further analysis, where the RC oxidation is constant (Fig. 8.4 (B)) was shown to be between 400 - 560 nmol $K_3Fe(CN)_6$.

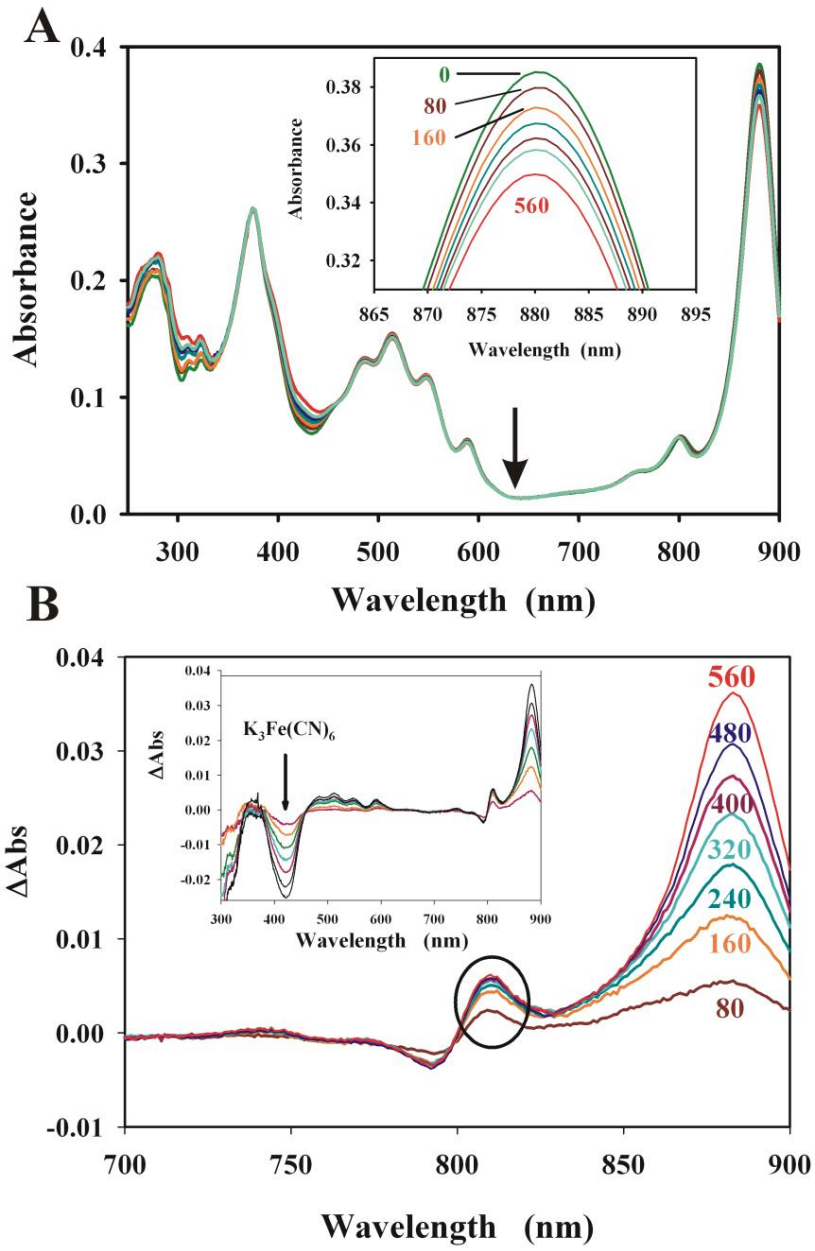

Figure 8.3: Reduction of the near-IR (LH1+RC) peak intensity following stoichiometric additions of $K_3Fe(CN)_6$. (A) The primary spectral data, obtained from chromatophores equilibrated with different concentrations of $K_3Fe(CN)_6$ (given in nmoles). The initial data set was normalized to the intensity at 640 nm, where no absorption due to pigment occurs. Inset: enlarged near-IR region of the spectrum. (B) First near-IR difference spectra (ΔAbs), obtained from the data shown in (A). Each spectrum corresponds to the difference between the spectrum obtained at a given amount of $K_3Fe(CN)_6$ (indicated) minus the reference spectrum (taken in the absence of $K_3Fe(CN)_6$). Inset: the spectral difference obtained over the complete range. Note that the absorption change due to $K_3Fe(CN)_6$ is easily visible (arrow), and can be used for control purposes.

Thus, the LH1 spectral contribution present in the spectra obtained from oxidized LH1+RC chromatophores should be obtainable by subtracting pairs of difference spectra (ΔAbs) obtained for $K_3Fe(CN)_6$ amounts between 400-560 nmol. In principle, any of the pairs might be employed for this purpose, but we have found it convenient to obtain a series of difference-difference spectra by subtracting sequental pairs (i.e. ΔAbs320-ΔAbs400, ΔAbs400-ΔAbs480, ΔAbs480-ΔAbs560). With this series in hand (Fig. 8.5 (A)), we need to perform one final control to prove that each member of this series corresponds to the same spectral form. This is done by a simple transformation. First, each (now noisy) ΔΔAbs spectrum is normalized to the same maximal intensity (Fig. 8.5 (B)). If the normalized spectra correspond to the same spectral form, then a plot of ΔΔAbs values for each pair should fall upon the same straight line. Fig. 8.5 (C) shows that this expectation is fulfilled. Therefore, we can now employ the parameters of the derived LH1 spectral difference for determining the contribution in the redox spectrum obtained from the lowest amounts of $K_3Fe(CN)_6$, where the contribution from RC and LH1, respectively are comparable.

The final deconvolution was performed as follows. We chose to use the primary difference spectrum ΔAbs(160) for the analysis, since visual inspection suggested significant spectral contributions from both LH1 and RC to be present. Initially, the secondary difference spectrum ΔΔAbs(560-480 nmol) (see Fig. 8.5 (A)) was fitted to the spectrum ΔAbs(160), using the constraint that the least-squares difference *at the far red flank* (which arises almost exclusively due to the LH1 component) must be minimized. The result, ΔAbs(160) - ΔΔAbs(560-480 nmol), is shown in green

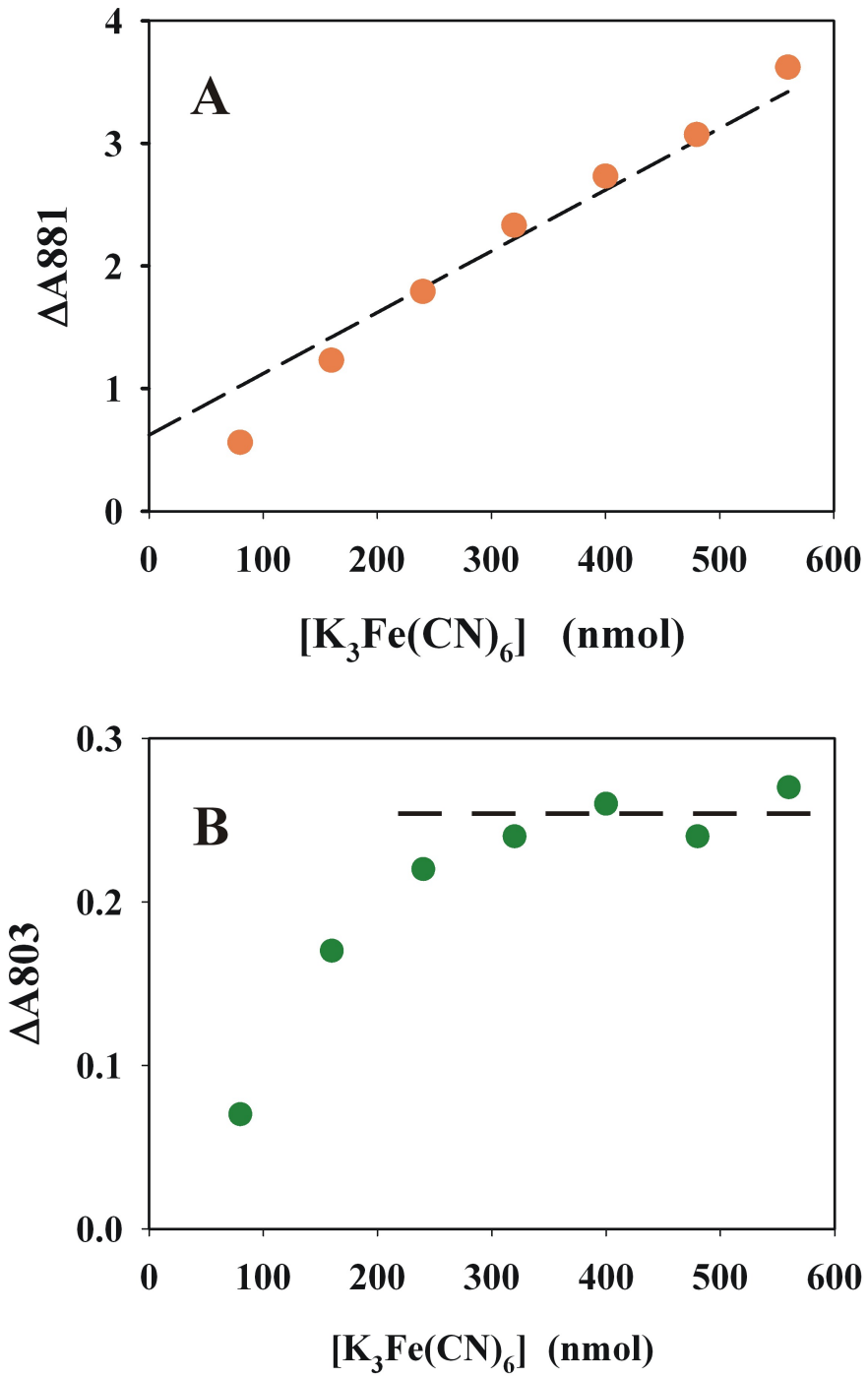

Figure 8.4: Variation of the peak amplitudes of the peak intensities at 881 nm (A) and 803 nm (B) respectively, obtained from the difference spectra shown in Fig. 8.3 (B). In (A) the dashed line was determined by linear regression, using the last four points (320 - 560 nmol) as input data. However, inclusion of the data point at 240 nmol had almost no effect upon the regression curve. Note that the intensities shown have been re-scaled for presentation clarity.

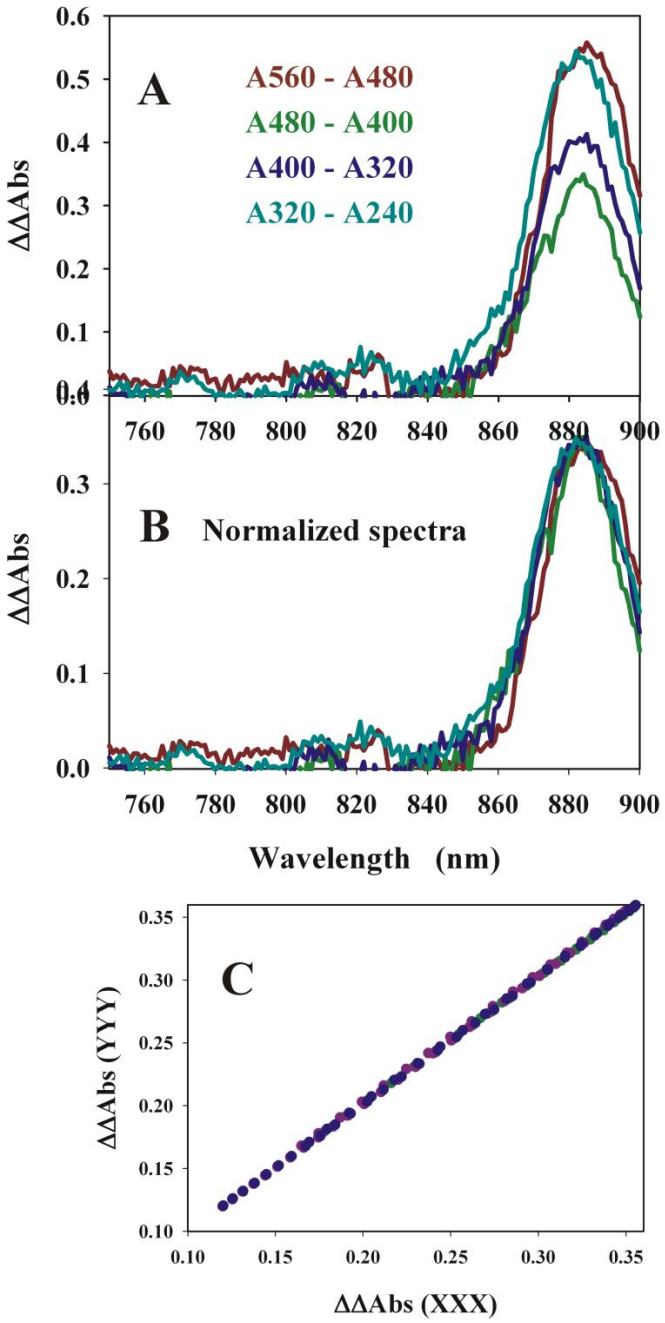

Figure 8.5: (A) The secondary difference spectra, obtained from the data shown in Fig. 8.3 (B). Each spectrum corresponds to the difference taken from two sequential pairs e.g. ΔΔAbs(A560-480) = ΔAbs(560) - ΔAbs(480). (B) The difference spectra in (A) normalized to the same intensity value at 881 nm. (C) Correlation plot of the ΔΔAbs intensities from sequential spectral pairs (e.g. ΔΔAbs(560-480) *vs.* ΔΔAbs(480-400)). The intensities shown have been re-scaled (x 10^2) for presentation clarity. Only the intensity range corresponding to the wavelength range 800 - 900 nm has been plotted.

in Fig. 8.6 (A) and (B), and the fitted LH1 component is shown as a dashed cyan line in Fig. 8.6 (A). Also shown is a Gaussian fit (λ_{max} = 868 nm, σ= 19.6 nm) to the "P870" peak of the final spectrum, which is thus 1 nm blue-shifted compared to that obtained for the purified RC in solution (shown as the orange dashed line in Fig. 8.6 (B)). In Fig. 8.6 (A), another secondary difference spectral component ($\Delta\Delta$Abs(320-240 nmol) is also shown (brown dashed line)). The same fitting as above, repeated using this latter spectral component, led to an identical result (not shown). In the main text, the spectrum shown in Fig. 5.1 (D) has been calculated using the difference ΔAbs(160)-$\Delta\Delta$Abs(320-160 nmol). The final result however, is essentially identical to that shown in Fig. 8.5 (A)–(B).

Methods for core complex photobleaching

The measurement of RC photobleaching was performed by comparing the "dark" spectrum obtained from total chromatophores (A881 (2 mm path-length) = 1.06) to that obtained during illumination with actinic light (using a 150 W halogen lamp). The actinic light was filtered through 3 cm of a 1 M $CuSO_4$ solution. The amount of light quanta reaching the cuvette during illumination in this experiment was 40 nmol $cm^{-2}.s^{-1}$ (or 14000 Lux). In the dark-light experiments, the internal photomultiplier of the Jasco spectrophotometer was used instead of the photodiode, because it could be protected more easily from any stray actinic light by a long-pass filter (Asahi, XVL 0610, 1.5 mm) and a self-built chamber of black cardboard. To improve the signal-to-noise-ratio, the scanning speed was reduced to 100 nm/min, and the response was set to *slow*. In this experiment, the contribution to LH1 fluorescence was negligible. This was confirmed by performing control experiments using an

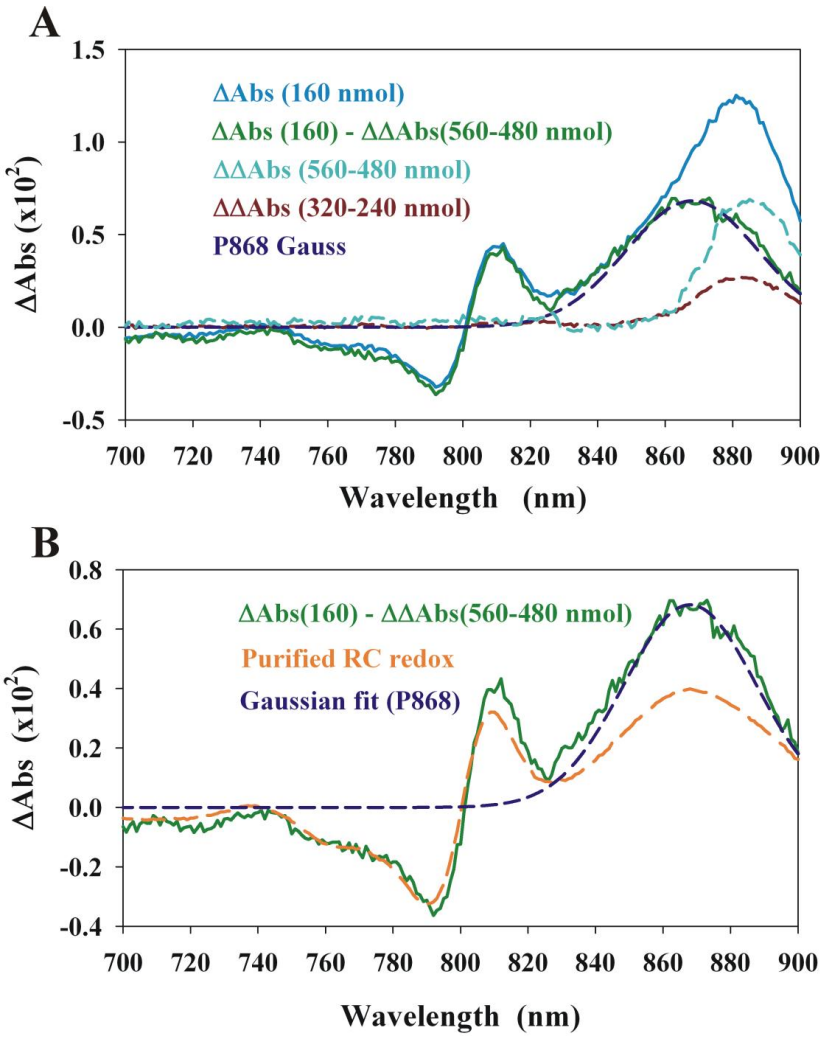

Figure 8.6: Deconvolution of the primary difference (ΔAbs) spectra into LH1 and RC components. (A) The primary difference spectrum ΔAbs(160) (blue line), obtained at 160 nmol $K_3Fe(CN)_6$, which contains about equal intensities from both LH1 and RC, was used for analysis. The fitting procedure was performed using the secondary difference spectrum ΔΔAbs(560-480 nmol) (see Fig. S11A) (see section SI (E) for details). The result, ΔAbs(160) - ΔΔAbs(560-480 nmol), is shown in green in (A) and (B), the fitted LH1 component (dashed cyan line in (A)), and a Gaussian fit (λ_{max} = 868 nm, σ = 19.6 nm, dark blue dashed line) to the "P870" peak of the final spectrum, which is thus 1 nm blue-shifted compared to that obtained for the purified RC in solution (shown as the orange dashed line in (B)), are also shown. In (A), another secondary difference spectral component (ΔΔAbs(320-240 nmol)) is also shown (brown dashed line). The same fitting as above, repeated using another secondary difference spectral component (ΔΔAbs(320-240 nmol), brown dashed line) led to an identical result (not shown). Note that the intensities shown have been re-scaled (x 10^2) for presentation clarity.

Avantes diode array spectrophotometer, where the intensity of the measuring beam was sufficient to induce measurable LH1 fluorescence.

Bibliography

[1] N. Lambert, Y. N. Chen, Y. C. Cheng, C. M. Li, G. Y. Chen, and F. Nori. Quantum biology. *Nature Phys.*, 9:10–18, 2013.

[2] S. F. Huelga and M. B. Plenio. Vibrations, quanta and biology. *Contemporary Physics*, 54:181–207, 2013.

[3] G. Engel, T. Calhoun, E. Read, T. Ahn, T. Mancal, Y Cheng, R. Blankenship, and G. Fleming. Evidence for wavelike energy transfer through quantum coherence in photosynthetic systems. *Nature*, 446:782–786, 2007.

[4] E. Collini, C. Y. Wong, K. E. Wilk, P. M. G. Curmi, P. Brumer, and G. D. Scholes. Coherently wired light-harvesting in photosynthetic marine algae at ambient temperature. *Nature*, 463:644–647, 2010.

[5] G. Panitchayangkoon, D. Hayes, K. A. Fransted, J. R. Caram, E. Harel, J. Wen, R. E. Blankenship, and G. S. Engel. Long-lived quantum coherence in photosynthetic complexes at physiological temperature. *Proc. Natl. Acad. Sci. USA*, 107:12766–12770, 2010.

[6] R. Hildner, D. Brinks, J. B. Nieder, R. J. Cogdell, and N. F. Van Hulst. Quantum coherent energy transfer over varying pathways in single light-harvesting complexes. *Science*, 340:1448–1451, 2013.

[7] E. Romero, R. Augulis, V. I. Novoderezhkin, M. Ferretti, J. Thieme, D. Zigmantas, and R. van Grondelle. Quantum coherence in photosynthesis for efficient solar-energy conversion. *Nature Phys.*, 10:676–682, 2014.

[8] F. D. Fuller, J. Pan, A. Gelzinis, V. Butkus, S. S. Senlik, D. E. Wilcox, C. F. Yocum, L. Valkunas, D. Abramavicius, and J. P. Ogilvie. Vibronic coherence in oxygenic photosynthesis. *Nat. Chem.*, 6:706–711, 2014.

[9] V. Tiwari, W. K. Peters, and D. M. Jonas. Electronic resonance with anticorrelated pigment vibrations drives photosynthetic energy transfer outside the adiabatic framework. *PNAS*, 110:1203–1208, 2013.

[10] M. B. Plenio, J. Almeida, and S. F. Huelga. Origin of long-lived oscillations in 2d-spectra of a quantum vibronic model: electronic versus vibrational coherence. *J. Chem. Phys.*, 139:235102, 2013.

[11] F. Caycedo-Soler, A. W. Chin, J. Almeida, S. F. Huelga, and M. B. Plenio. The nature of the low-energy band of the Fenna-Matthews-Olson complex: vibronic signatures. *J. Chem. Phys.*, 136:155102, 2012.

[12] N. Christensson, H. F. Kauffmann, T. Pullerits, and T. Mančal. Origin of long-lived coherences in light-harvesting complexes. *J. Phys. Chem. B*, 116:7449–7454, 2012.

[13] M. Mohseni, P. Rebentrost, S. Lloyd, and A. Aspuru-Guzik. Environment-assisted quantum walks in photosynthetic energy transfer. *J. Chem. Phys.*, 129:174106, 2008.

[14] M. B. Plenio and S. F. Huelga. Dephasing assisted transport: quantum networks and biomolecules. *New J. Phys.*, 10:113019, 2008.

[15] A. Kolli, E. J. O'Reilly, G. D. Scholes, and A. Olaya-Castro. The fundamental role of quantized vibrations in coherent light-harvesting by cryptophyte algae. *J. Chem. Phys.*, 137:174109, 2012.

[16] A. W. Chin, J. Prior, R. Rosenbach, F. Caycedo-Soler, S. F. Huelga, and M. B. Plenio. The role of non-equilibrium vibrational structures in electronic coherence and recoherence in pigment protein complexes. *Nature Phys.*, 9:113–118, 2013.

[17] A. Chin, A. Datta, F. Carusso, S. F. Huelga, and M. B. Plenio. Noise-assisted energy transfer in quantum networks and light-harvesting complexes. *New. J. Physics*, 12:065002, 2010.

[18] J.M. Womick and A.M. Moran. Vibronic enhancement of exciton sizes and energy transport in photosynthetic complexes. *J. Phys. Chem. B*, 115:1347–1356, 2011.

[19] J. Lim, D. Palaek, F. Caycedo-Soler, C. N. Lincoln, J. Prior, H. von Berlepsch, S. F. Huelga, M. B. Plenio, D. Zigmantas, and J. Hauer. Vibronic origin of long-lived coherence in an artificial molecular light-harvester. *Nat. Commun.*, 6:1–7, 2015.

[20] J. Strumpfer and K. Schulten. Excited state dynamics in photosynthetic reaction center and light harvesting complex 1. *J. Chem. Phys.*, 137:065101, 2012.

[21] Ilia A. Solov'yov, Po-Yao Chang, and Klaus Schulten. Vibrationally assisted electron transfer mechanism of olfaction: myth or reality? *Phys. Chem. Chem. Phys.*, 14:13861–13871, 2012.

[22] M. I. Franco, L. Turin, A. Mershin, and E. M. C. Skoulakis. Molecular vibration-sensing component in *Drosophila melanogaster* olfaction. *Proc. Natl. Acad. Sci. USA*, 108:3797–3802, 2011.

[23] K. Maeda, K. B. Henbest, F. Cintolesi, I. Kuprov, C. T. Rodgers, P. A. Liddell, D. Gust, C. R. Timmel, and P. J. Hore. Chemical compass model of avian magnetoreception. *Nature*, 453:387–390, 2008.

[24] C. .T. Rodgers and P. J. Hore. Chemical magnetoreception in birds: The radical pair mechanism. *Proc. Natl. Acad. Sci. USA*, 106:353–360, 2009.

[25] J. Cai and M. B. Plenio. Chemical compass model for avian magnetoreception as a quantum coherent device. *Phys. Rev. Lett.*, 111:230503, Dec 2013.

[26] C. .A. Schroeder, F. Caycedo-Soler, S. F. Huelga, and M. B. Plenio. Optical Signatures of Quantum Delocalization over Extended Domains in Photosynthetic Membranes. *J. Phys. Chem. A*, 0(0):null, 0. PMID: 26256512.

[27] F. Caycedo-Soler, C. A. Schroeder, C. Autenrieth, R. Ghosh, S. F. Huelga, and M. B. Plenio. Quantum delocalization directs antenna absorption to photosynthetic reaction centres. submitted, 2015.

[28] X. Hu, T. Ritz, A. Damjanović, F. Autenrieth, and K. Schulten. Photosynthetic apparatus of purple bacteria. *Q. Rev. Biophys.*, 35:1–62, 2002.

[29] D. Dolphin, editor. *The Porphyrins, Vol. 3: Physical Chemistry, Part A*. Academic Press, 1978.

[30] W. T. Simpson. On the theory of the π-electron system in porphyrins. *J. Chem. Phys.*, 17:1218–1221, 1949.

[31] M. Gouterman. Spectra of porphyrins. *J. Mol. Spectrosc.*, 6:138–163, 1961.

[32] R. Gale, A. J. McCaffery, and M. D. Rowe. Magnetic circular dichroism and absorption spectra of the porphyrins. part i. *J. Chem. Soc., Dalton Trans.*, pages 596–604, 1972.

[33] C. Weiss, Jr. The Pi electron structure and absorption spectra of chlorophylls in solution. *J. Mol. Spectrosc.*, 44:37–80, 1972.

[34] C. Weiss, Jr., H. Kobayashi, and M. Gouterman. Part III. Self-consistent molecular orbital calculations of porphyrin and related ring systems. *J. Mol. Spectrosc.*, 16:415–450, 1965.

[35] Wikimedia Commons. LH2 BCh Absorption. *http* : *//commons.wikimedia.org/wiki/File* : $LH2_BCh_Absorption.png$, 09-06-2015. File: LH2 BCh Absorption.png.

[36] F. Autenrieth. The photosynthetic apparatus of *Rhodospirillum rubrum*: a computational approach . Diploma thesis, University of Stuttgart, 2002.

[37] S. Karrasch, P. A. Bullough, and R. Ghosh. The 8.5 Å. projection map of the light harvesting complex I from *Rhodospirillum rubrum* reveals a ring composed of 16 subunits. *EMBO Journal*, 14:631, 1995.

[38] S. J. Jamieson, P. Wang, P. Qian, J. Y. Kirkland, M. J. Conroy, C. N. Hunter, and P. Bullough. Projection structure of the photosynthetic reaction centre-antenna complex of *Rhodospirillum rubrum* at 8.5 Å resolution. *EMBO J.*, 21:3927–3935, 2002.

[39] J. Koepke, X. Hu, C. Muenke, K. Schulten, and H. Michael. The crystal structure of the light-harvesting complex II (B800-850) from *Rhodospirillum molischianum*. *Structure*, 4:581–597, 1996.

[40] G. McDermott, S. M. Prince, A. A. Freer, A. M. Hawthornthwaite-Lawless, M. Z. Papiz, and R. J. Codgell. Crystal structure of an integral membrane light-harvesting complex from photosynthetic bacteria. *Nature*, 374:517–521, 1995.

[41] X. Hu and K. Schulten. Model for the Light-Harvesting Complex I (B875) of Rhodobacter sphaeroides. *Biophys. J.*, 75:683–694, 1998.

[42] U. Gerken, F. Jelezko, B. Götze, M. Branschädel, C. Tietz, R. Ghosh, and J . Wrachtrup. Membrane environment reduces the accessible conformational space available to an integral membrane protein. *J. Phys. Chem. B*, 107:338–343, 2003.

[43] U. Gerken, D. Lupo, C. Tietz, J Wrachtrup, and R. Ghosh. Circular symmetry of the light-harvesting 1 complex from *r*hodospirillum rubrum is not perturbed by interaction with the reaction center. *Biochemistry*, 42:10354–10360, 2003.

[44] A. Aird, J. Wrachtrup, K. Schulten, and C. Tietz. Possible pathway for ubiquinone shuttling in *Rhodospirillum rubrum* revealed by molecular dynamics simulation. *Biophys. J.*, 92:23–33, 2007.

[45] S. Scheuring, F. Reiss-Husson, A. Engel, Jean-Louis Rigaud, and Jean-Luc Ranck. High-resolution AFM topography of *Rubrivax gelatinosus* light-harvesting complex LH2. *EMBO J.*, 20:3029–3035, 2001.

[46] S. Niwa, L. J. Yu, K. Takeda, Y. Hirano, T. Kawakami, Z. Y. Wang-Otomo, and K. Miki. Structure of the LH1-RC complex from *Thermochromatium tepidum* at 3.0 Å. *Nature*, 508:228–232, 2014.

[47] Robin Ghosh, Helmut Hauser, and Reinhard Bachofen. Reversible dissociation of the B873 light-harvesting complex from *R*hodospirillum rubrum G9+. *Biochemistry*, 27:1004–1014, 1988.

[48] H. J. Carmichael. *An open systems approach to quantum optics*. Springer-Verlag, 1993.

[49] R. Jimenez, F. van Mourik, J. Y. Yu, and G. R. Fleming. Three-pulse photon echo measurements on LH1 and LH2 complexes of *Rhodobacter sphaeroides*: A nonlinear spectroscopic probe of energy transfer. *J. Phys. Chem. B*, 101:7350–7359, 1997.

[50] K. Timpmann, G. Trinkunas, P. Qian, and C. N. Hunter. Excitons in core LH1 antenna complexes of photosynthetic bacteria: evidence for strong resonant coupling and off-diagonal disorder. *Chem. Phys. Lett.*, 414:359–363, 2005.

[51] A.S. Davydov. The theory of molecular excitons. *Usp. Fiz. Nauk*, 82:393–448, 1964.

[52] F. Caycedo-Soler, F. J. Rodríguez, L. Quiroga, and N. F. Johnson. Light-Harvesting mechanism of bacteria exploits a critical interplay between the dynamics of transport and trapping. *Phys. Rev. Lett.*, 104:15832, 2010.

[53] S. Scheuring and J. Sturgis. Chromatic adaptation of purple bacteria. *Science*, 309:484, 2005.

[54] S. Scheuring, J. Busselez, and D. Levy. Structure of the dimeric PufX-containing core complex of *Rhodobacter sphaeroides*. *Journal of Biological Chemistry*, 279:3620, 2005.

[55] T. Walz and R. Ghosh. Two-dimensional crystallization of the light-harvesting I- reaction centre photounit from *Rhodospirillum rubrum*. *J. Mol. Biol.*, 265:107–111, 1997.

[56] S. Jang, M.D. Newton, and R.J. Silbey. Multichromophoric Förster resonance energy transfer. *Phys. Rev. Lett.*, 92:218301, 2004.

[57] G. D. Scholes. Long-range resonance energy transfer in molecular systems. *Ann. Rev. Phys. Chem.*, 54:57–87, 2003.

[58] Xanthipe J. Jordanides, Gregory D. Scholes, and Graham R. Fleming. The mechanism of energy transfer in the bacterial photosynthetic reaction center. *J. Phys. Chem. B*, 105(8):1652–1669, 2001.

[59] J. Adolphs and T. Renger. How proteins trigger excitation energy transfer in the FMO complex of green sulfur bacteria. *Biophys. J.*, 91:2778–2797, 2006.

[60] S. Georgakopoulou, R. van Grondelle, and G. van der Zwan. Explaining the visible and near-infrared circular dichroism spectra of light-harvesting 1 complexes from purple bacteria: A modeling study. *J. Phys. Chem.*, 110:3344–3353, 2006.

[61] R. C. Cheng and R. J. Silbey. Coherence in the b800 ring of purple bacteria lh2. *Phys. Rev. Lett.*, 96:028103–028106, 2006.

[62] A. Olaya-Castro, C. F. Lee, F. Fassioli Olsen, and N. F. Johnson. Efficiency of energy transfer in a light-harvesting system under quantum coherence. *Phys. Rev. B*, 78:085115, 2008.

[63] H. van Amerongen, L. Valkunas, and R. van Grondelle. *Photosynthetic excitons*. World Scientific Publishing Co. Pte. Lrd., 2000.

[64] H. Stahlberg, J. Dubochet, H. Vogel, and R. Ghosh. Are the light-harvesting I complexes from *Rhodospirillum rubrum* arranged around the reaction centre in a square geometry? *J. Mol. Biol.*, 282:819–831, 1998.

[65] A. J. Jackson, S. Lin, A. K. W. Taguchi, J. C. Williams, J. P. Allen, and N. W. Woodbury. Energy transfer in rhodobacter sphaeroides reaction centers with the initial electron donor oxidised or missing. *J. Phys. Chem. B*, 101:5747–5754, 1997.

[66] K. Timpmann, G. Trinkunas, P. Qian, C.N. Hunter, and A. Freiberg. Excitons in core LH1 antenna complexes of photosynthetic bacteria: Evidence for strong resonant coupling and off-diagonal disorder. *Chemical Physics Letters*, 414:359–363, 2005.

[67] D. J. Tannor. *Introduction to Quantum Mechanics: a Time-Dependent Perspective*. University Science Books, 2006.

[68] A. Ishizaki and G. R. Fleming. On the adequacy of the redfield equation and related aproaches to the study of quantum dynamics in electronic energy transfer. *J. Chem. Phys.*, 130:234110, 2009.

[69] J. Strumpfer and K. Schulten. Light harvesting complex II B850 excitation dynamics. *J. Chem. Phys.*, 131:225101, 2009.

[70] J. Strümpfer, M. Séner, and K. Schulten. How quantum coherence assists photosynthetic light-harvesting. *J. Phys. Chem. Lett.*, 3:536–542, 2012.

[71] M. Sener, J. D. Olsen, N. C. Hunter, and K. Schulten. Atomic-level structural and functional model of a bacterial photosynthetic membrane vesicle. *Proc. Nat. Acad. Sci. USA*, 40:15723–15728, 2007.

[72] A. Freiberg and K. Timpmann. Picosecond fluorescence spectroscopy of light-harvesting antenna complexes from Rhodospirillum rubrum in the 300-4 K temperature range. Comparison with the data on chromatophores. *J. Photochem. Photobiol B; Biol.*, 15:151–158, 1992.

[73] H.J.M. Kramer, J.D. Pennoyer, R. van Grondelle, W.H.J. Westerhuis, R.A. Niedermann, and J. Amesz. Low-temperature optical properties and pigment organization of the B875 light-harvesting bacteriochlorophyll-protein complex of purple photosynthetic bacteria. *Biochim. Biophys. Acta*, 767:335–344, 1984.

[74] C.P. Rijgersberg, R. van Grondelle, and J. Amesz. Energy transfer and bacteriochlorophyll fluorescence in purple bacteria at low temperature. *Biochim. Biophys. Acta*, 592:53–64, 1980.

[75] Donald R. Ort and Charles F. Yocum, editors. *Oxygenic Photosynthesis: the light reactions*. Kluwer Academic Publishers, 1996.

[76] A. Damjanović, H. M. Vaswani, P. Fromme, and G. R. Fleming. Chlorophyll exciations in photosystem I of *Synechococcus elongatus*. *J. Phys. Chem. B*, 106:10251–10262, 2002.

[77] G. Raszewksi and T. Renger. Light-harvesting in photosystem II core complexes is limited by the transfer to trap: can the core complex turn into a photoprotective mode? *J. Am. Chem. Soc.*, 130:4431–4446, 2008.

[78] G. Raszewksi, W. Saenger, and T. Renger. Theory of optical spectra of photosystem II reaction centers: location of the triplet state and the identity of the primary electron donor. *Biophys. J.*, 88:986–998, 2005.

[79] B.A. Raszewksi, G. Diner, E. Schlodder, and T. Renger. Spectroscopic properties of reaction center pigments in photosystem II core complexes: revision of the multimer model. *Biophys. J.*, 95:105–119, 2008.

[80] Y. Shiwei, M. G. Dahlbom, P. J. Canfield, N. S. Hush, R. Kobayashi, and J. R. Reimers. Assignment of the Q_y absorption spectrum of photosystem-I from *T*hermosynechococcus elongatus based on CAM-B3LYP calculations at the PW91-optimized protein structure. *J. Phys. Chem. B*, 111:9923–9930, 2007.

[81] L. Konermann and A. R. Holzwarth. Analysis of the absorption spectrum of photosystem II reaction centers: temperature dependence, pigment assignment, and inhomogeneous broadening. *Biochemistry*, 35:829–842, 1996.

[82] H. Lee, Y. C. Cheng, and G. R. Flemming. Coherence dynamics in photosynthesis: Protein protection of excitonic coherence. *Science*, 316:1462–1465, 2007.

[83] K. Timpmann, A. Freiberg, and V. Sundström. Energy trapping and detrapping in the photosynthetic bacterium rhosopseudomonas viridis: transfer to trap limited dynamics. *Chem. Phys.*, 194:275, 1995.

[84] K. Visscher, H. Bergström, V. Sündstrom, C. Hunter, and R. van Grondelle. Temperature dependence of energy transfer from the long wavelength antenna BChl-896 to the reaction center in *Rhodospirillum rubrum*, *Rhodobacter sphaeroides* (w.t. and M21 mutant) from 77 to 177 K, studied by picosecond absorption spectroscopy. *Photosynth. Res.*, 22:211, 1989.

[85] A. Damjanović, T. Ritz, and K. Schulten. Excitation energy trapping by the reaction center of *Rhodobacter Sphaeroides*. *Int. J. Quant. Chem.*, 77:139–151, 2000.

[86] K. Timpmann, F. Zhang, A. Freiberg, and V. Sundström. Detrapping of excitation energy transfer from the reaction center in the photosynthetic purple bacterium *Rhodospirillum rubrum*. *Biochim. Biophys. Acta*, 1183:185, 1993.

[87] R. G. Fleming, J. L. Martin, and J. L. Breton. Rates of primary electron transfer in photosynthetic reaction centres and their mechanistic implications. *Nature*, 333:190–192, 1998.

[88] nanoComposix europe. Silver nanoparticles: Optical properties. *http* : *//nanocomposix.eu/pages/silver − nanoparticles − optical − properties*, 06-11-2015.

[89] nanoComposix europe. Gold nanoparticles: Optical properties. *http* : *//nanocomposix.eu/pages/gold − nanoparticles − optical − properties*, 06-11-2015.

[90] Meindert Alexander van Dijk. *Nonlinear optical studies of single gold nanoparticles*. Doctoral thesis, Leiden University, 2007.

[91] T. Ziegler, C. Hendrich, F. Hubenthal, T. Vartanyan, and F. Träger. Dephasing times of surface plasmon excitation in Au nanoparticles determined by persistent spectral hole burning. *Chem. Phys. Lett.*, 386:319–324, 2004.

[92] S. Link and M. A. El-Sayed. Size and temperature dependence of the plasmon absorption of colloidal gold nanoparticles. *J. Phys. Chem. B*, 103:4212–4217, 1999.

[93] K. L. Kelly, E. Coronado, L. L. Zhao, and G. C. Schatz. The optical properties of metal nanoparticles: The influence of size, shape, and dielectric environment. *J. Phys. Chem. B*, 107:668–677, 2003.

[94] Y. R. Zhen, K. H. Fung, and C. T. Chan. Collective plasmonic modes in two-dimensional periodic arrays of metal nanoparticles. *Phys. Rev. B*, 78:035419, 2008.

[95] Z. Fan and A. O. Govorov. Plasmonic Circular Dichroism of Chiral Metal Nanoparticle Assemblies. *Nano Lett.*, 10:2580–2587, 2010.

[96] A. Kuzyk, R. Schreiber, Z. Fan, G. Pardatscher, E. M. Roller, A. Högele, F. C. Stimmel, A. O. Govorov, and T. Liedl. DNA-based self-assembly of chiral plasmonic nanostructures with tailored optical response. *Nature*, 483:311–314, 2012.

[97] W. Rechberger, A. Hohenau, A. Leitner, J.R. Krenn, B. Lamprecht, and F.R. Aussenegg. Optical properties of two interacting gold nanoparticles. *Opt. Commun.*, 220:137–141, 2003.

[98] R. Ghosh, H. Hauser, and R. Bachofen. Reversible dissociation of the B873 light-harvesting complex from *Rhodospirillum rubrum* G9+. *Biochemistry*, 27:1004–1014, 1988.

[99] D. Lupo and R. Ghosh. The reaction center H subunit is not required for high levels of light-harvesting complex 1 in *Rhodospirillum rubrum* mutants. *J. Bacteriol.*, 186:5585–5595, 2004.

[100] C. Vadeboncoeur, H. Noël, L. Poirier, Y. Cloutier, and G. Gingras. Photoreaction centre of photosynthetic bacteria. 1. Further chemical characterization of the photoreaction centre from *Rhodospirillum rubrum*. *Biochemistry*, 18:4301–4308, 1979.

[101] S. Amarie, D. Lupo, M. O. Lenz, R. Saegesser, R. Ghosh, and J. Wachtveitl. Excitation energy pathways in the photosynthetic units of reaction center lm- and h-subunit deletion mutants of *Rhodospirillum rubrum*. *Photosynth. Res.*, 103:141–151, 2010.